The University of Nottingham

Ultrastable heterodyne interferometry using a modulated light camera

Rikesh Ramesh Patel, MEng.

Division of Electrical Systems and Optics
University of Nottingham

Thesis submitted to the University of Nottingham
for degree of Doctor of Philosophy

June 2014

Abstract

Interferometry is used in a wide variety of fields for the instrumentation and analysis of subjects and the environment. When light beams interfere, an interference fringe pattern is generated. Captured widefield interference patterns can be used to determine changes in the optical path length of interfering beams across a 2D area. Two interferometer schemes regularly implemented in modern systems include the homodyne interferometer, where light with the same optical frequency in used to generate static intensity fringe patterns, and the heterodyne interferometer, where light with different optical frequencies are used to generate a fringe pattern that is modulated at a frequency equal to the optical frequency difference (beat frequency). A widefield heterodyne system is not straightforward to bring into practice, however, it does offer some benefits over a comparable homodyne interferometer, such as direct phase interpretation and the suppression of low frequency background light in interferograms.

In this thesis, a widefield heterodyne interferometer system is presented. A custom prototype modulated light camera (MLC) chip was used to capture both homodyne and heterodyne fringe patterns. The 32×32 pixel camera is capable of continuously demodulating incident modulated light at frequencies between 100 kHz and 17 MHz. In the presented system, an error in the interferogram phase was determined to be $\Delta\phi = \pm\, 0.16$ radians ($\sim 9.1°$). Comparisons between homodyne and heterodyne interferograms, captured using the MLC, are also presented.

With modifications to the system, an ultrastable widefield heterodyne interferometer system was implemented. The intention of this system was to eliminate the contribution of piston phase to a captured interferogram without the need for common path optics. In contrast to the standard heterodyne setup, the reference signal used in the demodulation process was derived from one of the pixels onboard the MLC, rather than from an external source. This new local reference signal tracks the common changes in the temporal phase detected by all the MLC's pixels, eliminating piston phase and substantially reducing the contributions of unwanted vibrations and microphonics from interferograms. To demonstrate this

ultrastable system, it is incorporated into a Mach-Zehnder interferometer, where a vibration is induced onto an object arm mirror (using a mounted speaker) at various frequencies. Stable interferograms are captured with the mirror moving at up to $85\,\mathrm{mm\,s^{-1}}$ at 62 Hz (an optical path length of $220\,\mu$m, or 350 wavelengths for $\lambda = 633\,\mathrm{nm}$), however, this limit was the result of the complex motion in the mirror mount rather than the stability limit of the system. The system is shown to be insensitive to pure piston phase variations equivalent to an object velocity of over $3\,\mathrm{m\,s^{-1}}$.

As an application of the ultrastable system, a novel interferometer has been developed that captures the widefield fringe patterns generated by interfering two independent light sources, rather than by a single split source. The two separately stabilised HeNe lasers, constructed in the laboratory, produce light with a reasonably stable output frequency. Interfering two of these sources produce a heterodyne interference pattern with an unknown beat frequency. The beat frequency continuously varies because of the variation in the output frequency of each laser, but these stabilised lasers produce a beat frequency that drift by as little as 3 MHz over 30 minutes. As the ultrastable system tracks changes in the temporal phase and instantaneous frequency of an incident fringe pattern, it can be used to track the variations in the modulation frequency generated by the fluctuations in the two separate lasers. The separation between the two lasers with regards to the images presented was about 35 cm, but they can be separated by much larger amounts.

Acknowledgements

Firstly, I would like to thank my supervisor, Matt Clark; Matt has been instrumental for the entirety of my PhD, from the concept of the project, through explaining the theory and aid in implementation of the various systems, right up to reviewing (as well as giving the initial push) for the journal publications and this thesis. His knowledge and insight in the field of optics is extraordinary; quite simply put, I would not be where I am without him.

I would like to thank my fellow lab-mate Samuel Achafuo-Yeboah; he designed the various cameras that I had used during my PhD project, as well as the initial control/acquisition hardware/software designs and implementations. His help in setting up the cameras has been much valued. I would also like to thank my first year secondary supervisor Ian Stockford for getting me started in the lab, Roger Light who has helped in a variety of ways especially with software issues, Richard Smith, Ben Waters and my brother Hiren Patel for proof reading my thesis, and all the other students and staff I dealt with in the SiOS lab and in the University's Applied Optics group in general.

Finally, I'd like to thank my family; my parents, who have always been supportive with whatever decisions I made in my life, and my brothers, who have always encouraged me to be the best that I can. I'd also like to thank my friends; the few that I still hang out with from before my post-graduate days and the ones that I made during my time at Lenton and Wortley Hall, and I'd like to thank my cousins, for basically hindering me, but making it all worthwhile.

Contents

List of Figures

List of Tables

Chapter 1

Introduction

In this chapter, an introduction of the work in this thesis is presented. A background of interferometry and interferometer detection methods is explored. This chapter will also discuss key concepts important to interferometer systems, such as photodetection and camera pixels, light coherence properties, and possible sources of noise and errors in captured images. An overview of this thesis, including the methodology for the experiments conducted and the thesis structure, is presented.

1.1 Introduction to interferometry

The phenomenon of wave interference can be observed in waves such as in light, sound and surface water. When waves interfere, they superimpose onto each other, which results in a new waveform defined as the sum of the component amplitudes.

Interferometers are instruments that use this property in light waves to measure the path differences between different beams of light. A light beam takes an amount of time for it to reach a point of observation from the emission source. This time will vary if the beam's path length is changed or if there is a change in the refractive index of the propagation medium. If the light wave is assumed to be sinusoidal, this time delay/advance can be observed as a phase change.

Direct detection of the phase for visible light is not possible because the optical frequencies (400-800 THz region) have oscillating fields much higher than any

feasible electronic devices' frequency response (i.e. MOSFETs have a frequency response in the 100 GHZ region [1]). One method of measuring light phase is to interfere the measurement or object light wave with a reference light wave. This generates an interference fringe pattern which can be captured as an interferogram image. The light intensity at difference points of an observed interferogram will depend on the phase difference between the interfering waves.

1.1.1 Historical overview

1.1.1.1 Young's double slit experiment

An experiment first conceived by Francesco Grimaldi in 1665 showed the interaction between two beams of light [2]. The setup involved a darkened room where light entered one end and exited through pinholes. Sunlight was used as the light source and two closely made pinholes let light fall onto an opaque screen. Grimaldi postulated that an image of the sun would appear but with circles of light overlapped with darkness. However, the experiment, was unsuccessful; the light entering the two holes was not coherent.

In 1799, Thomas Young, after working with the properties of acoustics, presented a paper to the Royal Society arguing the notion of light behaving like waves [3]. Young's theory contradicted Issac Newton's corpuscular theory of light, which stated light was composed of a stream of small particles [4]. In 1803, Young used his knowledge of overlapping sound waves generating beats to reproduce Grimaldi's experiment [5]. The sunlight now entered the apparatus through a pinhole, making it into a coherent light source; an interference pattern was visible.

The light source entering the two pinholes was spatially and temporally coherent. At the point where the two wavefronts have their respective maximum amplitudes (i.e. they are perfectly in phase), they constructively interfered, resulting in a bright fringe (maxima). When the two waves have amplitudes that negate each other (i.e. they are completely out of phase), they destructively interfered, resulting in a dark fringe (minima). This fringe pattern continues across the observable surface. The observation of interference showed that light can behave like waves.

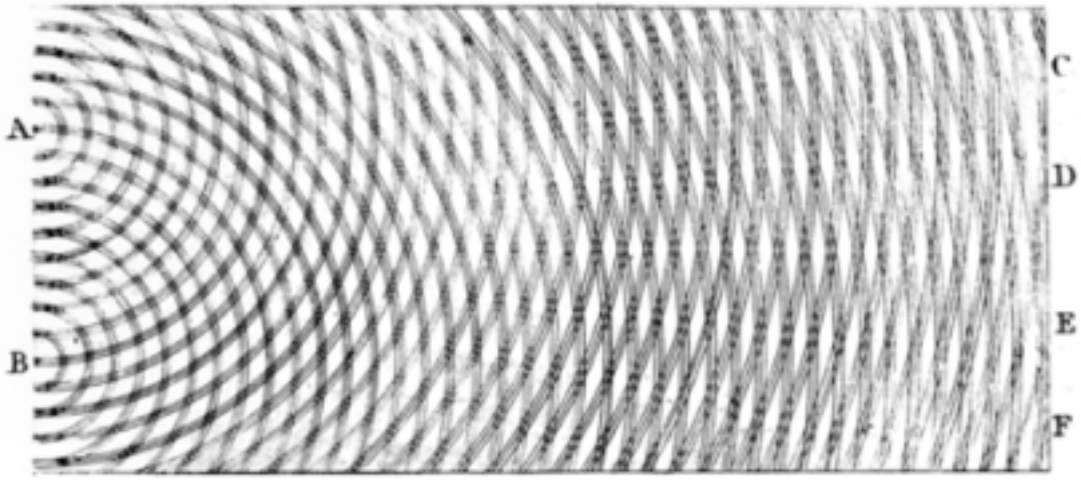

Figure 1.1: A sketch by Young showing the diffraction caused by two wavefronts [6]. A coherent wavefront incident on two slits produces two point sources, **A** and **B**. Points **C**, **D**, **E** and **F** show points of destructive interference (i.e. minima).

1.1.1.2 Michelson interferometer

During the 19^{th} century, the prevailing theory of light was that it must travel through a medium; just as tidal waves travel through water or sound through air, light was thought to travel through a medium called 'luminiferous aether'. However, proving its existence had been difficult.

In 1881, Albert Michelson used a device that sent light through a half silvered mirror, splitting the beam in two, each of which travelled in perpendicular directions [7]. The two beams were reflected back using mirrors, which caused them to interfere at the half silvered mirror.

The intensity of the fringe patterns would vary as the properties of the interferometer changed, which included the distance of the mirrors from the half silvered mirror and more importantly, the medium that the light travelled in.

Physicists such as James Clerk Maxwell [8] and George Gabriel Stokes [9] noted several restrictions on the aether medium. The medium had to be almost sta-

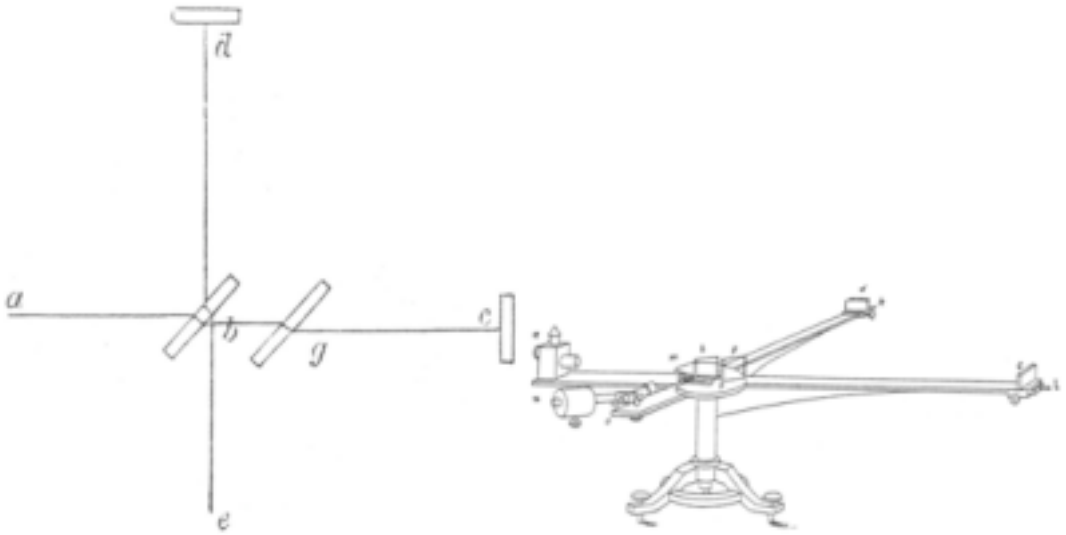

(a) (b)

Figure 1.2: Sketches of the interferometer designed by Michelson [7]. The left (a) schematic shows light being emitted from point a and split at point b. One of the beam paths has a compensation plate at g so both light beams travel through the same amount of glass. The beams are reflected back from the mirrors at c and d, and recombined and interfered at b. The fringe pattern is observable at e. The right (b) apparatus diagram shows the how the first Michelson interferometer was arranged and how the mirrors were designed to be moved.

tionary, otherwise large variations in the speed of light would be observable. To accommodate the high frequency of light, the medium would need to exhibit the properties of a solid material. However, to allow the Earth to move unhindered in proportion to other stellar bodies, the aether would have to move in one direction throughout the universe; this concept was known as the 'aether winds'.

It was postulated that as the Earth rotated, the direction of the wind would either aid or hinder light by a slight amount, fractionally changing the speed of light. Direct measurements of the speed of light would produce results too inaccurate to prove conclusively the presence of drag. Michelson intended to use his interferometer to detect sinusoidal oscillations in fringe patterns as one arm of the interferometer would travel both with and against the 'aether wind' over the course of a day. The experiment resulted in null results (a 4 % fringe shift was expected, only 1 % shift was detected), leading to Michelson to conclude that the

aether medium may be stationary rather than moving. Michelson repeated his experiment in 1887 with Edward Morley [10], in an improved system, measuring similar results. The results from these experiments eventually led to a rejection the aether medium concept.

1.1.2 Project brief

If we consider the most basic interferometer arrangement, a visible fringe pattern can be generated by interfering two coherent (explained in section 1.4) light beams, which can be simply produced by splitting a single initial light source. Analysing the intensity of the resulting interference pattern reveals the propagation distance differences of the split light. As each beam has the same optical frequency, a static intensity interference pattern is generated; this is known as homodyne interferometry [11]. In practice, when trying to capture the interference pattern, the influence from background light could make direct phase extraction from the pattern difficult.

One method of cancelling out the effects of low frequency background light from a captured pattern is to interfere light with different optical frequencies; this is known as heterodyne interferometry [12]. The detected intensity pattern is modulated at a frequency equal to the difference in the optical frequency difference between the interfering beams. Once the pattern has been captured, electronic filtering can be applied to remove the low frequency background light influence on the pattern.

One major disadvantage of developing a heterodyne interferometer is the complexity of the detector. The phase pattern across two dimensions (perpendicular to the optical axis) is often of interest; a widefield view of an interference pattern allows for the observation of any changes in the spatial phase difference, which is stored as an interferogram image. Additionally, fast capture of interferograms is required in situations where phase change occurs with time. As homodyne interferometers produce static intensity fringe patterns, the detector does not need to have large frequency response requirements or special demodulation circuitry. A widefield image of the fringe pattern can be captured and output in real time using standard commercially available digital cameras. Detectors used in heterodyne interferometer on the other hand, due to the response requirements, are

commonly implemented as point detectors [13]. The single-point detector can either be used to capture the real time phase at a single point in an interference pattern, or used to scan a pattern in order to acquire a widefield pattern over longer periods of time [14].

1.1.2.1 Widefield heterodyne interferometry

The initial aim of the project presented in this thesis was to investigate the use of a modulated light camera (MLC) for heterodyne interferometry. The MLC has been designed to detect modulated light, demodulate through signal mixing, and filter the result for output.

A heterodyne interferometer was built incorporating the MLC into the arrangement to capture widefield real-time interferogram images. Whilst this system may not be the first to capture real time widefield heterodyne interferograms [15, 16], the intention of this project was to produce a system that operates at much higher modulation frequencies than attempted before, as well as over a broader range of frequencies.

1.1.2.2 Ultrastable heterodyne interferometry

In order to demodulate a captured optical signal, the MLC requires the use of a reference signal. The phase data output from each pixel is generated relative to this reference signal. To produce a stable image, the reference signal is required to have the same frequency as the detected optical signal. However, a real system may not produce a stable pattern with a fixed frequency reference signal; this could be due to changing properties in the propagation medium or light source. An unstable image could also result from vibrations acting on the components of the interferometer. One form of instability external vibration imports onto a captured interferogram can be seen as piston phase change (a phase shift induced across the entire interferogram, often with an unknown and random function with time).

The main goal of this project was to investigate a method of producing ultrastable fringe pattern images using the widefield heterodyne interferometer. Instead of using an external fixed frequency reference signal, the reference signal is derived

from a single point in the fringe pattern itself. A reference optical signal, measured using a single pixel on the MLC, will have the same phase relationship, even in the presence of piston phase vibration, as the optical signal detected on all other pixels on the MLC. The intention of this setup was to cancel out any temporally varying phase change and produce stable interferograms.

1.1.2.3 Two laser interferometry

A heterodyne fringe pattern with temporally varying phase shifts can also be viewed as a pattern with a varying modulation frequency. For conventional interferometry, the visibility of the fringe pattern is dependent on the degree of coherence between the interfering light (a single split source is used in conventional interferometers). If the sources are not coherent, then the time averaged captured image shows no pattern.

As an extension to the project, the ultrastable system was adapted to capture the fringe patterns produced by interfering incoherent sources. The interferometer was designed using two separate lasers with the fringe pattern captured using the MLC. The single pixel feedback was employed to track the changes in the instantaneous beat frequency of the fringe pattern, enabling stable interference fringe patterns.

1.2 Concept of wave superposition

1.2.1 Interference phenomenon

The phenomenon of interference is based on the principle of superposition. The superposition property is present in all linear systems; this includes waves. The property states that the resultant response at any point in the system is equal to the sum of all the individual components at that point [17]; the resultant disturbance observed, E_{tot}, is equal to the algebraic sum of the separate constituent waves, E_1, E_2, ..., such that;

$$\mathbf{E}_t = \mathbf{E}_1 + \mathbf{E}_2 + \ldots \mathbf{E}_n \tag{1.1}$$

1.2.2 Electromagnetic waves

A wave can be described as a variation in amplitude at different spatial and temporal points. The amplitude relates to the parameter of the wave, such as the height or pressure. Light is a form of electromagnetic radiation and can be modelled as a transverse wave [8]. A light wave contains both electric and magnetic field components, with the direction of propagation perpendicular to the field components.

The electric field and magnetic field components of light waves are associated with the changes in each others fields [18–20]. To describe a wave, one field is used, commonly the electric field is chosen. In a homogeneous medium, free from regional currents and charges, the electric field homogeneous wave equation can be expressed as [17];

$$\frac{\partial^2 \mathbf{E}}{\partial t^2} - c^2 \cdot \nabla^2 \mathbf{E} = 0 \tag{1.2}$$

where $\mathbf{E}$ is the electric field, t is time and c is the speed of the wave. For a plane wave case, a monochromatic solution for this equation can be described by;

$$\mathbf{E}(\mathbf{r}, t) = \mathbf{E}_0 \cos(\mathbf{k} \cdot \mathbf{r} - \omega t + \phi_0) \tag{1.3}$$

where ω is the angular frequency, t is time, $\mathbf{k}$ is the wave vector, and $\mathbf{r}$ is the position vector, $\mathbf{E}_0$ is the peak electric field vector and ϕ_0 is the initial phase offset of the wave, i.e. the wave angle at time $t = 0$ and $|\mathbf{r}| = 0$.

1.2.2.1 Polarisation

Given that the electric field wave is a transverse wave, a plane wave travelling in the z direction can have field components in the x and y direction. The wave can be expressed as separate scalar components in the x and y direction;

$$\begin{aligned} E_x &= a_x \cos(kz - \omega t + \phi_0) \\ E_y &= a_y \cos(kz - \omega t + \alpha + \phi_0) \end{aligned} \tag{1.4}$$

where the electric wave components, E_x, E_y, in the x and y direction have amplitudes, a_x and a_y, and α is the relative phase difference between the components

(a value between $-\pi$ to π).

The polarisation state of the wave describes the shape the wave traces as it propagates [17]. The wave is linearly polarised if the relative phase difference between the two components, $\alpha = 0, \pm\pi$; the electric field oscillates in a straight line. The angle of the polarisation, relative to the x/y axis, is dependent on the amplitude of the separate components, a_x and a_y.

If one component leads or lags the other component but is not in or out of phase with the other, i.e. $\alpha \neq 0, \pm\pi$, then the wave is elliptically polarised. Additionally, a special case occurs when $\alpha = \pm\frac{\pi}{2}$ and $a_x = a_y$; this produces circularly polarised light.

The interferometers designed for this project will use light sources that have the same polarisation type and angle, with polarisers used for compensation if required. To this end, it is possible to simplify the wave equation further, and express it as a single scalar equation;

$$E = a_0 \cos(kz - \omega t + \phi_0) \tag{1.5}$$

1.2.3 Detection of intensity

Light waves are not measured instantaneously; the frequency of visible light is too high for photodetectors to generate an instant response [1]. Instead, a detector will integrate the received light energy over an amount of time. The intensity of light, I, describes the average light energy per unit area over a period of time. In the specific case of harmonic fields, the intensity is proportional to the square of the amplitude of the electric field [17];

$$I \propto |\mathbf{E}|^2 \tag{1.6}$$

The photocurrent generated by a photo-detector device (e.g. photodiode) is proportional to the square of the amplitude of the electric field. Therefore, the generated photocurrent is proportional to the light intensity incident on the detector. The actual current generated is also dependent on the depth of surface penetration, the wavelength of the light, and the photosensitive material itself [21]. These factors determine the responsivity of a device (measured in amperes per watt) and are taken into consideration when designing photodetectors (discussed

in section 1.6.2).

1.2.4 Information determined from phase measurements

Given the assumption that in a light wave the field components oscillates sinusoidally, the field components repeat periodically over time $t = T$. This is determined by the frequency, f, of the wave, such that;

$$f = \frac{1}{T} = \frac{\omega}{2\pi} = \frac{c}{\lambda} \tag{1.7}$$

where λ is the wavelength and c is the speed of the wave in a vacuum ($c \approx 3 \times 10^8\,\mathrm{m\,s^{-1}}$). The wave vector describes the displacement of a wave as it travels;

$$k = |\mathbf{k}| = \frac{2\pi}{\lambda} \tag{1.8}$$

Using the simple scalar wave equation expressed in equation 1.5, it is possible to see that this wave propagates through one wavelength in the time equal to one period. At the point of observation, it can be assumed that an incident light wave takes the form;

$$E = a_0 \cos(\omega t + \phi) \tag{1.9}$$

where ϕ is the phase observed at the point of detection. Comparing equation 1.9 with equation 1.5 shows that changing the propagation time of the wave can change the phase of a wave at the point of observation. One method of implementing a phase change is by varying the propagation distance as the wave travels.

The other method involves changing the propagation medium. The wavelength of light changes as it travels through mediums with different refractive indexes. Given the wavelength of the light wave in a vacuum, λ_0, the refractive index of the medium the light travels through, n, can be determined using;

$$n = \frac{\lambda_0}{\lambda} \tag{1.10}$$

where λ is the wavelength of light inside the medium. Vacuum has a refractive index of $n = 1$. The diagram in figure 1.3 shows the instantaneous phase observed at a single observation point at a fixed moment in time.

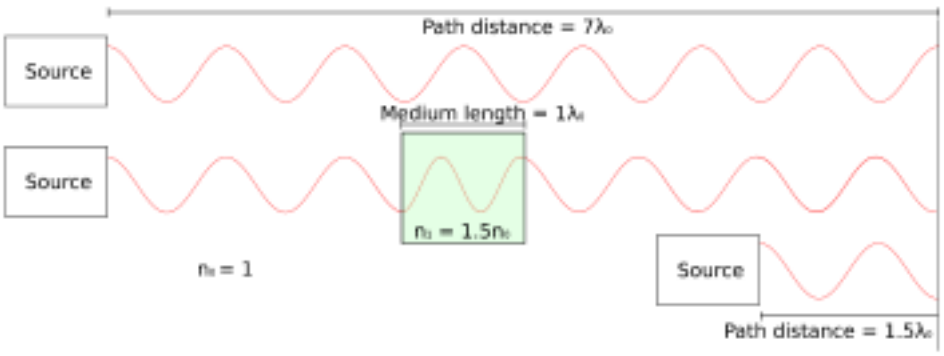

Figure 1.3: Examples of waveforms at an instant in time. Methods of altering the phase measured at an observation point include changing the propagation medium and the path length.

The phase of an incident light wave can be used to determine the propagation distance or propagation medium, and one method of determining the phase is by using interferometry.

1.3 Determining phase using interferometry

1.3.1 Homodyne interferometry

Homodyne interferometry is one technique that can be used to determine the phase of an incident light wave. Two interfering waves, a reference and object wave, in homodyne interferometry, have the same optical frequency (ω_h). The electric fields of these two beams at the point of detection, E_{hr} and E_{ho}, can be expressed (using equation 1.9) as;

$$\begin{aligned} E_{hr} &= a_r \cos(\omega_h t + \phi_r) \\ E_{ho} &= a_o \cos(\omega_h t + \phi_o) \end{aligned} \tag{1.11}$$

It is possible to express these two waves as a single interfered resultant wave, E_{ht}, using the superposition principle discussed in section 1.2.1;

$$E_{ht} = E_{hr} + E_{ho} \tag{1.12}$$

As discussed in section 1.2.3, a photodetector will generate an electric current proportional to the intensity of incident light, which itself is proportional to the

square of the electric field (equation 1.6). The intensity of the pattern measured by the photodetector, I_h, as a result of the two waves interfering can be expressed;

$$\begin{aligned} I_h = [E_{ht}]^2 &= I_{hr} + I_{ho} + 2\sqrt{I_{hr} I_{ho}} \cos(\phi_{hd}) \\ &= I_{\text{offset}} + I_{\text{amplitude}} \cos(\phi_{hd}) \end{aligned} \tag{1.13}$$

where $\phi_{hd} = (\phi_{hr} - \phi_{ho})$ is the phase difference between the two interfering waves, and I_{hr} and I_{ho} are the intensities of the separate beams (reference and object beams respectively) [12]. The intensity of a detected pattern will vary sinusoidally as the phase difference term changes.

1.3.2 Heterodyne interferometry

Another interferometry technique used for phase measurement is the heterodyne interferometer. Wave interference occurs between beams with different optical frequencies, ω_r and ω_o for the reference and object wave respectively. Their electric fields, E_r and E_o, can be expressed;

$$\begin{aligned} E_r &= a_r \cos(\omega_r t + \phi_r) \\ E_o &= a_o \cos(\omega_o t + \phi_o) \end{aligned} \tag{1.14}$$

The resultant interfered electric field wave is equal to the sum of these two waves (equation 1.1). The intensity of this wave, I, can be determined (like in the homodyne case) using the square of the electric field wave and the trigonometric product-to-sum identity;

$$\begin{aligned} I &= [E_r + E_o]^2 \\ &= \frac{1}{2}{a_r}^2 + \frac{1}{2}{a_o}^2 + \frac{1}{2}{a_r}^2 \cos(2\omega_r t + 2\phi_r) \\ &\quad + \frac{1}{2}{a_o}^2 \cos(2\omega_o t + 2\phi_o) \\ &\quad + a_r a_o \cos((\omega_r + \omega_o)t + (\phi_r + \phi_o)) \\ &\quad + a_r a_o \cos((\omega_r - \omega_o)t + (\phi_r - \phi_o)) \end{aligned} \tag{1.15}$$

Due to the frequency response of the photodetector, certain components from this interference expression are not detected [1]; these include the temporally varying

components where $\omega = \omega_r, \omega_o, (\omega_r + \omega_o)$. The detected intensity can therefore be expressed as;

$$I = I_{\mathrm{DC}} + A\cos(\omega_d t + \phi_d) \tag{1.16}$$

$$\begin{aligned} I_{\mathrm{DC}} &= \frac{1}{2}{a_r}^2 + \frac{1}{2}{a_o}^2 \\ A &= a_r a_o \end{aligned}$$

where differences in beam frequency (beat frequency) and phase between the two beams (phase difference) are described by $\omega_d = (\omega_r - \omega_o)$ and $\phi_d = (\phi_r - \phi_o)$, respectively. Unlike the homodyne case, the intensity of an interference pattern will vary sinusoidally with time. However, the phase offset of this optical signal is equal to the phase difference between interfering beams. If the phase of the reference beam is kept constant, the electronic signal observed on the photodetector is the same signal once carried by the object beam; the process is effectively down-mixing a 400-800 THz signal to a frequency at which the photodetector can operate.

1.3.3 Interferometer technique considerations

In addition to the fringe pattern, photodetectors also detect external light incident on them (assuming the light wavelength is within the photosensitive material absorption range), and contributions from these external sources (e.g. sunlight or ceiling lights) can be seen on captured interferograms as errors (i.e. increase in the DC intensity).

A homodyne interference fringe pattern comprises of points of static intensity; the equipment required for a homodyne interferometer arrangement is minimal and can be aligned easily (patterns can be seen by the human eye). To capture widefield images, commercially available cameras can be used which makes the system inexpensive and easily scalable. If an interferogram is in the presence of an external DC intensity, the fringe pattern visibility will decrease (an increased intensity average). This can be expressed using;

$$\nu = \frac{I_{\mathrm{max}} - I_{\mathrm{min}}}{I_{\mathrm{max}} + I_{\mathrm{min}}} = \frac{I_{\mathrm{amplitude}}}{I_{\mathrm{average}}} \tag{1.17}$$

where ν is visibility of the fringe pattern. This issue is further compounded if the background light varies with time, i.e. low frequency influence. There are methods of physically blocking background light, however, in some situations, this may be impractical. For example, where light from an open or distant light source is used. In such cases, different interferometer phase extraction methods are required.

Heterodyne interferometry is an alternative method of determining the phase whilst suppressing low frequency background light in a capture interferogram. As the intensity fringe pattern is modulated at a high frequency, the detector will require a high frequency response. This is a simple matter for a point detection scheme, where the phase value is output for a single point in the interferogram (only one high frequency response photodetector, one demodulation circuit and one analogue-digital converter is required). However, this becomes more complex when capturing a widefield image. Heterodyne arrangement require more components that an equivelent homodyne arrangement. This may include a device to shift the frequency of light and signal generators for referencing and driving the shifting device. Alignment also becomes more problematic as the fringe pattern will not be visible by eye.

One of the main challenges of capturing an interferogram is in a situation where the phase dependent component of the pattern is weak. In both homodyne and heterodyne schemes, this equates to a low intensity variation, which when detected, produces a small photocurrent change. Using an analogue-digital converter (ADC), this small signal can become difficult to read as noise contributions from the surrounding electronic circuitry will increase the system's uncertainty figure (discussed further in section 1.7). The signal can be amplified and filtered, however, if the noise present in the system is within the same frequency band as the signal, then amplification and filtering has no effect on the overall signal to noise ratio.

In practical arrangements, the intensity of the object beam can often be limited. Increasing the intensity of the reference beam will increase the overall fringe pattern intensity. However this will increase the constant DC term, as well as the phase dependent term (referring to equation 1.17). The system will therefore require a method of filtering out the constant DC intensity. In heterodyne systems

this is achieved simply by electronic filtering the received signal.

1.3.4 Fringe pattern analysis

Whilst the intensity on a captured homodyne interferogram is dependent on the phase difference of interfering beams, directly interpreting individual points on the interferogram into a phase value will produce results of limited accuracy. Instead, direct analysis of a fringe pattern can be implemented by tracking the maxima and minima across a captured image. While it is possible to perform fringe analysis by eye, computer algorithms have been designed to search for these extreme points to provide fast results [22]. In addition to tracking points of maximum intensity, the algorithms have been based on finding the maximum points in the gradient of the measured intensity or discontinuities in the fringe pattern (i.e. shift in the position of the maxima) [23]; the information determined using these methods can be used to generate a phase map. However, phase variations between maxima/minima points are often disregarded, limiting the spatial resolution of the phase image; these point are often filled in using interpolation.

As this process requires only one image, low frequency intensity drifts from background light will not influence the end results, given the condition of a high frame capture rate. However, this extraction method requires that the captured pattern have several fringes, each spaced to allow optimum phase determination (which may depend on the detector's resolution, expected interferogram or noise presence); this could limit the interferometer design and complicate alignment. Additionally, if the system is subjected to temporally varying background light or vibration, then no averaging or pixel integrating scheme can be implemented to reduce the influence of errors on the results. Finally, without additional information about the homodyne interferogram, it could be difficult to assign a sign to the phase map.

1.3.5 Spatial domain filtering method

Another method of extracting the phase from a homodyne interferogram is by spatially filtering the fringe pattern. An interference pattern arranged to produce a pattern with many fringes will have large spatial frequencies, whilst the DC off-

set of the pattern and, ideally, any influence from background light will have low frequencies or zero spatial frequency. By filtering (i.e. blocking in the Fourier plane) the interferogram, the phase component can be isolated and extracted. The filter would need to be designed with knowledge of the intended fringe pattern to preserve the maximum spatial resolution in the image. This method can be implemented computationally by Fourier transforming the captured interferogram in two dimensions and applying an ideal filter to the results [24]. In this scenario, averaging could be used to reduce random noise from images. However, the application of the filter will add systematic phase errors to an interferogram; the process could become unreliable if the filter is not optimised for the incident fringe pattern or if there is a drastic change in the fringe pattern shape.

1.3.6 Quadrature measurements

Examining both the homodyne (equation 1.13) and heterodyne (equation 1.17) interference expressions, we can see that the detected intensity is dependent on three unknown variables. These include the DC offset intensity, the phase component amplitude and the phase difference (ϕ_d). One method of determining the phase whilst eliminating the other two unknown variables is by acquiring at least three simultaneous equations, in this case, by acquiring the intensity values as a known phase shift is applied to the interferogram.

This phase extraction method can be implemented with a minimum of three intensity measurements [25], however, the calculation for determining the phase becomes simpler if four specific measurements are taken; these are at quadrature phase intervals (at 90° phase differences). Taking the homodyne interference expression as an example, we can see that these four expressions are;

$$\begin{aligned} I_0 &= I_{\text{offset}} + I_{\text{amplitude}} \cos(\phi_d) \\ I_1 &= I_{\text{offset}} + I_{\text{amplitude}} \cos\left(\phi_d + \frac{\pi}{2}\right) \\ I_2 &= I_{\text{offset}} + I_{\text{amplitude}} \cos(\phi_d + \pi) \\ I_3 &= I_{\text{offset}} + I_{\text{amplitude}} \cos\left(\phi_d + \frac{3\pi}{2}\right) \end{aligned} \tag{1.18}$$

As a phase shift is applied, a different intensity is measured, but the DC offset and phase amplitude stay the same. Once these values are acquired, the phase can be extracted using an inverse tangent operation;

$$\begin{aligned} \phi_d &= \arctan \frac{I_3 - I_1}{I_2 - I_0} \\ &= \arctan \frac{2\sin(\phi_d)}{2\cos(\phi_d)} \end{aligned} \tag{1.19}$$

This process can be used to determine the phase as long as the DC intensity offset and phase component amplitude remains constant while the interferograms are being captured.

1.3.6.1 Phase stepping interferometry

A common method of extracting the phase from a homodyne interference pattern is by using phase stepping [26]. Known phase steps in the captured interferogram are applied; common implementation methods include using a piezoelectric transducer (PZT), or a stepper motor and wave plate arrangement. An example implementation could involve mounting the reference arm mirror of a Michelson interferometer to a piezoelectric transducer; by adjusting the displacement of the mirror by multiples of $\frac{\lambda}{8}$, phase shifts of $\frac{\pi}{2}$ are induce on the captured interferogram. Interferometers that capture four results are commonplace [27], however, systems where three [28] or five [29] captures are also possible.

In contrast to the direct fringe analysis or spatial filtering method, accurate phase measurements can be acquired at every capture point (instead of simple fringe separation measurements and with no loss in the spatial resolution in the resultant image). In an ideal system, the pattern remains static for the duration of the phase stepping process, allowing standard camera devices to capture the homodyne interferogram and the option of averaging or pixel integration if random noise is present in the captured interferogram. Only an inverse tangent operation is required post capture meaning the frame rate of a system is not limited by the post capture process.

The implementation of linear transducers for phase shifting interferometry can be complex due to alignment difficulties. The PZT is required to produce sub-wavelength displacements (wavelength must be known for this method). Finally, the system is still susceptible to errors from low frequency variation in background light and vibration in the interfering arms between the multiple phase stepping

points.

1.3.6.2 Continuous phase shifting interferometry

The continuous phase shifting method is a variation of the phase stepping method; instead of introducing discrete phase steps, the phase is varied continuously with time [30, 31]. This makes a system that is analogous to a heterodyne interferometer since the intensity pattern will be modulated. For example, a linear phase shift through 2π (i.e. one wavelength displacement) over one second produces the same detected interferogram as a heterodyne system with a beat frequency of 1 Hz.

An example system could use an integrating pixel camera (e.g. a standard CCD camera) to begin capture of the interferogram at fixed intervals (i.e. samples) within the interferogram modulation period. To illustrate the system, figure 1.4 shows an example plot of four captures (with a short integration period) as the phase is shifted continuously with time.

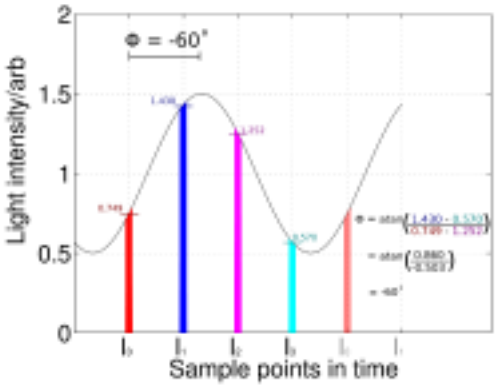

Figure 1.4: An example plot showing four captures per modulation period. The phase offset of this example, ϕ = -60 °, is determined by acquiring the quadrature measurements and using equation 1.20.

This method requires a reference signal, linked with the phase shifting mechanism, to synchronise with the capture times of the detector (e.g. using a phase lock loop). The read rate required from the detector is linked to the modulation frequency of the interferogram. For low modulation frequencies, a standard digital camera can be used to capture interferograms. However, like the phase stepping interferometer, this system can be susceptible to errors from background low fre-

quency light (i.e. intensity variation over the long modulation period). Therefore, a high modulation frequency is desirable. This requires a method of gating exposure to the incident light (e.g. optical chopper) if the modulation frequency exceeds the frame rate of the detector [32]. Additionally, if the fringe pattern remains stable, the measured intensity can be integrated/averaged over multiple modulation periods.

1.3.6.3 Heterodyne demodulation through mixing

Another method of extracting the phase from a modulated optical signal is through electronic signal mixing. The objective of the method is to down-mix the measured intensity signal using a local oscillator or reference signal. This technique is used in other demodulation systems outside the modulated camera field (e.g. superheterodyne radio receiver) [33]. The type of waveform used for mixing largely determines the complexity of the system design (e.g. electronic circuitry). Mixing two electronic signals (i.e. the measured optical signal and external reference signal) involves multiplying the components in each signal with the components of the other signal. The multiplication of two sine waves produce sum-and-difference components (explained further in section 3.1.2); if they have the same frequency, a DC phase result is produced (e.g. $\cos(\phi)$). Since the mixing process can be conducted at any time (or all the time), mixer devices can operate in parallel; this method can be used to output phase information continuously.

The simplest implementation of this method involves mixing the measured signal with a square wave. One method of implementing square wave mixing involves switching the incident signal (e.g. using a switching multiplier) i.e. the input wave is inverted and non-inverted every half modulation period. Figure 1.5(a) illustrates the square wave mixing process.

This measured signal is mixed with the reference square wave with different phase offsets; for quadrature demodulation, the measured signal is mixed separately with four reference signals, as shown in figure 1.5(b). Low pass filtering isolates the DC component in the mixer output (i.e. phase information), which is then used in equation 1.20.

The alternative to this scheme is to analogue mix the incident signal. Implement-

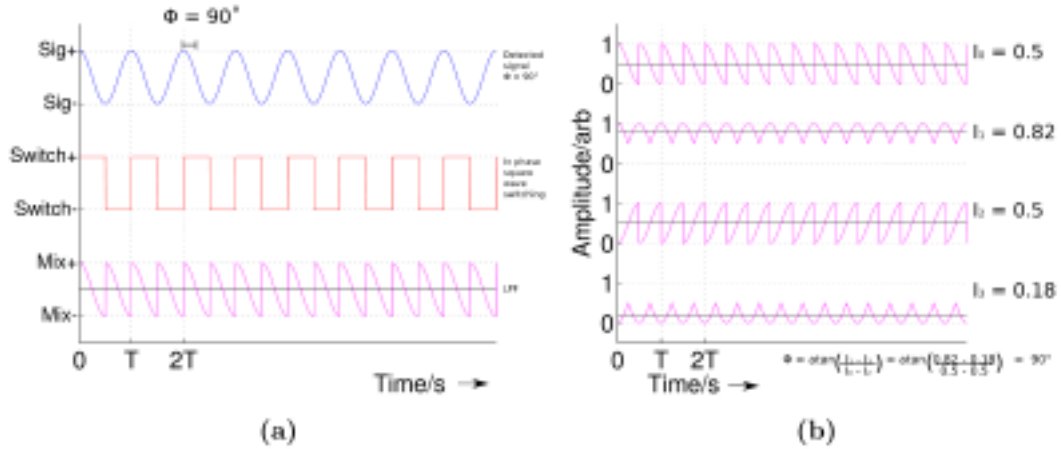

Figure 1.5: Example plots of an incident waveform (phase offset $\phi = 90°$) and a demonstration of the demodulation process using square wave mixing. The left figure (a) shows the mixed measured signal (blue sine wave) with the in-phase square wave (red), resulting in the (magenta) pre-filtered waveform and the ideal LPF output (black trace). The right (b) shows the mixed and LPF outputs (with a normalised amplitude range), I_0, I_1, I_2, I_3, where the measured signal is mixed with their respective phase offset local square wave. The phase calculation using equation 1.20 is shown.

ing an analogue mixing demodulator can be more complex than simply switching a signal (discussed further in section 3.1.3.2) especially for in-pixel implementations. However, it enables the mixing of the measured signal (ideally a sine wave) with a reference sine wave. In contrast to square wave mixing, the measured signal is mixed with only one sine wave instead of a series of sine waves, resulting in a higher retention of spectral power at DC (which contains phase information) and a cleaner frequency spectrum (allowing for a relaxation in the filter requirement and a reduction in out-of-band noise which could saturate electronic circuitry). The MLC used for capturing widefield interferograms in this project uses this type of demodulation technique (explored further in section 3.1.1).

1.4 Coherence

The wave equation expressed in section 1.2 makes the assumption of the ideal circumstance where light has a single optical frequency, i.e. monochromatic light. If a light source emits only at one frequency, it is possible to fully predict (and

expect) interference with itself (or another single frequency beam) at any point along its propagation. The beam can be described as being totally coherent at all temporal points, i.e. infinite coherence time and length.

The coherence of a beam is a set of properties which define how well the beam will enable interference [12]. A real source will emit light within an optical frequency band and the instantaneous emission frequency at any point in time cannot be predicted. For this reason, the frequency difference (beat frequency) between two separate sources is unknown and can vary randomly; the light emitted can be considered mutually incoherent. If the light is interfered, they will not produce a visible fringe pattern using conventional detection methods (explored further in chapter 6). Therefore, simple interferometers use light from single split sources. However, even this interferometer arrangement has limitations.

The temporal coherence determines the amount of phase drift (and therefore frequency variation) that occurs in an emitted waveform as it propagates, i.e. the degree of a phase relationship with itself at origin at different temporal points in a wave. The temporal coherence of a light wave is an important factor for amplitude splitting interferometer arrangements (e.g. Michelson interferometer), where interference occurs between the wave and a time delayed version of that wave. The coherence time, τ, of light is the amount of propagation time between which light is considered temporally coherent. The coherence length, L_c, is the distance that light travels in that coherence time. The visibility of a fringe pattern in the interferometer will decrease as the optical path length difference approaches the coherence length as illustrated in figure 1.6 [17]. If the OPL difference is more than the coherence length, then the two interfering light beams will be considered incoherent, i.e. no visible fringe pattern.

The coherence time is related to the bandwidth of the light source, Δf, such that;

$$T_c \Delta f \approx 1 \tag{1.20}$$

A source with a large range of emission frequencies, Δf, loses correlation with itself in a shorter time than a source with a smaller bandwidth.

Similar to temporal coherence, the spatial coherence of a wave determines the amount of phase drift observed across the wavefront, i.e. the phase relationship

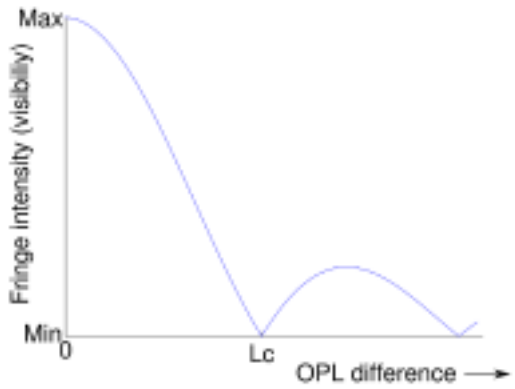

Figure 1.6: A plot of the visibility of a fringe pattern as the OPL difference between interfering beams approaches and extends beyond the coherence length of the source [12].

at different point spatial points. The spatial coherence of a light wave is an important factor for wavefront splitting interferometer arrangements (e.g. Young's double slit experiment).

1.5 Interferometer arrangements

An interferometer can be designed in a number of ways. Two of these arrangement categories are double path and common path interferometers.

In a double path (D-P) interferometer, a beam is split and each beam travels different paths before being interfered. These paths can be referred to as the reference arm and object arm, where often the reference arm retains a control wavefront and the object arm transmits through or reflects off a sample. The source of an amplitude splitting arrangement is commonly split using a beamsplitter, which typically splits the light 50:50 and into a perpendicular direction, or alternatively, using a polarising beamsplitter, which splits a beam depending on the polarisation state of the beam components.

The Michelson interferometer is one form of a double path interferometer [7, 10] (figure 1.7(a)). A beam from a source is split into separate arms using a beamsplitter. Each arm reflects back to the initial beamsplitter using mirrors, generating an interference fringe pattern at the exit of the beamsplitter. A variation of this interferometer is the Twyman-Green interferometer [34–36] which replaces

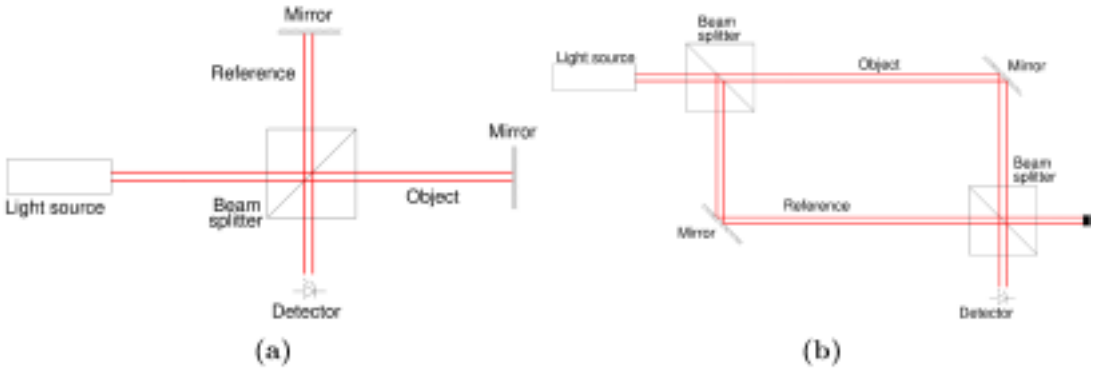

Figure 1.7: Schematics of double path interferometers. Left (a) shows the Michelson interferometer and right (b) shows a Mach-Zehnder interferometer.

the reference mirror with a reference surface; this setup is used to test optical components for difference/defects (i.e. phase comparison between reference and test surfaces).

Another double path interferometer is the Mach-Zehnder interferometer [37, 38] (figure 1.7(b)). This setup also uses a beamsplitter to split a beam into separate arms, however, the beam paths reconverge into another beamsplitter (after reflecting off individual mirrors) where interference occurs.

In these interferometers, the phase of the observed interference pattern varies as the OPL of the object beam varies (assuming a static reference arm). Additionally, these homodyne interferometers can be converted into a heterodyne interferometer by introducing a frequency shifting device into either interferometer arm.

For a common path (C-P) interferometer, the interfering beams propagate mostly along the same path. Temporally varying phase (e.g. from vibration) common in both interfering beams is cancelled out when they interfere; the interferometer produces stable fringe patterns. Figure 1.8 shows examples of three C-P arrangements.

One form of a common path interferometer is the lateral shearing interferometer [39]. The arrangement uses a shear plate, made from high quality flat glass (figure 1.8(a)); when a beam is incident on the plate at an angle, it is reflected off the exterior surface. The incident beam is also transmitted into the plate

and reflected off the internal surface at the other end of the plate. This beam then transmits back through glass and interferes with the first reflected beam, generating a laterally shifted interference pattern. One usage for the shearing interferometer is to determine whether a beam is collimated [40]. In simple arrangements, the thickness of the plate sets the requirement for the coherence of the incident light (to ensure a visible pattern), however, more complex arrangements can be used to relax the coherence requirement [41].

Another common path arrangement is the point diffraction interferometer [42,43]. The setup includes an apparatus which operates like a spatial filter (figure 1.8(b)); by placing the aberrated beam through a lens and placing a pinhole at the focal plane, all but the DC spatial frequency is filtered. In point diffraction interferometry, the pinhole apparatus is semi-transparent. At the observation plane, an interference pattern is generated between the filtered reference beam and the 'semi-transmitted' object beam. The pinhole-lens arrangement is simple, however considerations need to be made for alignment and high optical power arrangements (i.e. trade-off between optical power and pinhole material costs).

The Sagnac interferometer system is used to determine rotational speed [44, 45]. In this common path arrangement, a beam is split into arms, after which each arm propagates in different directions (figure 1.8(c)). Mirrors are placed in the interferometer to form a ring where the split beams overlap (e.g. three mirrors and beamsplitter can be positioned to reflect the beams into a square ring travelling in opposite directions). As the interferometer rotates, one beam travels a shorter path compared with the other, generating a shifting interference fringe pattern; the rate of this shift is used to determine the angular speed of the interferometer.

The choice in using different interferometer arrangements depend on the experimental need. The key difference between the C-P and D-P interferometers is that the C-P reveals the phase difference relative to a shifted or filtered version of itself; it is optically self-referenced. This property of the C-P interferometers can be both an advantage and disadvantage. The setup generates a stable interferogram, however, the phase range of the system is limited by the optical component arrangement. The arrangement also has the ability to produce an interferogram without a separate reference beam, allowing for compact interferometer designs and relieves issues with a separate beam's mutual coherence requirement with

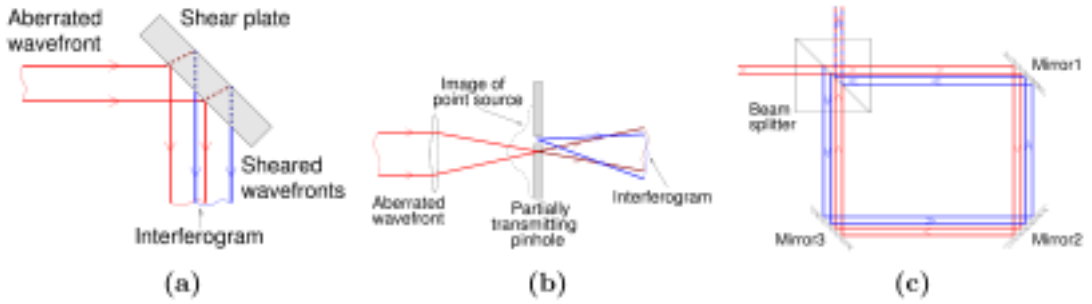

(a) (b) (c)

Figure 1.8: A selection of common-path interferometers, where the interfering beams travel along the same path (with a slight deviation). The left (a) diagram shows a shearing interferometer using a shear plate. The wavefront reflected from the front of the plate interferes with the wavefront reflected from the back of the plate. The middle (b) diagram shows the point diffraction interferometer, an unfiltered wavefront interferes with a spatially filtered wavefront using a semi-transparent pinhole apparatus. The right (c) diagram shows a Sagnac interferometer, a beam is split and each beam travels round a ring of mirrors in opposite directions before interference occurs.

the aberrated beam.

Alternatively, the D-P interferometer is used to determine the phase difference between an object and reference beam. This allows for a variable phase range (up to the coherence length difference) but will not produce a stable interferogram if each arm experiences separate vibrations. The D-P interferometer can be less complex (and less expensive) to setup and align than a C-P interferometer. Finally, intensity variation across an aberrated beam could make image capture difficult in a C-P interferometer due to its self-referencing property. For example, if the incident pattern was strongly scintillated or had high spatial frequencies, fringe visibility may be extremely low (or non-existent). Fringe visibility is more controllable if a separate reference beam was used to interfere with the aberrated beam.

The widefield ultrastable heterodyne interferometer described in this project uses an electronic feedback system to keep a captured interferogram stable, where the measured phase is relative to a single point on the interferogram (eliminating piston phase), whilst maintaining an interferometer setup with a separate reference arm. If a situation arises where the absolute phase difference is required (i.e.

phase difference between the reference and object arm), then the electronic local reference signal can simply be switched from the feedback system to an external signal.

1.6 Electronic Photodetection

1.6.1 Widefield imaging

To extract phase from an interference fringe pattern, a measurement of the pattern intensity is required. The intensity at a single location can be measured using a point detector, for which the capture unit and phase extraction components can be simple and inexpensive. Measuring the intensity values across a 2D region can be used to construct widefield phase images, revealing information about the wavefront of the interfering beams.

A widefield phase image can be used to observe variations in physical properties across an inspection object (i.e. changes in mediums, thicknesses or to acquire the surface profile), the interferometer arrangement (i.e. from tilting or path length changes), or detecting anomalous results across the data set (i.e. from electronic noise or an aberration in the apparatus). It is possible to generate a widefield image using a point detector by scanning across a fringe pattern [14], however, due to timely mechanical translations, any fringe pattern change during a scan (e.g. changes in refractive index or the thickness of an object, or due to external vibration) will result in unstable interferograms.

The simplest solution for capturing widefield interferograms involves using an array of photodetectors to capture light; commercially available digital cameras are designed using this array structure. Since each photodetector unit in the camera, known as a pixel, operate independently of each other, only the locally incident intensity (e.g. of a fringe pattern) is measured and output. Commercially available cameras are ideal for widefield capture of homodyne fringe patterns. However, an alternative operating scheme or camera is required for capturing the high frequency heterodyne fringe patterns (section 2.1).

1.6.2 Pixel operation and design

The photosensitive area of each camera pixel converts incident light into a photocurrent by generating an electron-hole pair. Current flow can be described as a movement of charge carriers. In a semiconductor, these carriers exist as an electron flow in the material conduction band and a flow of holes (electron vacancy) in the valence band [1]. The properties of a semiconductor allow for an electron to move from the valence band to the conduction band if it supplied with enough energy. The amount of energy required, i.e. the bandgap, is dependent on the material.

Light can be described as a stream of photons [17] and each incident photon has a set amount of energy, E, such that;

$$E = hv = \frac{hc}{\lambda} \tag{1.21}$$

where h is Planck's constant ($6.626 \times 10^{-15}\,\mathrm{J\,s}$), and v, c and λ is the frequency, speed and wavelength of the light respectively. In order to generate an electron-hole pair, each photon must supply energy greater or equal to the semiconductor bandgap. For example silicon (Si) has a bandgap of 1.11eV and would require incident light with $\lambda \leq 1.12\mu$m, whereas gallium arsenide (GaAs) has a bandgap of 1.43 eV and would require $\lambda \leq 868$nm [21].

In addition, the amount of current generated will also depend on the design of the photodetector, or in this case the pixel. The quantum efficiency, η, of a light detection device is the ratio of electron-hole pairs generated given the number of incident photons, and is usually dependent on the light wavelength. Factors such as additional transparent layers and coatings can affect the quantum efficiency. The responsivity of a photodetector, R, indicates the amount of photocurrent generated given the amount of incident optical power at specific frequencies (and therefore wavelengths), and can be calculated using;

$$R = \eta \frac{q}{hv} \tag{1.22}$$

where q is the charge of an electron. The responsivity has units of amperes per watt (AW^{-1}).

To create compact camera devices, all pixels (and surrounding ancillary circuitry) are fabricated on to a small section of semiconductor material. Each pixel con-

tains a dedicated area which is light sensitive; the pixel fill factor describes what proportion of each pixel consists of the photosensitive area. A large fill factor is desirable as this provides a higher conversion from an optical to electronic signal (given a fixed pixel size).

The overall size of the pixel is also important; the pixel pitch is used to describe the distance between the centres of each pixel. For a uniform pixel layout, the pitch is equal to the pixel width and length. Considering a fixed camera chip fabrication area, a smaller pixel size will allow for more pixels in an array, which in turn leads to a potentially higher spatial resolution for any images captured. However, since the photosensitive area has been reduced, less photocurrent is generated (assuming the same amount of incident light), leading to lower signal to noise ratios (section 1.7). The design of camera chips (including the pixel and ancillary circuitry) often take into consideration the trade-offs between resolution and SNR, with particular emphasis put on reducing the noise contributions to small signals from surrounding circuitry [46].

Two commonly used technologies utilised for camera pixel design include the charged coupled device (CCD) or complementary metal oxide semiconductor device (CMOS); these two technologies define the method of pixel addressing and reading.

In a CCD pixel, the incident light generates charge over an integration period, which is collected into a signal bin (i.e. charge collection device) [47]. After the integration period, the collected charge is transferred along the camera array into the next pixel. The pixels closest to the readout stage passes its data onto the output; the information collected by each pixel is read out sequentially. Typical, a CCD pixel can be designed so that most of the pixel area is used to detect light (close to 100% fill factor). The CCD array is manufactured using specialised fabrication processes which are specifically designed to store and transfer charge. It is not designed to have any additional circuitry within the CCD pixel (i.e. any transistors designed using the CCD process would have reduced performance when compared to using the CMOS process [48]). The CCD's simple design, low cost and low noise figures (down to a few electrons over long integration times [49]) made it the preferred camera pixel design technology over most of the 20^{th} century [50].

The initial MOS pixel devices consisted of a photodiode that was 'set' using a transistor [51]. Each photodiode has an inherent capacitance which could be used to store charge. However, once the pixel is selected, the photodiode is connected to the output bus directly, leading to complications such as additional bus capacitances and impedances. This problem was addressed with addition of pixel buffer components [52]. Unlike the CCD type camera, a camera designed with this type of pixel would suffer from a rolling shutter effect (each pixel's information is read one at a time, with no storage outside the read time).

One major advantage of the CMOS architecture is the ability to allow any pixel to be selected; this permits direct access to any pixels. In addition, some of the pixel area could be sacrificed in exchange for additional in-pixel circuitry; this could include amplifiers to improve performance as well as other subsystems that perform 'per pixel' operations. This, in contrast to performing all operations off chip, could improve the integratability of the system and limit exposure of the small signals to external noise.

1.6.3 In-pixel gain

Due to the size of a typical pixel, specifically the photosensitive area of each pixel, the photocurrent generated with light incident would be small, typically between a few picoamps and nanoamps. For example, if the photosensitive section of a single pixel had an area of $2.116\,\mathrm{nm}^2$ (pixel pitch and fill factor equal to $115\,\mu\mathrm{m}$ and 16 % respectively) and background light with an intensity of $1.3\,\mathrm{Wm}^{-2}$ [53] was incident on the camera (2.75 nW per pixel), assuming that the responsivity of each pixel was $0.3\,\mathrm{A\,W}^{-1}$, the pixel would generate $\sim$0.825 nA of photocurrent. Direct analogue-to-digital conversion of this small signal would be unfeasible without gain applied.

The CCD pixel is designed to collect charge generated by incident light within its pixel structure. By adjusting the exposure/integration time each pixel has to the light source, the charge collected changes; signal gain increases with the integration time.

The CMOS pixel gain method varies with the pixel design. The photosensitive

region can be designed like a photogate, which acts like a CCD pixel, storing generated charge over an integration period. The photosensitive component can also be designed like a photodiode, producing a constant photocurrent signal. The current generated can be integrated on to a separate storage component (e.g. a capacitor) implemented into each pixel. However, unlike CCD implementations, it is also possible to amplify the continuously generated photocurrent in each pixel; this requires converting the photocurrent into a voltage. This type of CMOS pixel can either incorporate a linear or a logarithmic frontend scheme.

1.6.3.1 Integrating pixel

Integrating pixel designs use a storage bin in conjunction with the photocurrent generated by the photodetector. As a concept, the pixel can be modelled as capacitor with a photodiode in reverse bias generating photocurrent. If the capacitor, with known capacitance C, is charged up to a known voltage and then allowed to discharge due to the photocurrent generated, i_{pd}, over a known integration time period, dt, then the measured change in voltage, dV, could be used to determine the photocurrent using the capacitor current-voltage relationship ($i_{pd} = C\frac{dV}{dt}$). If the incident light levels are low, increasing the integration time achieves a larger change in voltage given the amount of photocurrent generated.

Since this method requires time to collect charge, frame rates are affected; the lower the light signal, the longer the integration time required to obtain a satisfactory SNR; the method is not suited for the continuous measurement of incident light with a high frequency component. The integrating pixel scheme is ideally suited for CCD arrangements as all pixels collect charge at the same time (before they are serially read out), while CMOS pixels require setting (via addressing) before charge is collected.

1.6.3.2 CMOS linear pixels

One method of implementing a current-to-voltage conversion in a CMOS pixel involves using a linear frontend. As shown in figure 1.9, a linear frontend pixel can be made with a current source, i.e. photodiode, put in series with a resistor.

Under ideal circumstances, the voltage seen at the output of the frontend will fol-

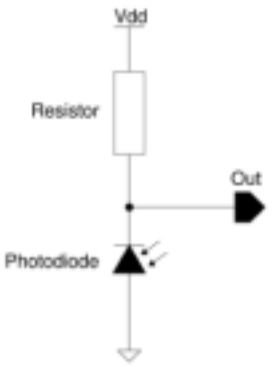

Figure 1.9: Schematic of a simple linear frontend pixel. The photodiode is in series with a resistor. The voltage at the frontend output is linearly related to the photocurrent generated.

low Ohm's law, where the output voltage of the arrangement will be dependent on the resistor value ($V = iR$), and remain linear for all values of the photocurrent.

The linear current-voltage relationship has advantages when detecting a large intensity range, e.g. if an incident optical signal has a large AC amplitude/modulation depth. Determining the generated photocurrent (and therefore incident light intensity) using the output voltage under these conditions is simple. However, given that the amount of photocurrent generated in a pixel is around the picoamp to nanoamp range, the resistance required to produce a workable voltage would be extremely high. For example, in order to output 0.1 mV, a resistor with resistance between 10^6 - $10^9\,\Omega$ is required. Using the AMS C35 fabrication process [54], a $1\mathrm{M}\,\Omega$ resistor would require a silicon square of $35\,\mu\mathrm{m} \times 35\,\mu\mathrm{m}$, whilst a $200\,\mathrm{M}\Omega$ resistor would require a $565\,\mu\mathrm{m} \times 565\,\mu\mathrm{m}$ square [48]. This would be an unreasonable restriction in the pixel design. Additionally, a resistor made this way will not produce a truly linear resistance as parasitic capacitances in the implementation will add frequency dependant impedances to the pixel's frontend response.

1.6.3.3 CMOS logarithmic pixels

An alternative design to the linear frontend for the current-to-voltage conversion, involves using a logarithmic frontend. The frontend of the pixel can be designed using a transistor in series with the photodiode, as shown in figure 1.10.

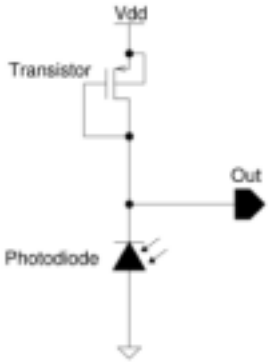

Figure 1.10: Schematic of a simple logarithmic frontend pixel. The transimpedance of the transistor is dynamic, with the voltage at the frontend output having a logarithmic relationship with the photocurrent generated.

The voltage observed at the output in this scheme has a logarithmic relationship with the photocurrent generated. A large transimpedance gain (G × V/I) can be achieved using a small amount of the pixel area. This reduction in the frontend area improves the camera resolution, cost and response speed of the pixel [48,55]. The downside of this frontend implementation is that the output voltage is not linearly related to the photocurrent generated making it difficult to determine the incident light intensity. However, over a small enough photocurrent range, the current-voltage relationship can appear linear.

1.7 Noise and error sources

In the ideal experimental scenario, a detector would be able to exactly measure the intensity of a fringe pattern generated by an interferometer. The detection unit would be able to determine the phase precisely from this measurement, even if the intensity of the optical signal was low. However, in a real system, contributions to the measured signal from internal and external noise sources increase the system output uncertainty, and therefore reduce the accuracy of the system. As noise (and other sources of errors) degrade the performance of a system, it is important to know its cause and, if possible, how to minimise it.

1.7.1 Shot noise

Light can be described as a stream of discrete packets, known as photons, emitted from a source. From every real source, the number of emitted photons (per unit

time) will not be constant, but it can be modelled by its statistical fluctuation. These fluctuations in the number of photons, and therefore variation in measured intensity using a photodetector, is known as the optical shot noise. This noise is not dependent on the quality of the detector and is unavoidable, representing the fundamental limit to detection.

The events causing shot noise increase with the square root of the expected number of events [56](i.e. signal), such that;

$$N_{\text{shot}} = \sqrt{N_{\text{signal}}} \tag{1.23}$$

Increasing the number of collected photons (e.g. increasing integration time or with a high intensity beam), and therefore generated photocurrent, also increases the amount of shot noise. However, the relative proportion of the shot noise decreases with higher intensities (due to the square root relationship), which will increase the signal to noise ratio (considering only the shot noise). Since the optical power of the shot noise is only proportional to the signal power, it is apparent at all frequencies, i.e. shot noise is white noise.

In addition to the optical shot noise, shot noise can also occur in electronic circuitry. Similar to the optical case, electric current can be described as a flow of electrons. The direction of the electron flow is a random process which causes a fluctuation in the observed current [57]. The shot noise can be described;

$$i_{\text{shot}} = \sqrt{2qi_{\text{signal}}\Delta f} \tag{1.24}$$

where q is the electron charge, i_{signal} is the signal current, and Δf is the signal bandwidth. Again, at high signal intensities, relative shot noise ($i_{\text{shot}}/i_{\text{signal}}$) decreases. Since each pixel in a camera only generate small amounts of current, electronic shot noise could be the dominant source of noise on a single captured image. Additionally, since it is not dependent on the temperature (thermal noise) or operation frequency (flicker noise), it cannot be eliminated by operating the system at a high frequency and low temperature. Increasing the measured intensity for an image capture (e.g. increasing integration time on a CCD) or averaging multiple images (to reduce the random variations) are, techniques that could be implemented.

1.7.2 Thermal noise

Thermal noise (or Johnson-Nyquist noise) occurs due to random motions of electrons in resistive materials [58]. This causes small voltage fluctuations, V_{thermal}, on the system's terminals, such that;

$$V_{\text{thermal}} = \sqrt{4K_B T R \Delta f} \tag{1.25}$$

where K_B is the Boltzmann constant (1.38×10^{23} $\text{J}\,\text{K}^{-1}$), T is the absolute temperature, R is the resistance and Δf is the bandwidth of the signal; there is no current term in equation 1.25, so thermal noise will be present in a system even if there is no signal. At higher temperatures, an increase in electron motion occurs, which will in turn increase the amount of thermal noise. Therefore, methods of reducing the system temperature could be used to reduce thermal noise (e.g. heat sinks, exhaust fans, liquid cooling, etc). In electronic systems, thermal noise could be considered to be a white noise source (uniform power contributions at all frequencies up to ~6000 GHz [59]) and operating a system at different frequencies would not affect the thermal noise contribution (although a limitation of the operational bandwidth could reduce the overall thermal noise).

1.7.3 Flicker noise

Flicker noise is present in all semiconductor devices and occurs due to resistance fluctuations in silicon, and crystal defects in diodes and transistors [60]. This in turn creates voltage or current fluctuations (considering Ohm's law). Flicker noise is dominant at low frequencies [61], such that;

$$i_{\text{flicker}} = \sqrt{K \frac{{i_{\text{signal}}}^{\alpha}}{f^{\beta}} \Delta f} \tag{1.26}$$

where K, α and β are fabrication process dependent parameters, i_{signal} is the signal current, f is the signal frequency, and Δf is the system bandwidth. The contributions from flicker noise decreases as the system frequency increases. The reduction of flicker noise in the detection unit is one key advantage of using a heterodyne interferometer system over a homodyne system.

In detection, the flicker noise appears as a low frequency phenomenon and at higher frequencies it can be overshadowed by noise from other sources; the corner frequency where flicker noise is no longer considered dominant is often used as an

electronic device design parameter. This frequency is illustrated in figure 1.11. The corner frequency, f_c, of a component fabricated on a semiconductor [62] can be determined using;

$$f_c \propto \frac{K}{C_{ox}WL} \tag{1.27}$$

where K is a process parameter, C_{ox} is the oxide capacitance, and W and L is the width and length of the device. Since the process parameter and the oxide capacitance is dictated by the fabrication process and semiconductor properties, decreasing the flicker noise corner frequency can be implemented by designing a larger device.

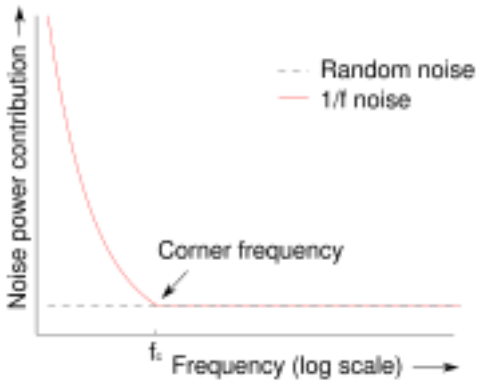

Figure 1.11: An example plot of the noise contribution to a system. In this plot, at low frequencies ($< f_c$) the dominant form of noise is flicker noise. At high frequencies ($> f_c$) the flicker noise is sufficiently low so that random noise from other sources, such as from thermal and shot noise, becomes the dominant source of noise.

1.7.4 Fixed pattern noise

Even though each pixel in a camera array has the same design, each component in the pixel can have slight variations in its performance. This generates errors known as the fixed pattern noise (FPN) in the output image. The variation seen in each pixel is caused by factors such component layouts and fabrication process parameters; careful design of components can reduce FPN [46]. Each stage of the camera circuitry can add further contribution to the FPN and can produce distinct glitches in the image. For example, where readout and amplification circuitry is designed in columns, distinct vertical patterns would emerge in the

output image. Since the FPN causes systematic errors in the image, it is possible to calibrate the camera by capturing an initial FPN image and subtracting mismatched values from subsequent images in order to reduce FPN.

1.7.5 Vibration and microphonics

In an interferometer system, temporal phase shifts observed in an interferogram can be attributed to changes in a beam's optical path length (OPL) within the sub-wavelength region (i.e. nanometres). If the physical interferometer arrangement is subjected to even tiny amounts of vibration (microphonics), the phase accuracy of the system will be affected (e.g. an OPL offset of $\frac{\lambda}{2}$ causes a constructive interference pattern to change to a destructive pattern).

If the vibration frequency is much higher than the image acquisition rate, the net result would be a reduction of fringe pattern visibility; the fringe visibility is dependent on the vibration amplitude (in addition to other factors such as coherence, polarisation, etc). This reduction equates to $J_0\left(\frac{2\pi}{\lambda}A\right)$ of the intensity in an otherwise stationary system (where J_0 is the Bessel function of order 0 of the first kind, and A is the amplitude of optical path length variations [63]). The equation suggests that the first zero in the visibility occurs when the vibration amplitude is $\sim 1.2\lambda$ (no fringe visibility with this amount of vibration). Beyond this amount, there is an induced sign change in the visibility, indicating an inversion of the fringe contrast. For systems where the vibration is unknown, random, or time varying in frequency or amplitude, interpreting the fringes becomes difficult at higher vibration amplitudes.

Environmental influences to an interferometer are not just limited to vibrations, continuous changes in the propagation medium (e.g. from a slight breeze or fumes) or change in medium density (e.g. due to a temperature difference in the arms of the interferometer) could also cause an unwanted phase variations in the measured interferogram. Methods of stabilising an interferometer can be achieved by physically modifying the setup, for example, reducing environmental factors such as temperature changes and vibration [64], or through the use of sensors and feedback into the systems mirrors to counteract unwanted OPL changes [65, 66]. Interferometer arrangements with self-referencing (e.g. common-path) could also be used to produce a stable interferogram (discussed further in section 1.5 and

section 2.3).

1.8 Project summary

The work presented in this thesis explores the use of modulated light cameras (MLCs) to produce widefield heterodyne interferograms. The flow chart shown in figure 1.12 depicts the direction of ideas used to produce the interferometer systems presented in this thesis.

Figure 1.12: A flow diagram showing the ideas used in implementing the interferometer systems discussed. The camera is used to capture widefield heterodyne interferograms. Modifying the setup produces an ultrastable configuration, which can be used to capture two laser interferograms.

Standard digital cameras are suited to capturing homodyne interferograms since the frame rate is not critical if a steady fringe pattern is incident. Conversely, a point detection system is commonly used for capturing heterodyne fringe patterns as it has the required frequency response to detect the modulated optical signal and the system only needs a single demodulation circuit and ADC.

A modulated light camera is designed to capture modulated light and demodulate the high frequency contents of incident light; the measurement outputs include the DC intensity, AC amplitude and/or the phase offset (relative to a reference signal). The cameras are designed to output data with a frame rate comparable with regular digital camera devices. The demodulation process is conducted on each pixel of the MLCs.

The motivation behind developing the first system presented in this thesis was to demonstrate that widefield images of heterodyne interferograms can be captured using an MLC. If the assumption is made that the MLC camera becomes mass-producible, then a user designing an interferometer system does not need to make the choice between reduced low frequency influence (i.e. point-detection heterodyne) and real time widefield imaging (i.e. widefield homodyne), the system presented in this initial concept experiment can do both.

The second system developed was the ultrastable widefield heterodyne interferometer. In this system, the modulated optical signal detected by a single pixel was fed back into the camera and used as the demodulation reference signal, effectively making the interferometer system electronically self-referenced. This makes the captured interferogram immune to the effects of piston phase change (e.g. due to vibrations); a key trait of common path interferometers. However, the ultrastable system retains the availability of a separate reference signal (e.g. for boosting the optical signal) as well as keeping the interferometer arrangement simple and inexpensive. A user deciding to use either a C-P or D-P interferometer for their respective advantages, can alternatively use this ultrastable system.

As an extension to the ultrastable system, a third interferometer system was developed to capture the fringe pattern generated by two separate lasers. The unknown and randomly varying optical frequency difference between the two incoherent sources was tracked using a single pixel on the MLC and used as the demodulation reference signal (as long as the optical frequency difference is within the MLC operation bandwidth). A major constraint of an interferometer design is the light coherence restriction, e.g. the temporal coherence for single split source interferometer will limit the optical path length difference between the arms. This system employs a major relaxation in the coherence requirement for the light source, such that the interferograms generated by two separate laser

can be captured; interferometers can be designed with this de-restriction in mind.

1.8.1 Structure of thesis

Chapter 2 gives a review of systems that could be used to acquire the phase of incident modulated light in the widefield region. A review of developed modulated cameras is given. Reviews of interferometer systems that produce stable interferograms and of two laser interference systems is also given.

Chapter 3 gives an overview of the MLC camera used to capture the interferograms produced. This includes an outline of the key components used in each pixel for capture and demodulation, and an analysis of the camera's performance. The chapter also details components used in the various interferometer arrangements presented in this thesis, as well as the interface system used to obtain images from the MLC chip.

Chapter 4 explores the widefield interference patterns captured using the MLC. The first set of results show the MLC capturing both homodyne and heterodyne widefield interferogram images. Next, using the knowledge of incident wavefronts (in one setup of the interferometer), a theoretical fringe pattern was generated; a measured interferogram is compared with the theoretical pattern. Finally, a phase shift induced along part of one arm in the interferometer was captured as a proof-of-concept experiment.

Chapter 5 explores the main aim of this thesis; the ultrastable interferometer system. The theory of temporally changing phase, which could relate to unwanted vibration for example, is modelled into the operation of the system. An explanation of how a signal feedback is used to cancel out these effects is presented. Experiments are conducted by introducing a fast changing OPL (relative to the frame rate) into the interferometer (i.e. vibration) and the physical stability limits of the system are determined. Experiments are also conducted simulating the effects of vibration to determine extended stability limits. The results where the characterisation of a profiled object determined using the ultrastable interferometer, are presented.

Chapter 6 explores a novel two laser interferometer system using the MLC. Using

the ultrastable system, interferogram images are captured, even though the beat frequency generated by the two lasers is unknown (required for many demodulation techniques). The effects of the varying modulation frequency on the MLC and the images produced is also discussed.

Chapter 7 summarises the work presented in this thesis and discusses the merit of the MLC in heterodyne interferometers; specifically in its ultrastable configuration.

1.9 Publications based on this project

R. Patel, S. Achamfuo-Yeboah, R. Light, and M. Clark, "Widefield heterodyne interferometry using a custom CMOS modulated light camera," Optics Express **19**, 24546–24556 (2011).

R. Patel, S. Achamfuo-Yeboah, R. Light, and M. Clark, "Ultrastable heterodyne interferometer system using a CMOS modulated light camera," Optics Express **20**, 17722–17733 (2012).

1.9.1 Pending publication on this project

R. Patel, S. Achamfuo-Yeboah, R. Light, and M. Clark, "Two laser interferometry"

Chapter 2

Literature review

In this chapter, a review of modulated light cameras (MLCs) is given with an explanation of their operation. Key specifications of the cameras are provided as a summary. This chapter will also reviews interferometer systems that are analogous to the experimental systems described in this thesis. These include heterodyne interferometer systems that capture widefield fringe patterns, interferometer systems that produce stable phase measurements using electronic signal feedback, and widefield two laser interferometer systems.

2.1 Modulated light cameras

Modulated light cameras (MLCs) is a term given to detection units capable of capturing, storing (if necessary) and demodulating incident modulated light signals. The aim of these cameras is to determine the phase of modulated light and are primarily used for 3D ranging [67] or LIDAR (light detection and ranging) [55]. The incident signal produced in LIDAR has a similar form to that observed in heterodyne interferometry (equation 1.17). A LIDAR system is used to measure distances within the range of the modulated signal's wavelength, as opposed to the optical wavelength in interferometry. Due to the high modulation frequencies used in these ranging applications (e.g. emitted modulation frequency of 15 MHz gives an imaging range of 10 m [55]), direct image capture using commercially available cameras will not provide the necessary frequency response or a demodulation method. One key factor to note is that the techniques used in an MLC configuration is not limited to just the pixel/camera design, for example some methods use external gated structures (such as slit masks) to control expo-

sure [32] or use lock-in amplifiers [33] to control when pixels begin integration [68].

2.1.1 CCD lock-in arrangements

2.1.1.1 Stenflo and Povel

The first implementation of a lock-in pixel for detecting modulated light was described by Stenflo and Povel [68]. The intended use for the arrangement was in the field of polarimetry (measurement of the polarisation state of transverse waves as it propagates through or reflects off an object). The technique involved attaching a lock-in amplifier to a single pixel in order to initiate integration. As the single pixel used an external demodulator, a comparative multi-pixel system would be slow; the read rate of the CCD pixel was limited to 5 MHz. In a serial read-out arrangement for example, a 32×32 pixel array taking two samples per pixel per modulation period would have a maximum detectable modulation frequency of about 2 kHz. In contrast, parallel read-out arrangements would be large, power intensive, and costly due to the requirements of the multiple lock-in amplifiers.

A potential pixel array solution described by Povel involved using a slit mask to expose (and block) light to alternate rows of a commercially available CCD camera (385×288 pixel array) [32]. The technique used the CCD camera's charge transfer method in order to make two measurements per modulation period, demonstrating how a CCD could be used directly as a demodulator. In the first half cycle of a modulation period, light was integrated on exposed rows (no exposure on blocked rows). Charge on each pixel was transferred down one row (i.e. into shielded rows) and during the second half-period, the light was integrated onto the exposed pixels (previously contained covered row data). This cycle could be repeated (i.e equivalent to increasing the integration time) until the pixels are read out. The two results obtained per 'pixel' were used to calculate the amplitude of the modulate light. The technique was used to measure modulated light with frequencies of 50 kHz and 100 kHz. However, this technique suffered from misalignment problems with the slit mask (e.g. in the presence of vibration) and required two pixels to measure modulated light at one position (loss of spatial resolution).

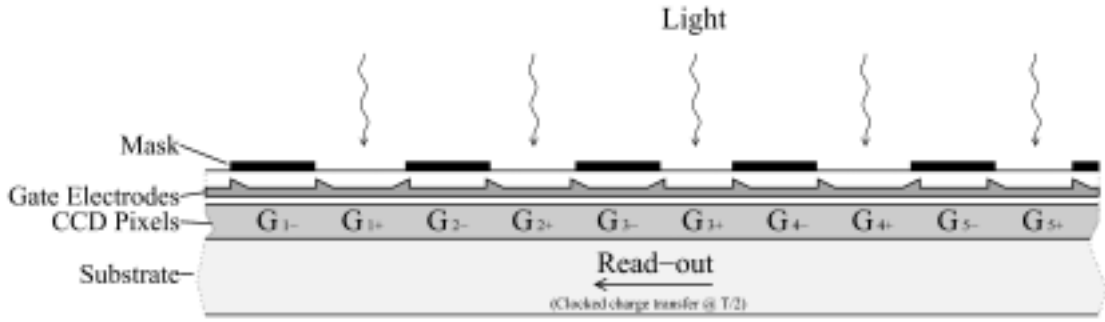

Figure 2.1: Diagram of Povel's slit mask CCD design (Povel et. al 1990 [32]). Light falls on unmasked pixels (G+), integration begins in the first half modulation period. Integrated charge is then transferred to the masked pixels (respective G- pixels) and integration begins for the second half of the period in the now empty pixel. Extended integration times can be achieved by transferring charge back and forth before frame read-out.

2.1.1.2 Spirig and Lange

If a demodulation technique takes only two samples per modulation period, it is possible to determine the amplitude and the offset of modulation signal (as long as phase difference between the reference and incident signal remains constant). Spirig improved on the lock-in pixel design by increasing the number of samples taken per modulation period from two to four [69], making the extraction of phase possible (section 1.3.6). A custom fabricated 3×3 CCD pixel array with a fill factor of 17 % and pixel size of 87.5 μm×80 μm was produced. Each pixel consisted of a single photosensitive area (a photogate) with four storage gates. The transmission gates between the photogate and storage gates on each pixel controlled where, and critically, when the integrated charge was stored. The pixel arrangement was able to demodulate at 100 kHz but it was suggested that a CMOS equivalent design would be able to demodulate signals up to 30 MHz.

This concept was investigated further by Lange for the purposes of ranging using modulated light [67]. The time-of-flight ranging concept uses pulses or a stream of pulses (e.g. modulated light) to determine the distance between a reflecting object and measuring device, depending on the measured phase, speed of light and modulation frequency [70]. The 64×25 pixel array device described by Lange used a combination of CCD photo-collectors and CMOS readout integrated circuits (ROICs). The arrangement reported a demodulation frequency of up to 20 MHz.

2.1.2 CMOS integrating cameras

2.1.2.1 Ando and Kimachi

The equivalent CMOS-only implementation of a lock-in camera was first described by Ando [71]. The 100×100 pixel array arrangement was similar in function to Povel's system (section 2.1.1.1) in that the current generated by the pixel photodiode was used to charge one capacitor (i.e. signal bins) over half a modulation period and another capacitor over the other half modulation period.

This design was improved by Ando with a 64×64 pixel array implementation that made three measurements per modulation period (known as the three-phase Correlation Image Sensor (CIS)) [72]. This is the minimum number of measurements required for unambiguous phase determination from an incident modulated signal (section 1.3.6). The pixel arrangement (illustrated in figure 2.2) shows transistor switches connected to storage capacitors where the three local signals used to begin charging have the same frequency as the incident modulated signal but with 120° phase difference between them.

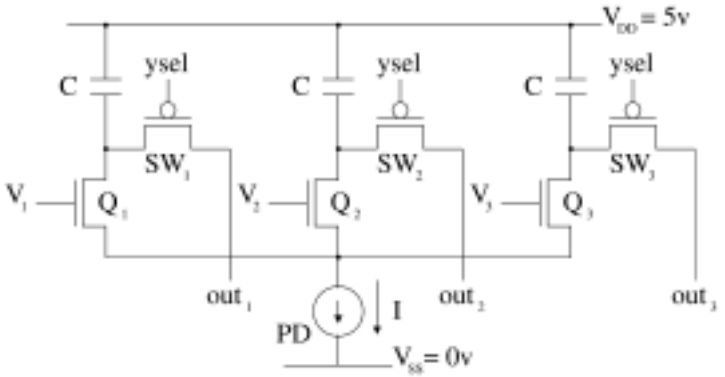

Figure 2.2: A schematic of Ando and Kimachi's three phase CIS pixel design (Ando and Kimachi 2003 [72]). To extract the phase, three measurements of the intensity are made per modulation period (out_1, out_2, out_3). Capture of photo-charge is controlled using signals (V) to line switches (Q) and each line is read-out using the select switch (SW). The phase can be determined using the equation $\phi = \arctan\left(\frac{\sqrt{3}(out_2 - out_3)}{2out_1 - out_2 - out_3}\right)$.

Building on this, Kimachi produced a 200×200 array camera for use in tomography [16]. The system was reported to work with a beat frequency of 25 kHz and

was able to produce 30 frames s^{-1}.

2.1.2.2 Schwarte

The commercially available photonic mixer device (PMD) was conceived by Schwarte [73]. The demodulation of an incident signal is implemented through square wave mixing. A schematic of the pixel is illustrated in figure 2.3. The pixel arrangement includes two reverse biased photodiodes, where each photodiode can be read as a normal single photodiode. If the control voltage applied to the transparent gates is equal, the photocurrent is split equally. However, if the control voltage to gate is different, the photocurrent tends towards the more negative gate. Applying local signals with a phase difference (i.e. 180°) to the gates, the device will produce switched outputs with the same phase difference. The outputs of the frontend is integrated onto storage capacitors. The current generation of PMD camera (2012) produce three outputs for phase determination, demodulates at 15 MHz in a 204×204 pixel array camera [74], and is used for range finding purposes.

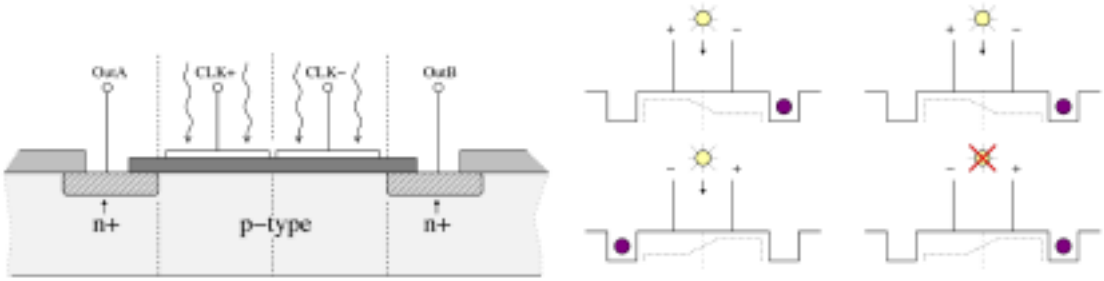

Figure 2.3: A diagram of the PMD pixel design (Schwarte 1997 [73]). The pixel consists of two reverse bias photodiodes (shown in left image). The voltage at the transparent control gates (CLK+/CLK-) can be used to direct the generated photocurrent towards either end of the diode (as shown in right image). Applying a voltage signal with different phases (with the same frequency as the incident modulated light) produce switched outputs at OutA and OutB.

2.1.2.3 Stoppa

A 80×60 pixel array camera designed by Stoppa used buried channel photodetectors [75]. The operation of the pixel was similar to the PMD camera (section 2.1.2.2), but differs in that, instead of using surface channels, buried channels were used. Using the 0.18 μm CMOS process, each pixel had a fill factor of 24 % and a pitch of 10 μm; a maximum demodulation frequency of 50 MHz was achieved at 20 frames per second.

2.1.2.4 Light

Roger Light designed a custom camera using the 0.35 μm CMOS process [48] where each pixel integrated the incident modulated light using storage bins. The output of the pixel was connected to a comparator. The time taken for the storage bins to reach a certain voltage was measured and that time was used to determine phase information. The 128×128 pixel camera array was able to detect modulation frequencies of up to 2.5 kHz.

2.1.3 CMOS continuous-time cameras

2.1.3.1 Benton

Benton described the concept of a CMOS pixel for use in measuring blood oxygenation and dental pulp vitality; the pixel demodulated light using square wave mixing [76]. The pixel consists of two photosensitive channels for detecting two different modulation signals. The system allows simultaneous detection of light signals of two different modulation frequencies. The detected signal was fed into a switching multiplier which would multiply the input by +1 or -1 at a frequency equal to the light modulation frequency. A low pass filter was implemented to remove all harmonics apart from the DC (output voltage proportional to the amplitude). The system used modulated light with frequencies of between 50 Hz and 40 kHz. The application involved making measurements within the mouth, however, the pixel had an area of 2.9 mm × 0.45 mm; the described method used optical fibres to make measurements.

2.1.3.2 Bourquin

A camera design described by Bourquin used a 58×58 pixel array where each pixel consisted of a photodiode, voltage controlled current source, amplifier, square-wave mixer and a low-pass filter [77]. To perform the square wave mixing, the detected analogue signal was fed to a phase controlled rectifier circuit, before being low pass filtered. The operation of the camera was similar to the system described by Benten (section 2.1.3.1) with the addition of a feedback loop between the filter and the amplifier to ensure that the amplifier was operating under optimum conditions (gain was adjusted on a pixel by pixel basis). The camera was capable of detecting signals with modulation frequencies from 1 kHz to 1 MHz. The pixel had a pitch of 110 μm.

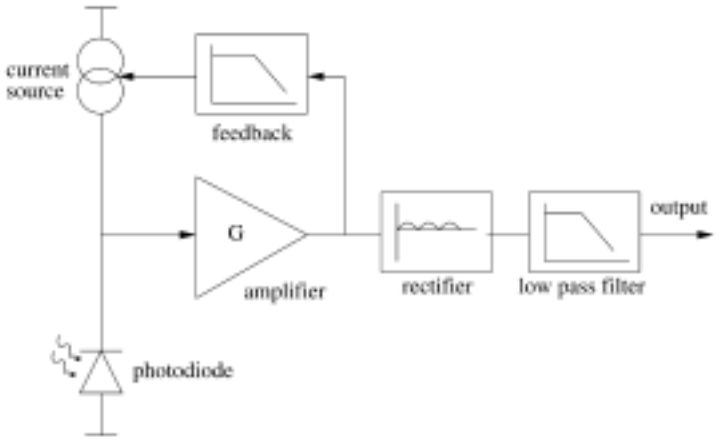

Figure 2.4: Schematic of Bourquin's smart pixel (Bourquin et. al 2000 [78]). The detected photocurrent is amplified and square wave mixed using the rectifier circuit. The low pass filter provides the DC output. A feedback circuit is used to maintain optimal amplifier conditions.

2.1.3.3 Lu

Lu presented a continuous time pixel which used a buried double junction (BDJ) detector as the photodetector [79, 80]. In addition, the pixel contained a transimpedance amplifier, differential amplifier, mixer and a low pass filter. As BDJs are sensitive to different ranges of wavelengths (due to differing junction depths), the pixel was capable of differentiating between two modulated signals. However, the single pixel was relatively large and power intensive (an area of at least 2.5 mm^2 and power consumption of about 20mW [55]), making it unsuitable for a full-field camera array.

2.1.3.4 Pitter

Pitter produced a 4×4 pixel array for measuring modulated thermo-reflectance (measuring the reflectivity of temperature dependent materials) [81]. Each pixel used a logarithmic frontend, with the captured signal mixed using two channels of switched capacitors (for the in-phase (I) and quadrature (Q) phase signals) and integrated onto signal bins. Each signal was sampled once per modulation period (set time in the modulation period). The frontend of the pixel produces a continuous time signal, however this signal integrates onto another capacitor using a reference signal. Each pixel was 200 μm by 200 μm in area with a 9% fill factor.

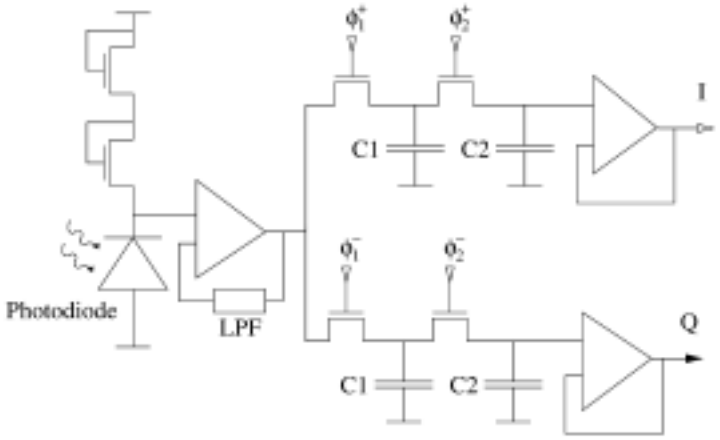

Figure 2.5: Schematic of Pitter's modulated light pixel (Pitter et. al 2003 [81]). The frontend of the pixel captures a continuous modulated signal and the signal is sampled at specific points within each modulation period using ϕ_1^+ and ϕ_1^-. It is integrated onto capacitor C1. For read-out, a signal is applied in ϕ_2^+ and ϕ_2^- for the I and Q output respectively.

This design was followed up by a 64×64 pixel array [82]. In this implementation, the camera was designed to be column based (rather than individually pixel based); one entire row was selectable at a time (64 pixels). The amplification, filtering and demodulation, was performed outside of the pixel, with the selected row of pixels sharing the same signal processing circuitry. Due to this separation of photosensitive element and circuity, the size of the pixels was smaller at 25 μm × 25 μm with a fill factor of 56% at a cost of a lower frame rate (a larger integration period was required in this arrangement).

2.1.3.5 Dmochowski

An initial pixel design by Dmochowski used a continuous wave mixer with two channels [83]. The emphasis of this test pixel design was on high frequency demodulation. The pixel used a logarithmic frontend with a regulated cascode circuit (multi-stage current amplifier arrangement used to increase bandwidth), allowing it to demodulate light from 500 kHz to 25 MHz. Each pixel was independent, containing the amplification, mixing, and low pass filtering circuits. However, the fill factor was only 4 %, and was designed with a pixel pitch 180 μm.

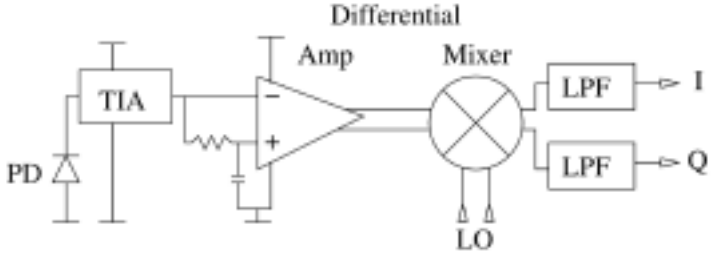

Figure 2.6: Schematic of Dmochowski's pixel (Dmochowski et. al 2004 [83]). Continuous photocurrent is amplified using transimpedance and operation amplifiers. The signal is mixed with in-phase and quadrature phase local reference signals using a Gilbert cell. The output signals are low pass filtered to produce DC, I, and Q outputs.

Further to this design, Dmochowski designed a camera with a 24×32 pixel array, called MLCv5 [84], with a decreased pixel pitch of 130 μm and increased fill factor of 5.4 % (and with a decrease in pixel power consumption of 200 μA). An increase in the demodulation frequency bandwidth of between 10 kHz and 30 MHz was reported. The use of a logarithmic frontend however posed problems with non-linear output responses (i.e a large variation in gain and phase response) which restricted the DC and AC intensity range of the incident light (discussed further in section 3.1.3.1).

2.1.3.6 Achamfuo-Yeboah

Samuel Achamfuo-Yeboah created two test designs before producing the final camera that was used for the work presented in this thesis [55]. The first was a continuation of Dmochowski's design, named MLCv6FE. The single pixel fabrication comprised of a logarithmic frontend with a regulated cascode circuit. The

motivation behind the design was to force the pixel response up the logarithmic curve so that the response appeared linear (through adding a bias current in with the photo-detector current). This allows for an increase in the range of AC input amplitudes. The MLCv6FE frontend had a pixel size of $40\,\mu$m$\times 40\,\mu$m and was able to demodulate light up to 13 MHz.

The next iteration of this design was the successor to Dmochowski's MLCv5 camera; a 32×32 pixel array camera using the MLCv6FE test pixel design, named MLCv6. The chip was setup in 8 banks of 4 columns, with 4 pixels in the centre capable of outputting the raw measured signal (known as the RFout). A smaller fabrication process was used [54] along with shared current mirrors, which allowed for a more compact pixel. The bias current could also be manually changed to allow for a larger intensity capture range. However, the chip had a pixel read design flaw; it was possible to create a workable image, but with significantly increased noise (compared with the design simulations).

2.1.4 MLC review summary

A brief summary of the MLC camera arrangements discussed in this section is presented table 2.1 and includes each systems key specifications.

2.2 Widefield heterodyne capture techniques

If a widefield image is captured in real time using a pixel array, both spatial (limited by the pixel number) and temporal (limited by frame rate) variations in a phase pattern can be determined. This is in contrast to point detection schemes, where the frame rate is limited by the scanning setup (i.e. mechanical translations [14]). Using camera arrays to detect widefield homodyne fringe patterns is common place. However, capturing widefield heterodyne interference patterns becomes a challenge (discussed in section 1.3.3). The interferometer arrangements and detection schemes described below produce real time acquisitions of heterodyne interference fringe patterns in the widefield region. The systems use a variety of different demodulation techniques.

One common use for widefield interference pattern capture is in the field of surface

Author	Year	Pixel arrangement	Max. Mod. freq.	Measurements
Stenflo [68]	1985	Single pixel CCD	5 MHz	Amplitude
Povel [32]	1990	385×288 CCD	100 kHz	Amplitude
Spirig [69]	1995	3×3 CCD	100 kHz	Amplitude + Phase
Lange [67]	1999	64×25 CCD	20 MHz	Amplitude + Phase
Ando [72]	1999	64×64 CMOS intg.	10 kHz	Amplitude + Phase
Kimachi [16]	2010	200×200 CMOS intg.	25 kHz	Amplitude + Phase
Schwarte [74]	1997	204×204 CMOS intg.	15 MHz	Amplitude + Phase
Stoppa [75]	2011	80×60 CMOS intg.	50 MHz	Amplitude
Light [48]	2008	128×128 CMOS intg.	2.5 kHz	Amplitude + Phase
Benten [76]	1997	Single pixel CMOS cont.	40 kHz	Amplitude
Bourquin [77]	2001	58×58 CMOS cont.	1 MHz	Amplitude
Lu [80]	2000	Single pixel CMOS cont.	10 Hz	Amplitude
Pitter [82]	2003	64×64 CMOS cont.	2 kHz	Amplitude
Dmochowski [84]	2004	24×32 CMOS cont.	30 MHz	Amplitude + Phase
Achamfuo-Yeboah [55]	2012	32×32 CMOS cont.	13 MHz (50 MHz with bias)	Amplitude + Phase

Table 2.1: Table summarising key factors, including the number of pixels, maximum modulation frequency, and measurements possible, for the MLCs reviewed in this section.

profilometry. Interferometry can be used to measure small height variations on the surface of an object (i.e. interpreting OPL variations across the cross section of a reflected beam).

2.2.1 Massie

One of the first implementations of a real-time heterodyne interferometer system was developed by Massie [85]. The presented system was capable of making direct measurement of the optical path difference between interferometer arms without the requirement to interpret the fringe pattern (as discussed in section 1.3.4). The system used a zero-crossing phase-meter; the phase-meter produced an analogue voltage depending on the time difference between two signals (reference/measured) crossing a 'zero' point (which would be proportional to the phase difference). The phase-meter was capable of achieving a phase accuracy of $\sim \lambda/1000$.

The interferometer was a combination of modified Mach-Zehnder and Twyman-Green interferometers. Light emitted from a laser entered a Mach-Zehnder interferometer. The beam was split into test and reference arms. Each arm passed

through acousto-optic modulators or AOMs (discussed further in section 3.2.2), which were driven at 43 MHz and 42 MHz, shifting the optical frequency of the reference and test beams by these frequencies. The test beam passed through a half-wave waveplate before both arms exited the Mach-Zehnder arrangement through a beamsplitter. The arrangement produced optical outputs similar to those emitted from a Zeeman laser (two beams with different frequencies and polarisation planes [86]), however, this arrangement allowed for greater control over the frequency difference and intensities.

The two beams entered a Twyman-Green interferometer, passing through linear polarisers before the interference occurred. The modulation frequency of the interference pattern was equal to the 1 MHz differential between the optical frequency shifts. The reference signal for the phase measurement was obtained by using a detector located at a stationary point on the fringe pattern (discussed further in section 2.3.1) and the test image was obtained by scanning another detector (mounted on to an X-Y stage) across the pattern.

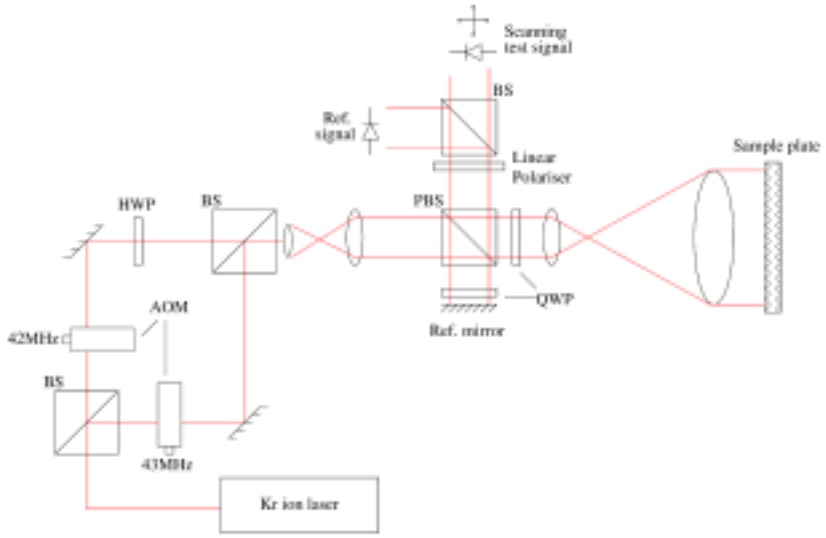

Figure 2.7: Optical arrangement of Massie's interferometer system (Massie et. al 1979 [85]). The light from a Kr-ion laser was split, with each beam arm frequency shifted by 42 MHz and 43 MHz. The arms were orthogonally polarised and reflected off a reference mirror and sample plate. After passing through a linear polariser, the interference pattern was captured using a scanning photodetector. Part of the fringe pattern was measured using a fixed photodetector and used as the reference signal.

The interferometer used a 100 mW Kr-ion laser ($\lambda = 647.1$nm) and a computer

(HP9825A) to control the motors and data recording. The phase detectors required multiple modulation periods to produce an accurate phase value (at 1 MHz, 300 ms was required per data point), with a phase accuracy of $\lambda/100$ demonstrated. An improved single point system was demonstrated with a serial data acquisition rate of 50 μsec/point and a system with a spatial resolution of 500 points/line (5 seconds for a total of 100 frames) [87]. A phase accuracy of $\lambda/70$ was achieved.

A widefield version of this system was constructed using a multiple photodetector/phasemeter combination to construct a phase image across two dimensions [15]. The system was equipped to simultaneously measure and record phase at 64 discrete locations. The measurements were obtained at 10 μs time intervals with a phase resolution of $\lambda/100$. Each phase detector had a dedicated data recording system (each point generated data 16-bits wide and 4096 words deep, each run of capture produced ~500 kB of data). A set of optical fibres (connected to the 64 photodetectors) were arranged across the generated heterodyne fringe pattern in a cross pattern (32 vertical, 32 horizontal) although it could also have feasibly been arranged in a 2D 8×8 matrix. Two great challenges were faced in the construction of this instrument; the authors noted that there was difficultly in mounting the fibres in a closely packed array and processing the considerably large amount of data generated (at a 100K frame rate, 10 MB/s of data required transferring and storage, a massive undertaking in 1983). Ultimately, large imaging systems like the described system become prohibitively expensive and complex as both the number of data points and frame rates increase. Practically, widefield heterodyne capture schemes require pixel (ideally single chip) based detection methods.

2.2.2 Akiba

A heterodyne detection technique developed by Akiba demonstrated capture of real-time cross sectional phase images in an optical coherence domain reflectometry (OCDR) application [88]. This technique measured the depth of surface reflectance by detecting the degree of interference using a low coherence light source. The system used a frequency synchronous detection scheme, similar to the system described by Stenflo (section 2.1.1.1). The interferometer arrangement was a modified Mach-Zehnder, with the test and reference arms frequency shifted, using AOMs, by 79.94 MHz and 79.90 MHz respectively. This generated

a beat frequency of 40 kHz when they interfered.

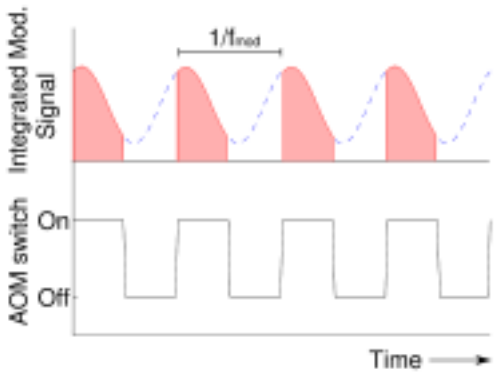

Figure 2.8: Example plot of an integrated beat signal. The signal used to drive the AOM was switched on-off at the f_{mod} frequency. The modulated fringe pattern is integrated on a CCD camera only when the AOM is switch on. The presented system was similar to system described by Stenflo (section 2.1.1.1).

The author noted previous attempts of this demodulation technique used two pairs of liquid crystal shutters, however, these instruments were difficult to obtain commercially and had introduced alignment problems. In this arrangement the capture gating effect was produced by switching the AOMs on-off using a pulse train with a frequency equal to modulation frequency of fringe pattern.

The presented system used a superluminescent diode (central wavelength $\lambda = 813\,\text{nm}$, spectral bandwidth FWHM $\Delta\lambda = 16\,\text{nm}$) and a commercially available 640×480 pixel CCD camera. The CCD had a frame rate 30 fps, and as three frames were used to determine phase, a phase image could be obtain in 0.1 s.

This system was later adapted for full-field optical coherence tomography (OCT), an interferometric technique similar to OCDR which uses back-scattered light from a sample to determine depth through OPL (depth) and coherence [89]. The proposed system employed a pair of CCD cameras to detect the in-phase and quadrature components of the heterodyne signal simultaneously. The interferometer was setup in a Michelson arrangement. The resultant beam from the arrangement was split and passed through through liquid crystal shutters (LCS) for gating at the modulation frequency; there was a phase difference between the two LCS signals of 90°. This system used faster cameras than the previ-

ous attempt and was capable of 100 fps in a single longitudinal scan. The author noted a signal to noise ratio of approximately 85 dB with 1 mW of incident power.

2.2.3 Bourquin

The modulated light camera presented by Bourquin (section 2.1.3.2) was presented in a heterodyne low-coherence reflectometer application (i.e. similar to the OCT) which was based on a conventional Michelson interferometer [77, 78]. The novelty of this system was the use of the 'smart pixel' camera to capture and demodulate the heterodyne signal. The modified Michelson interferometer arrangement used a superluminescent diode (central wavelength $\lambda = 850\,\text{nm}$, spectral bandwidth FWHM $\Delta\lambda = 20\,\text{nm}$) with the beat signal in the generated fringe pattern achieved by varying the optical path length of the reference arm using a mirror mounted on a speaker.

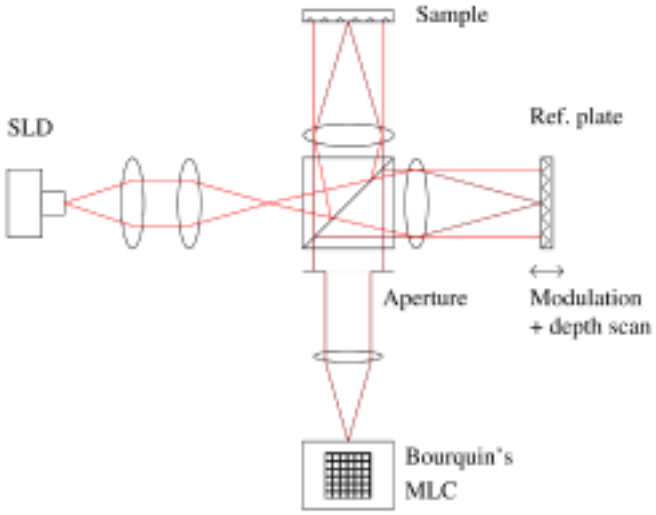

Figure 2.9: Schematic of Bourquin's low-coherence reflectometer. Interference only occurs when the path length difference is within the small coherence length of the source. The light is modulated using a moving reference plate, which is also used to perform a depth scan. Bourquin's smart pixel array is used to capture the heterodyne interference pattern.

A symmetric sawtooth waveform was applied to the mirror mounted speaker, producing a pattern modulation with a frequency of 3.7 kHz. The MLC (discussed in section 2.1.3.2) plus the ancillary electronics had a reported frame acquisition time of ~3.36 ms (~300 fps). The system created a 3D map of reflectances from a sample through depth scanning (i.e. frame grab traverse layer by transverse

layer). The detection limit of the system was reported as being 7.2 dB above the shot noise limit.

2.2.4 Pitter

A heterodyne interferometer microscope arrangement presented by Pitter captured full-field phase images using a combination of a modified Mach-Zehnder and Michelson interferometer [90]. The Mach-Zehnder generated an object and reference beam, which were orthogonally polarised and frequency shifted using AOMs to have a 1 Hz optical difference (i.e. beat frequency), similar to the setup used by Massie. At the entrance of the Michelson interferometer, the light was scattered using a rotating diffuser such that the reference and object beams were temporally coherent but spatially incoherent. As the object beam speckle pattern defocused, the interference signal (i.e. visibility) decreased. Coherent noise in the image was suppressed by averaging over many captured patterns.

The CCD camera used captured at a rate of 4 Hz in order to obtain quadrature images. The system demonstrated a full-field surface height precision of 1 nm RMS. The author noted future implementations of this arrangement could include using MLCs to improve performance (e.g. increased beat frequency) and the use of an optically generated reference signal to enable stable image capture.

2.2.5 Kimachi

The MLC presented by Ando and Kimachi was used to capture and demodulate widefield heterodyne interference fringe patterns [25]. As described in section 2.1.2.1, the 64×64 pixel camera was capable of outputting real-time phase images, operating at 30 fps, by acquiring the data at three phase points in a modulation period (three-phase correlation image sensor).

The reported interferometer described a combination of Mach-Zehnder and Michelson interferometers, similar to the arrangement described by Massie. A stabilised HeNe beam (λ = 632.8nm) entered the Mach-Zehnder interferometer, and two AOMs and a waveplate were used to generate frequency shifted (by 80 MHz and 80.025 MHz) orthogonally polarised arms. The two frequency separated beams

entered the Michelson interferometer and produced the interference pattern onto the camera device after reflecting off a reference mirror and object. A beamsplitter was used before the two beams enter the Michelson interferometer in order to capture a beat signal (beat frequency $f = 25\,\text{kHz}$) using a photodiode; this captured optical signal was used as the electronic local reference signal to demodulate the captured fringe pattern (the electronic signal was 3-way phase split by $2\pi/3$). This is similar to the ultrastable technique described in chapter 5, but the goal in this implementation was only to determine the beat signal (vibration in the Michelson interferometer would still produce an unstable pattern. The setup was used to obtain results of a scanning PZT mirror and of heated silicone oil, with a reported phase accuracy of 0.85°.

The improved 200×200 pixel correlation image camera was used for real-time capture of heterodyne speckle patterns [16]. Two interferometer arrangements were presented; a Michelson arrangement where beams reflected off a reference grating and an object grating before interference (figure 2.10(a)), and an in-plane interferometer where a split beam reflected off a single object grating at different angles, generating an interference pattern which was detected at a fixed distance from the grating(figure 2.10(b)). In both arrangements, an external signal generator provided the local reference for image demodulation, and was used to drive an electro-optic modulator (EOM). The light source from a 6 mW HeNe laser passed through the EOM, which produced a pair of orthogonally polarised beams (with a frequency separation of $f = 100\,\text{Hz}$), which entered the interferometer arrangements after passing through a polarising beamsplitter.

The system had a reduced frame rate of 8.33 fps due to limitations on the external circuitry (not of the camera itself); a demodulated phase standard deviation of 19° was reported.

2.3 Electronically stabilised heterodyne capture

The ability to detect changes in the optical path length of a beam within a sub-wavelength range (i.e. nanometers) is a major asset of using interferometry for a variety applications. However, this causes a problem in practical systems as changes in the ambient conditions (heat, vibration, air flow, etc) could cause

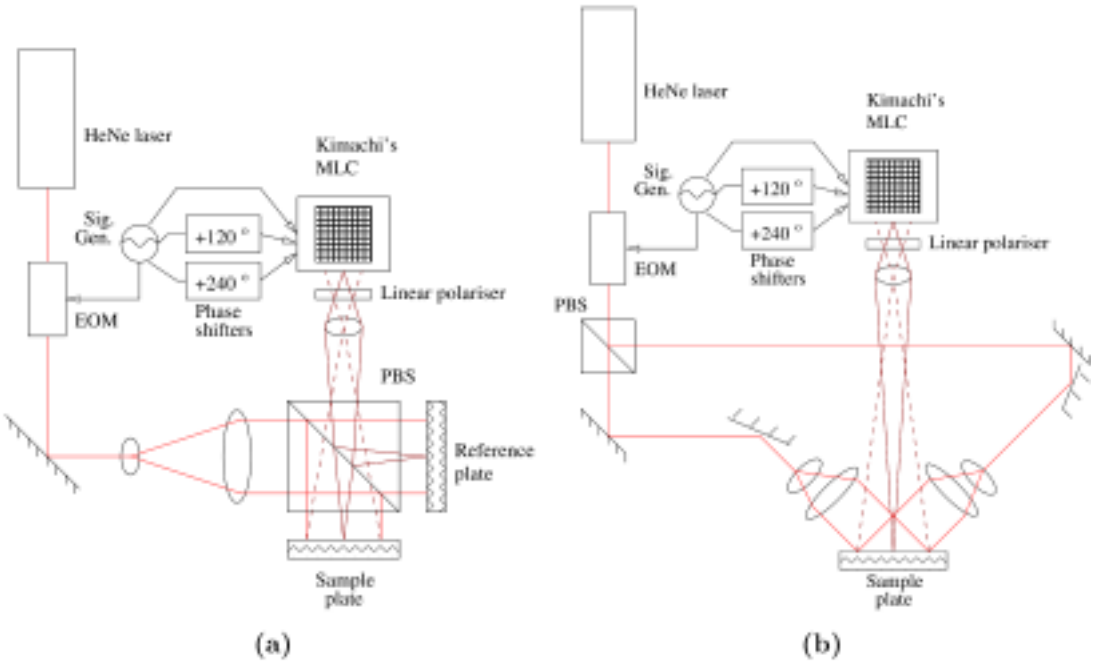

Figure 2.10: Two scattering heterodyne interferometer arrangements designed by Kimachi which used the 3-phase CIS camera (Kimachi 2010 [16]). A local reference signal was used in the electro-optic modulator (EOM) and for the camera's demodulation method (after phase splitting). Both arrangements used the EOM to generate two orthogonally polarised frequency shifted beams. The left (a) and right (b) arrangements are of a Michelson interferometer and in-plane interferometer respectively.

measurement instability (e.g. time varying phase shifts cause unstable phase images) that will greatly affect the accuracy of the system; the stability of a captured interferogram can be the critical factor for an interferometer system design.

An often used technique to counteract the effects from external influences involves using self-referencing, i.e. removing the unwanted temporally varying phase from an interferogram with some form of feedback. This involves acquiring a reference signal with the same unknown temporal phase variations as the testing beam or the generated fringe pattern (producing a relative phase image).

Optically, this can be achieved by using a common path (C-P) interferometer (described in section 1.5) where interference occurs between one part of a single beam with another part, i.e. a temporally delayed [91] or spatially shifted version of itself [92]. Therefore, the two interfering beams contain (most of) the same unknown temporally varying phase function.

In heterodyne interferometer systems, this can also be implemented electronically. Environmental variations will cause a shift in the observed modulation frequency (explored further in section 5.1.2.3). This signal can be used as the reference signal for the demodulation technique [85] (analogous to a phase-lock loop operations used in RF communication systems [33]). This section explores heterodyne interferometer systems that use this electronic stabilisation technique.

2.3.1 Massie

The real-time heterodyne interferometer system described by Massie was one of the first to implement an electronic feedback system to remove *'the corrupting motions'* of the interferometer optics [15, 85, 87]. The reference signal used in the zero crossing phase-meter was derived optically by measuring the beat signal at a fixed point in the fringe pattern using a photodiode. The author referred to this as a common path phase reference signal which records rigid body motions of the interferometer optics (in addition to controlling the phase offset) and noted that it would not be possible to measure the absolute phase using this setup. Due to the slight variations in the optical arrangement between the two capture points, the system's precision was limited by external noise sources (noted as air turbulence, component mechanical jitter, etc.) to $\lambda/1000$. A similar technique to this is used in the ultrastable interferometer explored in chapter 5, except the measurement of the beat signal is made on the camera array itself.

2.3.2 Toyooka

A heterodyne interferometer presented by Toyooka makes use of a cascading double-diffraction optical arrangement [93]. In this setup, a collimated beam from a HeNe laser ($\lambda = 633\,\text{nm}$) was passed through a moving grating (at a fixed velocity). This created different orders of diffraction; the grating functions as both a beam divider and frequency shifter. The scattered light entered the first spatial filter where at the focal plane, the light was spatially split into many components. The filter at this plane consisted of two holes allowing through the zeroth-order beam with a small hole, i.e. DC spatial frequency only, and first order beam with a large hole, i.e. extended spectrum passes, which became the

reference and frequency shifted test beams respectively. This created two diffraction components at the exit of the first spatial filter, so a second filter was used to select one to produce one interference pattern.

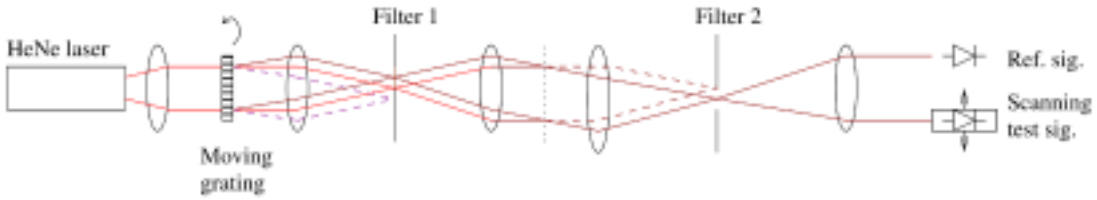

Figure 2.11: Toyooka's cascading double-diffraction interferometer (Toyooka et. al 1984 [93]). Light from a HeNe laser was spatially split and frequency shifted into multiple orders using a moving grating. The light entered a spatial filter where the spatial DC content and wideband content of two orders were allowed through. Two heterodyne interference patterns are generated, so a second filter was used to select one to pass through. A scanning photodetector was used to record the widefield image, whilst a fixed photodetector is used to determine a reference signal (to keep the measure pattern stable).

Similar to the system described by Massie, the resultant interference pattern was measured using photo-multipliers at two points, one at a fixed location (to acquire the beat signal) and another on a stepper motor mount to scan across the fringe pattern. Both signals are fed into a phase-detector, which would output a voltage depending on the time intervals between the zero-crossing times of the two electronic waveforms. The beat frequency of the system was equal to 100 Hz and a standard deviation in measured phase of $\lambda/130$ was reported.

2.3.3 Offside

A scanning optical profilometer presented by Offside produced two orthogonally polarised heterodyne interference patterns which utilised a common path arrangement [94]. The setup produced three beams in a modified Michelson interferometer, a sample reference beam, a sample probe beam and a common reference beam. Light from a laser was split using a beamsplitter, one arm passed through a Bragg cell twice and reflected back into the system as the common reference beam. The other arm passed through an optical construct made of an annular

waveplate and a lens with a hole. This created two beams that were orthogonally polarised; the wide area collimated beam was used as the sample reference beam and the focused beam was used as the sample probe. Both beams reflected back off a sample surface and back into the interferometer. All three beams passed through a polarising beamsplitter which splits the common reference beam and separated the sample reference and probe beams, generating two separate interferograms that were detected by photodiodes, much like the system described by Massie. A stable phase image was determined using a vector voltmeter using the two capture signals and a scanning system.

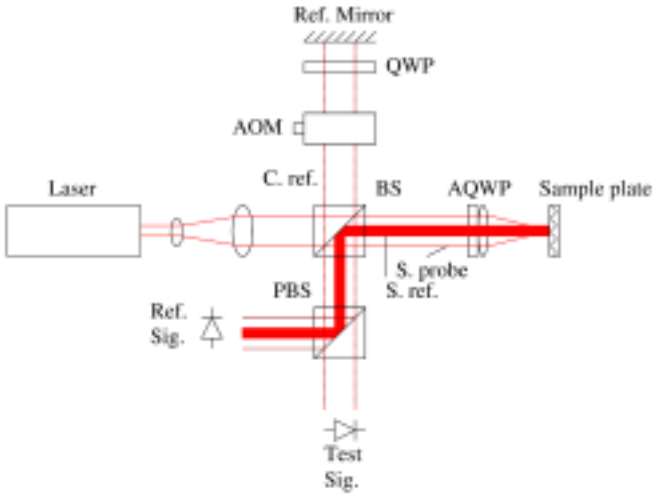

Figure 2.12: Offside's scanning optical profilometer (Offside et. al 1989 [94]). Light from a laser is split into two arms, sample and reference. The reference arm double passes through an AOM to introduce a frequency shift (C. ref.). The sample arm passes through an annular quarter wave plate with a hole, generating two beams, the sample probe and sample reference. Each of these beams interfere separately with the common reference, and each interference pattern is split (using the polarising beamsplitter) and detected using two separate photodetectors. The reference signal is used to maintain a stable interferogram.

The author demonstrated a comparison between the presented system and a basic Michelson interferometer which showed that under the same stability test (64 g ball dropped on the table from 30 cm) the RMS variation in the phase equalled 0.28 nm and 4.12 nm in the respective systems. It was also noted that drilling holes in lenses was practically challenging and other arrangements could be made possible using mirrors.

2.3.4 Chou

A heterodyne interferometer developed by Chou used a birefringent lens to produce a common-path polarised optical profilometer [95]. The optical arrangement used a modified combination Mach-Zehnder/Michelson interferometer. After light from a HeNe laser entered the Mach-Zehnder interferometer, two frequency shifted beams were produced using two AOMs driven at 80.0000 MHz and 80.0377 MHz (beat frequency f = 37.7 kHz). The object beam entered the Michelson arrangement, where the object arm consisted of a birefringence lens arrangement; the light in one polarisation plane had a different focal plane to the light in the orthogonal polarisation plane (f_e = 87.8485 mm for the extraordinary ray and f_o = 40.0735 mm for the ordinary ray). This property of the lens was exploited in order to create two sample beams, a reference and probe, similar to the arrangement presented by Offside. Once reflected off a test sample, the beams combine with the original Mach-Zehnder reference beam, and the three beams were split using a polarising beamsplitter. The interference patterns were captured using two photodetectors and stable phase measurements were made using a lock-in amplifier and a PC. Repetition in the surface profile measurement revealed a maximum variation of 0.5 nm.

2.3.5 Aguanno

An approach for heterodyne interference pattern capture described by Aguanno involved using a high read rate CMOS camera [96]. The optical arrangement in the setup was a Mach-Zehnder interferometer, with each arm frequency shifted by 80 MHz and 80 MHz+82.2 Hz (beat frequency f = 82.2Hz). The light source used was a Ti:Sapphire laser (λ = 532 nm). The interferogram was detected using a 512×512 CMOS camera (AKAtech iMVS-135) read by a 40 MS/s ADC/DSP. In order to construct a stable image, the system read one row at a time and used the first pixel in each row as the reference pixel (eliminating the temporally varying phase common in both captured signals). Each pixel was sampled at 1.3 kHz. The DSP unit was used to output phase using a quadrature mixing process (as described in section 1.3.6) using the captured sample and reference waveform. This generated a full-field phase image without mechanical scanning. The author noted that the pixel read rate was dependent on the light intensity incident on each pixel as averaging was required over time. With 40 mW m^{-2} incident, the

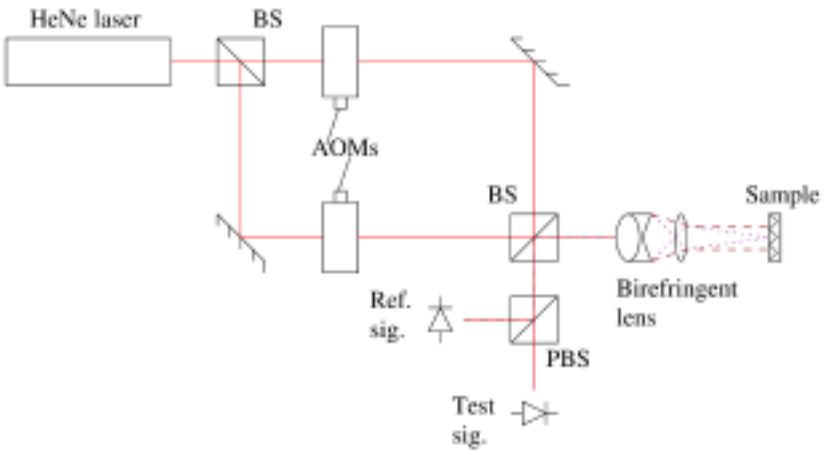

Figure 2.13: Chou's optical profilometer (Chou. et al 1998 [95]). The light from a HeNe laser was split. Each arm was frequency shifted using AOMs and passed through a second beamsplitter. One arm passed through to a birefringent lens, where light with different polarisation planes focused to different points away from the lens. These two new beams now become the sample probe and reference, analogous to the interferometer described by Offside. These two beams recombined with the other original beam, generating two interference patterns, which were split using a polarising beamsplitter and detected using photodetectors.

read time was equal to ~4 ms, however, increasing the intensity to 400 mW m^{-2}, reduced pixel the read time to 400 μs. A phase error of 0.004° was reported.

2.3.6 Park

A heterodyne interferometer scheme developed by Park used a double pass through a single AOM in order to generate a reference and sample fringe pattern [97]. In this arrangement, light from a single mode stabilised HeNe laser was passed through a polarising beamsplitter (only one of the split paths was used at this stage). An AOM, driven at 40 MHz, was tilted at an angle to satisfy the Bragg condition with respect to the angle of light incidence. Two beams were present at the output; one travelled along the same path as the incident light with no frequency shift, referred to as FO, and the other beam appeared deflected (with respect to the incident beam path) and was frequency shifted, referred to as ZO. Both beams passed through a waveplate and were reflected along the same path using mirrors. When each beam passed through the AOM again, they were each split into two. Due to each beams path, they both experience different frequency

shifts; the diffracted versions of FO and ZO experienced an upshift and downshift in frequency respectively. Therefore, on the second pass through the AOM, the FO splits into the original FO (or ZFO) and +FO (or FFO) and the ZO was split into the original ZO (or ZZO) and -FO (or -FZO). Once all four beams passed thorough the polarising beamsplitter, the ZZO and FFO beams interfered along one trajectory and the -FZO and ZFO beams interfere along another trajectory. Due to the double pass through the AOM, both interference patterns had the same beat frequency, and since both beams travelled along similar paths, the optical signal they carried include the same common temporally varying phase (e.g. due to vibration). The fringe patterns were detected using a pair of photodiodes and a differential amplifier was used to electronically determine the difference between each signal. Demodulation was conducted using quadrature demodulation through mixing. The author claimed a displacement resolution of $\sim$0.5 nm.

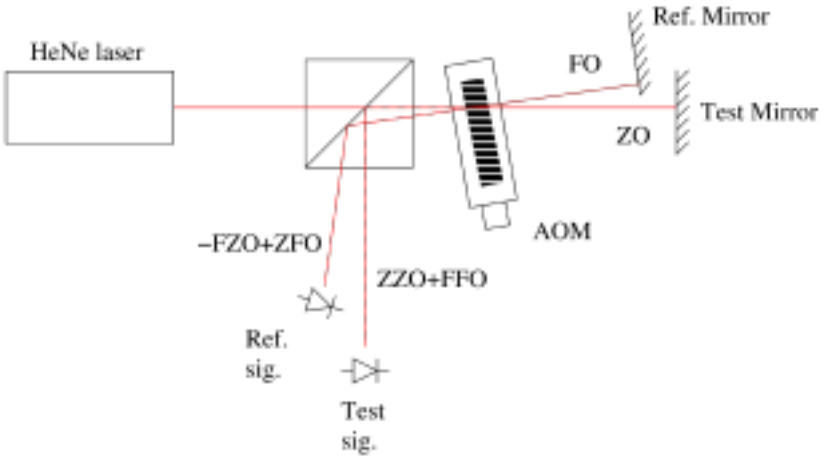

Figure 2.14: Park's AOM double pass heterodyne interferometer (Park and Cho 2011 [97]). Light from a HeNe laser passed through an AOM where light was split into a frequency shifted order (FO) and non-frequency shifted order (ZO). After both beams were reflected back into the AOM, each beam generated additional orders (FO $\rightarrow$ ZFO and FFO, ZO $\rightarrow$ ZZO and -FZO). Owing to their trajectory, [-FZO and ZFO] and [ZZO and FFO] interfered; the modulation frequency in each pattern was equal (double the AOM drive frequency). One pattern is used for the reference beat signal and the other was used to capture a stable interferogram.

2.4 Two separate source interferometer systems

A common misconception in the field of interferometry is that light from different sources do not produce observable interference patterns. Dirac claimed in his quantum mechanics book in 1930 that "*each photon then interferes only with itself. Interference between different photons never occurs.*" [98]. It was viewed that interference patterns generated by a light stream would only interfere on account of its own wave function and not with another stream's function.

In basic interferometer systems, for interference patterns to be detectable, the interfering light beams are required to have a constant or, at least, a definable phase relationship between each other [12]. It was thought that the relationship was only maintainable when interfering split light from the same source. The visibility of the interference pattern would depend on the coherence properties of the source (discussed in section 1.4).

However, the visibility due the coherence of the source is a time averaged value, which is the case if an image is captured over time (large integration time or averaged) at one frequency (DC or a single heterodyne frequency). If the capture time is lowered sufficiently or if the pattern is allowed to be captured over a large operational bandwidth, it is possible to capture the interference pattern from sources considered incoherent [99]. The instantaneous beat frequencies of two sources interfering (discussed in Appendix B) can vary randomly; a large variation in beat frequencies requires an extremely high operational bandwidth system or a high speed acquisition system. Therefore, a light source is required to keep the beat frequency to within a workable range. For example, in a laser implementation, a frequency locking method could be used between the separate sources in order to maintain a phase relationship between the sources (to ensure that the beat is within the parameters of the detection unit [100]). This section describes interferometer systems that have been used to capture the widefield interference patterns generated by two lasers.

2.4.1 Magyar and Mandel

Two laser interferometry was first performed by Magyar and Mandel [101]. The experiment used short pulses of light from two ruby lasers (referred to as '*opti-*

cal masers') with the interference captured on the photocathode of an electronic gated image tube. Using a mode-locking technique, short timed pulses from each laser (wavelength $\lambda = 694.3\,\text{nm}$) had a constant phase relationship over a short observation time, noted as being less than the reciprocal total frequency spread ($1/\Delta\lambda$) between the two lasers. Within this time, fringe patterns could be viewed as being static and could therefore be imaged. Even with the lock-in technique used, the system was limited by the exposure time of the detection unit (40 ns). When an image had been taken, the author noted a fringe visibility of 15 %. Additionally, provisions had to be made for preventing multiple exposures by paralysing the electronic gate for upto a millisecond after image capture.

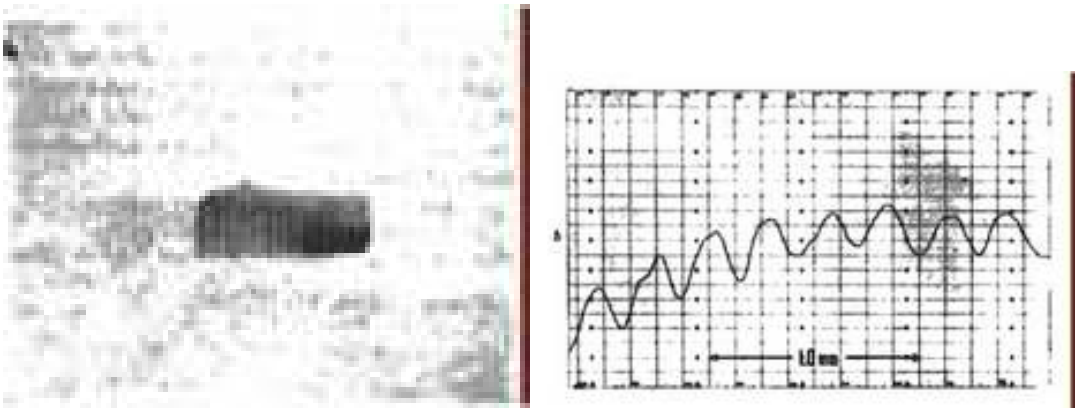

(a) **(b)**

Figure 2.15: Experimental images captured by Magyer and Mandel of two lasers interfering (Mandel and Magyar 1962 [101]). The left (a) image is the photograph taken of the fringe pattern generated and the right (b) is the intensity plot across the fringe pattern measured using a microphotometer tracing.

2.4.2 Louradour

A two laser interferometer presented by Louradour [102] improved on the setup used by Mandel and Magyar, in which the interference fringes lacked stability due to the thermal fluctuations of the source (which caused variations in the emission frequency). The system described by Louradour used a Nd:YAG laser to simultaneously pump two dye lasers. The emission frequency of the dye lasers depended on the temperature of the dye solution (i.e. tunable wavelength set to $\lambda \approx 568\,\text{nm}$), therefore, frequency stability (and adjustment) was maintained

through thermal regulation between the laser dye solutions; a maximum temperature difference of 0.1 °C was maintained for 30 mins.

The Nd:YAG pump laser was used to trigger emission pulses in the dye lasers where each pulse width, 20 ps, was less than to the coherence time of the dye lasers (the spectral bandwidth of the dye laser $\Delta f \approx 30$ GHz). A picosecond streak camera was used to capture the two lasers' interference pulse patterns. The author noted that upto 100% fringe contrast was achievable, but fringe positions shifted shot by shot.

2.4.3 Basano

An interferometer system described by Basano captured the fringe patterns generated using two stabilised laser diodes [100]. The light from the lasers were combined using a beamsplitter and interference fringes were generated by propagating each beam through a dual slit arrangement. The fringe pattern was recorded using a linear array of CCD pixels and was displayed using an oscilloscope.

In this implementation, the individual linewidths of the two single mode lasers (30 mW laser diode, $\lambda = 780$ nm) were narrower than 1 kHz. The average frequency drift rates for the stabilised lasers was noted as being less than 0.1 MHz/s. The experiment measured the correlation between the visibility of interference fringes and the integration time used for each CCD element. The results showed a loss in fringe contrast as the integration time was increased. Fringe patterns were visible for up to 1 ms.

2.4.4 Kawalec

A system developed by Kawalec allowed for naked eye observations of the interference patterns (i.e. long term stable DC fringes), generated using two lasers [103]. The emitted wavelength of each laser diode ($I < 300$ mW, $370\text{ nm} < \lambda < 1770$ nm) was varied by applying different currents to the laser input. One laser (labelled L2) had an emission frequency 200 MHz higher than the other laser (labelled L1). The system was implemented in two stages. In the first stage, light from each

laser was sent through a beamsplitter and the generated interference/beat signal was detected using a fast photodiode. The 200 MHz (difference frequency) signal was fed to a phase-lock loop and used to modulate the current input of the laser L2 in order to maintain the 200 MHz frequency difference between lasers L1 and L2. In the second stage of the system, an AOM was used to shift the frequency of laser L1 (using a double pass arrangement) by 200 MHz using the beat signal measured in the first stage. This ensured that, in this second stage, the instantaneous frequency of both lasers were the same.

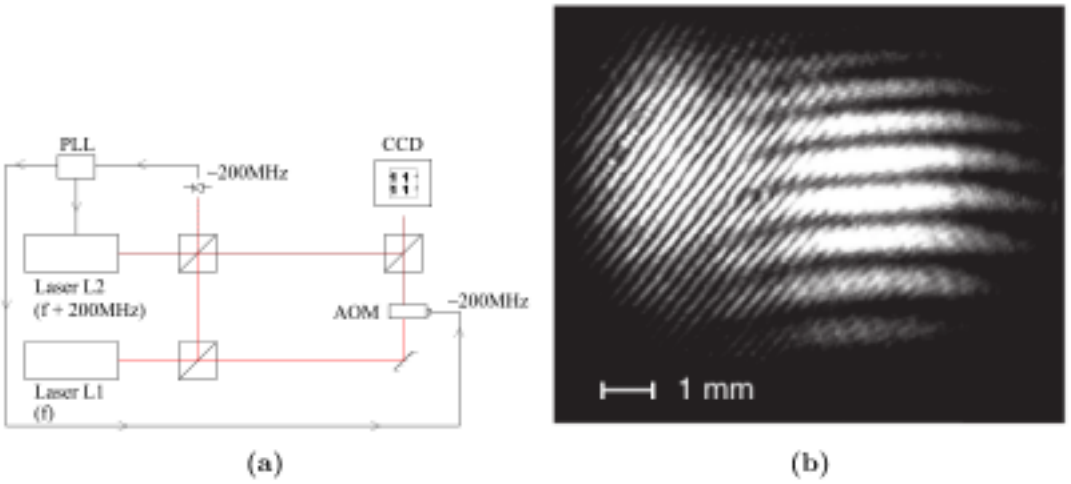

Figure 2.16: Kawalec's two laser interferometer (Kawalec and Bartoszek-Bober 2012 [103]). (left) Light from L2 was set to have a central emission frequency at 200 MHz higher than L1. The beat signal produced when they interfere was measured using a photodiode and used to 'stabilise' L2's emission frequency. The same signal was used to frequency shift light from L1 at another stage of the interferometer, where this light was interfered with L2 to generate DC fringe patterns (right).

The generated interference pattern (visible to the naked eye) was captured using a commercially available CCD camera. The author demonstrated the system's ability to overcome the fast random changes in the laser emission frequencies by integrating a fringe pattern for 5 s.

Chapter 3

MLC and system methods

In this chapter, the modulated light camera (MLC) utilised to capture interference fringe patterns presented in this thesis is analysed. A brief overview of the camera is given, along with an examination of the circuitry in each pixel and a discussion of the output uncertainty. This chapter also discusses the components used in the interferometer systems, including acousto-optic frequency shifters and lasers, as well as the data acquisition process for the MLC output. Considerations during the capture process are also discussed.

3.1 Modulated light camera

3.1.1 Camera brief

One of the major themes of this thesis was to capture heterodyne interference fringe patterns using a modulated light camera (MLC). The modulated light camera used for this project is the next iteration of the MLCv6 camera design (discussed in section 2.1.3.6).

Like its predecessors, each pixel on the camera produces a continuous electronic signal of the detected optical signal, which is continuously demodulated through analogue mixing using local reference signals (as long as the pixel has been selected [55,84]). Updates to the camera design from MLCv6 include the correction of an on-chip read error, component rearrangement to reduce electronic noise (specifically the crosstalk from the RFout), improvements to the fill-factor, and an increase to the power supply and RF signal distribution lines.

The camera features a 32×32 CMOS pixel array; the pixels have a pitch (i.e. distance between pixel centres) of 115 μm, each with a fill factor (i.e. photosensitive area of each pixel) of 16 % (area of 2.116 nm^2). The total size (including addressing/buffer/other external circuitry) of the camera is 3.68 mm × 3.68 mm. Each pixel electronically demodulates the detected optical signal through continuous quadrature mixing (mixed with an external reference signal) to produce differential in-phase ($I^+_{\text{out}}/I^-_{\text{out}}$) and quadrature phase ($Q^+_{\text{out}}/Q^-_{\text{out}}$) outputs. DC intensity outputs are also available for each pixel. The CMOS chip architecture allows for random access to any pixel, which is setup set up in 8 banks of 4 columns. The combination of continuous demodulation and random access pixels means that any pixel's phase data can be read immediately after being addressed. Additionally, four pixels in the centre of the camera have been designed to directly output the raw detected modulated signal (RFout).

Specifying the operation bandwidth figure of the camera can be complex as it is dependent on a number of factors. Most notably, the bandwidth is largely dependent on the DC and AC content of the incident light (discussed further by the chip designer [55]). The amplifier stage of the camera can be tuned to provide maximum gain by sacrificing bandwidth; a gain of 32 dB → 38 dB for a bandwidth of 100 kHz to 40 MHz → 17 MHz. Hence, a 'conservative' bandwidth figure for the MLC of 100 kHz to 17 MHz has been determined. Optical signals with modulation frequencies of up to 50 MHz have been successfully measured using high values of DC intensity (100s nanowatts per pixel) and data averaging [55].

3.1.2 Analogue demodulation process

As briefly discussed in section 1.3.6, quadrature demodulation of an incident signal can be performed through analogue mixing. The advantages of using analogue mixing for heterodyne signal demodulation over other methods include being able to determine phase continuously (as opposed to signal sampling or integrating bucket methods) and retaining the maximum signal for the phase output (i.e. square wave mixing).

Each pixel on the camera captures the local incident modulated light. As discussed in section 1.2.3 and section 1.6.2, the photocurrent generated by the photosensitive material is proportional to the light intensity incident on it.

In an ideal detection unit, this photocurrent is passed through a linear load. The voltage observed across the load, V_{in}, would be proportional to the incident intensity, such that;

$$V_{\text{in}} = V_{\text{DC}} + V_{\text{AC}} \cos(\omega t + \phi) \tag{3.1}$$

where V_{DC} and V_{AC} is the component in the voltage signal due to the DC intensity and the AC amplitude of the incident optical signal respectively, ω is the angular modulation frequency, and ϕ is the phase offset of the incident modulated light.

External reference in-phase, I_{LO}, and quadrature phase, Q_{LO}, signals are mixed with the detected signal;

$$\begin{aligned} I_{\text{LO}} &= V_{\text{LODC}} + V_{\text{LOAC}} \cos(\omega t) = V_{\text{LODC}} + V_{\text{LOAC}} \cos(\omega t - 0^\circ) \\ Q_{\text{LO}} &= V_{\text{LODC}} + V_{\text{LOAC}} \sin(\omega t) = V_{\text{LODC}} + V_{\text{LOAC}} \cos(\omega t - 90^\circ) \end{aligned} \tag{3.2}$$

where V_{LODC} and V_{LOAC} are the DC offsets and AC amplitudes of the local reference signals respectively. The reference signals have the same frequency as the incident optical signal.

Mixing two signals involves multiplying them together; multiplying two sinusoidal signals produces a sum-and-difference output. For each of the reference signals mixed with the detected signal, the output can be expressed as;

$$\begin{aligned} I_{\text{mix}} &= V_{\text{in}} I_{\text{LO}} \\ &= V_{\text{DC}} V_{\text{LODC}} + V_{\text{DC}} V_{\text{LOAC}} \cos(\omega t) + V_{\text{LODC}} V_{\text{AC}} \cos(\omega t) \\ &\quad + \frac{V_{\text{AC}} V_{\text{LOAC}}}{2} [\cos(2\omega t + \phi)] + \frac{V_{\text{AC}} V_{\text{LOAC}}}{2} [\cos(\phi)] \\ Q_{\text{mix}} &= V_{\text{in}} Q_{\text{LO}} \\ &= V_{\text{DC}} V_{\text{LODC}} + V_{\text{DC}} V_{\text{LOAC}} \sin(\omega t) + V_{\text{LODC}} V_{\text{AC}} \cos(\omega t) \\ &\quad + \frac{V_{\text{AC}} V_{\text{LOAC}}}{2} [\sin(2\omega t + \phi)] + \frac{V_{\text{AC}} V_{\text{LOAC}}}{2} [\sin(\phi)] \end{aligned} \tag{3.3}$$

where I_{mix} and Q_{mix} is the resultant signal from mixing the detected signal (V_{in}) with the in-phase (I_{LO}) and quadrature phase (Q_{LO}) reference signals respectively. Given that the frequencies of both mixed signals are the same (ω), the temporally

varying components in the 'difference' term are cancelled out (i.e. down-mixed to DC), leaving only the phase element.

Applying an ideal low pass filter to these signals eliminates all but the DC components, such that the in-phase (I_{out}) and quadrature phase (Q_{out}) outputs can be expressed;

$$\begin{aligned} I_{\text{out}} &= V_{\text{DC}}V_{\text{LODC}} + \frac{V_{\text{AC}}V_{\text{LOAC}}}{2}\cos(\phi) \\ Q_{\text{out}} &= V_{\text{DC}}V_{\text{LODC}} + \frac{V_{\text{AC}}V_{\text{LOAC}}}{2}\sin(\phi) \end{aligned} \tag{3.4}$$

The process of extracting the phase requires the removal of the DC offset and AC amplitude components. For this, the differential in-phase ($I^{+}_{\text{out}}/I^{-}_{\text{out}}$) and quadrature phase ($Q^{+}_{\text{out}}/Q^{-}_{\text{out}}$) outputs are determined. The phase of the signal detected at each pixel can be extracted by using;

$$\phi = \arctan\left(\frac{Q^{+}_{\text{out}} - Q^{-}_{\text{out}}}{I^{+}_{\text{out}} - I^{-}_{\text{out}}}\right) \tag{3.5}$$

The `atan2` operation (available in the majority of mathematics based programming environments) is preferred over using `atan` as it is capable of distinguishing direction and can output angles over the full 2π range.

In a practical system (i.e. this MLC), the accuracy of the output phase is based on a number of factors; the linearity of the frontend, the phase and amplitude differences between the reference signals, the output filter response, and quantisation error in the analogue to digital conversion [33], in addition to the noise in the signal from electronic and optical sources (section 1.7).

3.1.3 Pixel overview

Each pixel on the MLC is fabricated using the same electronic footprint. A schematic of the components that form a signal MLC pixel is illustrated in figure 3.1.

The modulated light that is incident on each pixel is detected using the photodiode element (taking 16 % of the pixel's area). A continuous photocurrent signal (i_{PD}) is generated if the frequency of the modulated signal is less than the

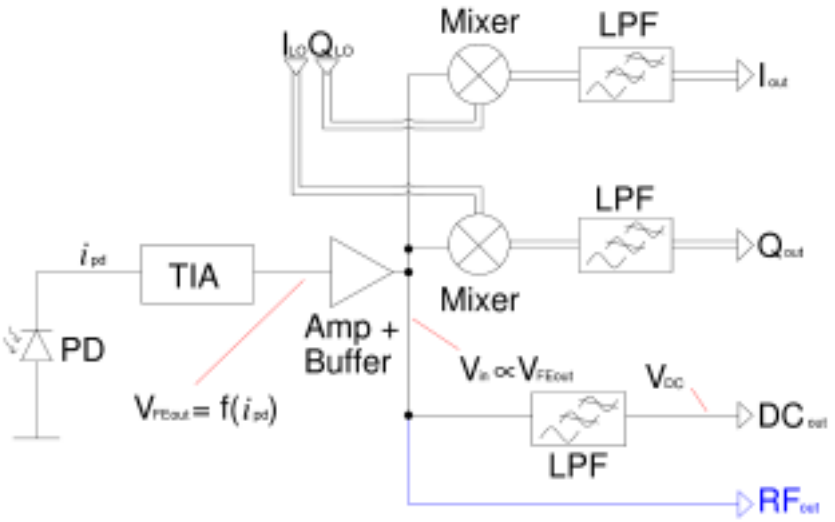

Figure 3.1: Schematic of a single pixel. The diagram shows the different stages of each pixel; the photodiode and transimpedance amplifier (TIA) produce a frontend voltage that has a logarithmic relationship with the photocurrent. This signal is amplified where it is, low pass filtered for a DC output, fed out directly in the RFout pixels, and fed to two analogue mixers. The signal is mixed with LO signals (with the same frequency as the modulated signal), producing differential I and Q values (at 0 Hz), and is filtered before being output.

frequency response cutoff of the photodiode (simulation results indicate this to be ~70MHz [55]). In the pixel frontend, a current-to-voltage conversion is conducted using a transistor-diode arrangement (transimpedance amplifier). This provides a voltage, V_{FEout}, that has a logarithmic relationship with the generated photocurrent; this is discussed further in section 3.1.3.1.

The frontend voltage signal is amplified (V_{in}) using an operational amplifier and a unity gain inter-stage buffer. In the setup used for the images captured in this thesis, the amplifier stage has been set to provide an operating frequency range (-3 dB cutoff) of between 100 kHz and 17 MHz.

At this stage, each pixel outputs (when addressed) the low frequency component of the incident signal (V_{DC}) as it is passes through a variable low pass filter (1 kHz - 5 kHz, set to 2 kHz).

Four pixels in the centre of the camera array (pixels [x=15 y=17], [x=16 y=15], [x=17 y=18], [x=18 y=16], shown in figure 5.1) are designed with additional RF

output lines (RF_{out}), which output the amplified detected signal (i.e. V_{in}). This output is constantly 'on' and requires no specific pixel addressing. When designing the MLC, the choice of designating which pixels should be RFout pixels was determined by assuming that the maximum optical intensity would be incident at the centre of the array. Simulations showed that these RFout pixels produced more electronic crosstalk than regular MLC pixels [55], so the number of these pixels was limited to four, with none of the pixels sharing the same row or column.

The amplified detected signal (V_{in}) is mixed with external reference signals (I_{LO} and Q_{LO}) using two fully differential Gilbert cell mixers. The operation of the mixer stage is discussed further in section 3.1.3.2.

The two differential outputs from the Gilbert cells are low pass filtered, with the filter -3 dB cutoff set to 2 kHz. The four outputs ($I^{+}_{\text{out}}/I^{-}_{\text{out}}$ and $Q^{+}_{\text{out}}/Q^{-}_{\text{out}}$) are available on the MLC's output pins when the pixel is addressed (described further in section 3.2.3).

3.1.3.1 Logarithmic frontend

As each pixel contains a small photosensitive area, it generates a small photocurrent when light is incident. To enable a pixel read, a current-voltage gain method is required (ref. section 1.6.3). As the MLC was intended to be a continuous time camera, a gain method that involves charge collection over time (e.g. using signal bins) cannot be used. Instead, the time varying photocurrent generated by the photodiode, i_{pd}, in each pixel is converted to a voltage with a function, such that $V_{\text{FEout}} = f(i_{\text{pd}})$. The frontend circuit in the MLC provides a logarithmic current-voltage conversion relationship; an example plot of the frontend voltage response is illustrated in figure 3.2.

One of the requirements of the detection unit for the demodulation process described in section 3.1.2 is to provide a linear relationship between the voltage and photocurrent. It is possible to work within a photocurrent range (and hence intensity range), where $f(i_{\text{pd}})$ appears linear. Referring to the frontend response plot (figure 3.2), this 'linear' range is indicated as the shaded orange region. The incident light is required to have a high intensity (high DC offset) but with a low variation/modulation depth (small AC amplitude) to stay within the 'linear'

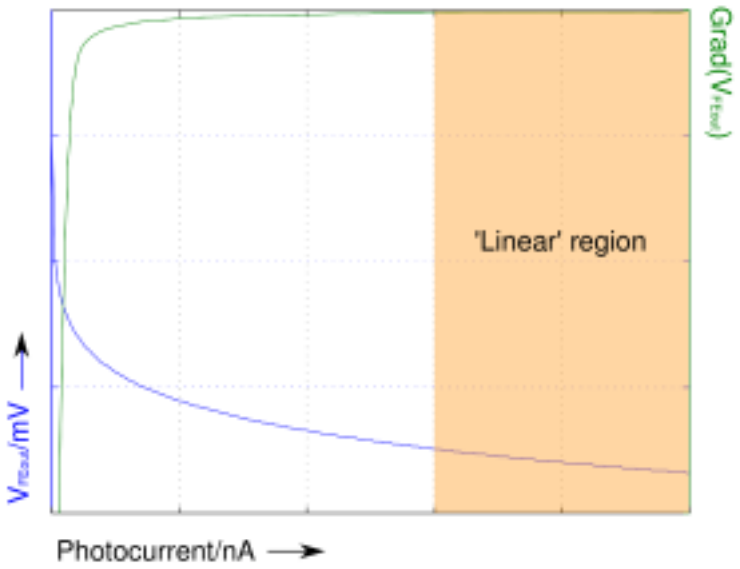

Figure 3.2: Graph showing the (blue) voltage output observable at the frontend (V_{FEout}) vs. the photocurrent generated by the pixel photodiode. The gradient of the voltage, with respect to the photocurrent, is shown as the green trace. The shaded area on the graph indicates the local region where the gradient is approximately flat, and where the frontend response appears linear.

range.

As an improvement on the design of the MLCv5 frontend [84], the frontend circuit of this MLC also includes a biasing transistor. The bias transistor acts as a current sink for the reverse bias photodiode and logarithmic load transistor circuit (section 1.6.3.3). This allows the user to tune to a bias point on the frontend response curve, effectively simulating an additional amount of incident DC light onto each pixel. This 'tune biasing' function is not used in the interferometer systems presented in this thesis, but is used by the chip designer to test the camera at different points on frontend response curve [55].

The voltage at the frontend output given the photocurrent, also known as the transimpedance gain or the frontend load, is regulated using a current feedback circuit. Figure 3.3 illustrates the results of a design simulation [55] for the operational frequency against the transimpedance gain for varying values of photocurrent. In effect, this is the AC amplitude frontend response, assuming it is small (in this simulation, the AC amplitude is 1 nA). The response diminishes as

the frequency increases, but also has a lower frequency cutoff for lower values of photocurrent (in exchange for the gain required).

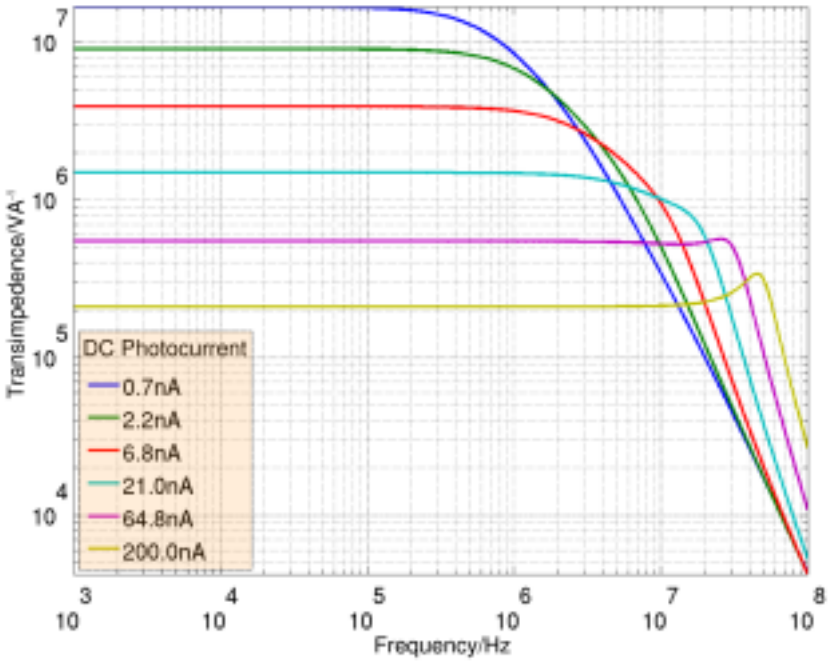

Figure 3.3: Graph of the simulated transimpedance gain of a small AC signal (1nA) at various frequencies [55]. A number of plots are given for differing values of DC photocurrent. As the amount of DC photocurrent increases, the current-voltage conversion value decreases. This remains almost constant upto an AC 'cut-off' frequency.

In addition to the amplitude response, frontend simulations were conducted to determine the noise equivalent bandwidth (NEB) [55]. Figure 3.4 illustrates the noise response in $V/\sqrt{Hz}$ with varying AC frequencies at different values of DC photocurrent.

The noise response graph can be used to determine the RMS noise at a given frequency over a specific bandwidth, and indicates the minimal detectable AC signal (unity SNR). As an example, assuming that the photocurrent generated due to the DC component of an incident modulated optical signal is 200 nA (light intensity of 600 nW) and measurement bandwidth of 2 kHz, $V_{rmsnoise} = 98.3\,pV$. Using the transimpedance plot in figure 3.2, this equates to a RMS noise current of $i_{rmsnoise} = 0.5\,fA$ (equivalent to a light intensity of 1.5 fW, 478 photons at $\lambda = 633\,nm$). The AC component of the example optical signal will need to be larger than this value.

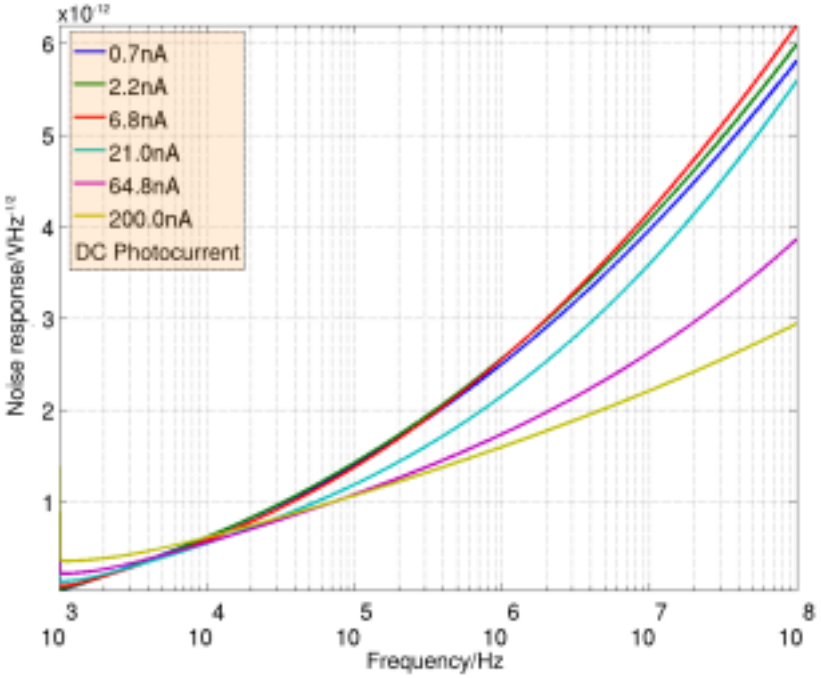

Figure 3.4: Graph of the simulated noise response (as an RMS voltage) at different operational frequencies [55]. Plots for different values of DC photocurrent is presented.

3.1.3.2 Mixer stage

Analogue multiplication of two signals can be achieved by using a non-linear device (where the output has a function consisting of a polynomial equation). With two signals input into a device, the second order output is of interest as one of its components is the multiplication of the two input signals. For example, if two signals, v_{i1} and v_{i2}, are fed into a diode (forward bias, small signal), the output signal would be proportional to $v_0 = (v_{i1} + v_{i2}) + \frac{1}{2}(v_{i1} + v_{i2})^2 + \ldots$. The second order output can be expressed as $(v_{i1} + v_{i2})^2 = v_{i1}^2 + v_{i2}^2 + 2v_{i1}v_{i2}$ which contains the multiplication of the two input signals [1, 33, 104].

A diode used in this way can be characterised as an unbalanced mixer. This type of mixer is simple in its design and can achieve a broad bandwidth, however since the output contains many components, sharp filters may be required to isolate the desired output (which may also be required to prevent the saturation of any output electronics). In addition, the input signals are required to be directly connected together, which could increase the circuit design complexity

(e.g. impedance matching). Instead of a diode, a transistor could be used. The signals are fed into the transistor source and gate, producing a mixed output (a source signal controlled using a gate signal with a non-linear response). This provides a degree of input signal isolation at a cost of bandwidth.

An alternative mixer circuit design is the balanced mixer; these mixers are designed to cancel out the unneeded first order components in the output signal, as well as providing isolation between the input signals. This class of mixer can be categorised into single balanced mixers or double balanced mixers, where either one of, or both input signals (i.e. first order components) are eliminated from the output equation respectively.

The mixer stage of the MLC has been designed using two Gilbert cell mixers [105], which are classed as a form of double balanced mixers. The Gilbert cell produces differential outputs using differential input signals. A simplified circuit diagram is illustrated in figure 3.5. The mixing process in the cell is performed by the four transistors in the centre. The signal at locations a, b, c and d will be proportional to the mix of signals [RF^+ and LO^+], [RF^+ and LO^-], [RF^- and LO^-] and [RF^- and LO^+]. Considering the first and second order components of each signal, adding the signal at a and c will eliminate all but the multiplication term (RF^+LO^+) at Out^+ (the same is true for Out^-). Each pixel contains two Gilbert cells for mixing the detected signal with either the in-phase or the quadrature local oscillator signal.

3.1.3.3 Estimated uncertainty

As discussed in section 1.7, a signal in a real system becomes 'contaminated' as each stage within the system adds noise onto the signal. Noise on an output signal introduces measurement uncertainties. Sources of uncertainty in the system can either be systematic or random. If systematic uncertainty is present in the system, repeat measurements of an unchanging variable will produce a static error onto the result. The system can be calibrated in order to remove this error (it will not be considered in this section). If there are random errors present in a system, repeat measurements of an unchanging variable will produce randomly different result. The spread of the random results can be described by using probability distributions, such as a Gaussian distribution or uniform distribution; the error

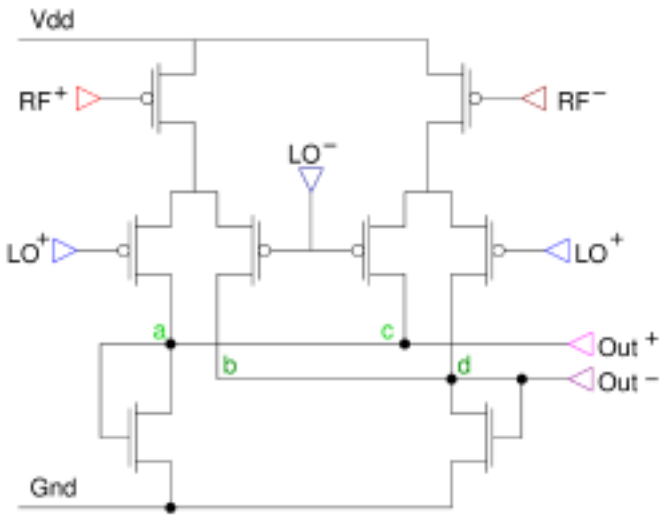

Figure 3.5: Schematic of a Gilbert Cell [105]. The four centre transistors form a ring; the two differential RF signals each mix with the two differential LO signals, producing four output signals. The addition of the signals at a and c, and b and d produce the differential output with first order suppression.

on the measured value is often given as the standard deviation.

The noise contributions from components along the system chain are assumed to be independent of each other as there is no correlation between the noise sources. The noise powers through a system are additive and are assumed not to be correlated, the noise voltages (or currents) can be calculated by summing the individual noise contributions in quadrature. This can be extended when considering multiple signals by using;

$$\Delta f = \sqrt{\sum_{i=n}^{n} \left(\frac{\delta f}{\delta x_i} \Delta x_i \right)^2} \tag{3.6}$$

Figure 3.6 shows the MLC signal chain (different electronic stages of each pixel); the noise and signal is annotated between the amplifiers and the mixer.

At the mixer stage, each phase output is generated by using two signals; the measured signal and the local oscillator signal. Using the uncorrelated noise assumption, it is possible to model the uncertainty at the output of the mixer, $\Delta \mathrm{Mix}_{\mathrm{out}}$, using equation 3.6, such that;

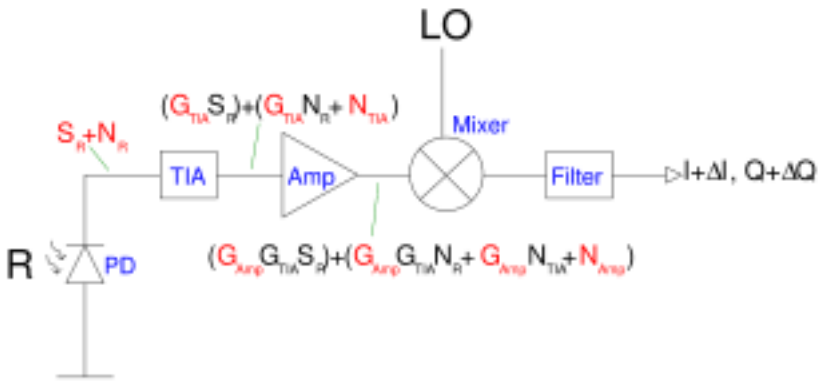

Figure 3.6: A diagram of the signal chain for the MLC. Both the signal and noise from the receiver is amplified. The amplifier components contribute its own noise to the signal chain.

$$\begin{aligned} \mathrm{Mix_{out}} &= \mathrm{Sig.LO} \\ \Delta\mathrm{Mix_{out}} &= \left(\left(\frac{\delta\mathrm{Mix_{out}}}{\delta\mathrm{Sig}}\Delta\mathrm{Sig}\right)^2 + \left(\frac{\delta\mathrm{Mix_{out}}}{\delta\mathrm{LO}}\Delta\mathrm{LO}\right)^2\right)^{\frac{1}{2}} \\ &= \sqrt{\mathrm{LO}^2.\Delta\mathrm{Sig}^2 + \mathrm{Sig}^2.\Delta\mathrm{LO}^2} \end{aligned} \tag{3.7}$$

where the measured signal and local oscillator signal at the mixer is expressed as Sig and LO, with the uncertainty of these signals expressed as ΔSig and ΔI_{LO} respectively.

In the standard widefield interferometer setup, the LO signal is derived from a signal generator. For the analysis described in this section, the assumption is made that there is no uncertainty in the LO signal (ΔLO = 0). The mixer is designed to produce unity gain and assumed to contribute negligible noise. The schematic in figure 3.7 shows how the noise around the modulation frequency (F_{mod}) appears at the output. The noise and signal from the mixer output is filtered using a 2 kHz low pass filter, as represented in figure 3.7(c). This is the equivalent of applying a sharp band pass filter around the high F_{mod} frequency signal, as illustrated in figure 3.7(d).

The phase (ϕ) of an incident optical signal is calculated by capturing the in-phase (V_I) and quadrature phase (V_Q) voltages at the output of the MLC. This is represented in the complex plane graph illustrated in figure 3.8. Repeat measurements of the voltage (given a constant input phase) will produce random results due to noise. In this analysis, the spread of the repeat results can be expressed as the

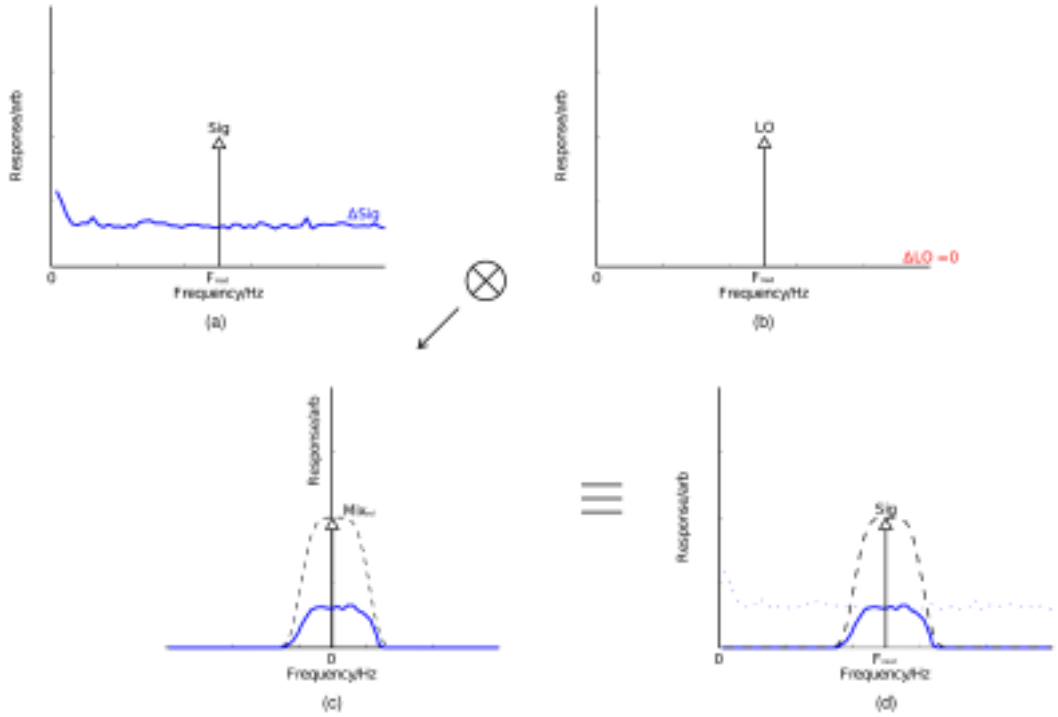

Figure 3.7: Schematic of frequency spectra depicting the inputs and output of the MLC mixer stage. The measured signal input (a) contains some random noise, whilst an assumption is made that the LO signal input (b) contains no noise. The output of the mixer (c) will be a down-mixed version of the measured signal (entire spectrum is mixed with the LO signal). This signal is filtered around DC using a low pass filter, which is the equivalent to band pass filtering the signal input (d).

RMS voltage around an offset (depicted as red dots around the 'true' value in figure 3.8) for both the in-phase (ΔV_{Irms}) and quadrature phase (ΔV_{Qrms}) signals. Given the condition that the signal to noise ratio of the output is greater than one, the uncertainty of the output phase ($\pm\Delta\phi$) can be calculated (using Pythagoras's theorem and trigonometry), using;

$$\begin{aligned} s &= \frac{1}{2}\sqrt{{\Delta V_{\text{Irms}}}^2 + {\Delta V_{\text{Qrms}}}^2} \\ \Delta\phi &= \arctan\left(\frac{s}{\text{amplitude}}\right) = \arctan\left(\frac{\sqrt{{\Delta V_{\text{Irms}}}^2 + {\Delta V_{\text{Qrms}}}^2}}{2.\text{amplitude}}\right) \end{aligned} \tag{3.8}$$

The error in phase can be further simplified by using the small angle approximation where $\tan\theta \approx \sin\theta \approx \theta$.

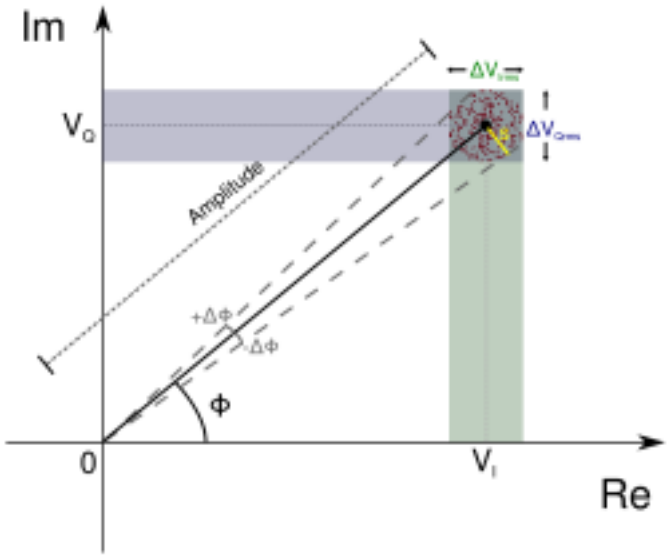

Figure 3.8: Argand diagram showing the relation between the MLC V_I/V_Q outputs and the signal phase, ϕ. With noise present on the MLC outputs, the captured voltage (given an incident signal with static phase) varies randomly (red dots) over the range, $\Delta V_{\text{Irms}}/\Delta V_{\text{Qrms}}$, shown as the green and blue shaded region respectively. This creates uncertainty in the measured phase, $\pm\Delta\phi$. The phase error can be determine by measuring the MLC I/Q errors and amplitude.

Determining the phase error for the detection system is complicated due to the characteristics of the MLC components and the surrounding electronic circuity. Factors such as different modulation frequencies (and any change in these frequencies), the incident optical AC and DC intensities (and hence the modulation depths) and any biasing currents applied to the MLC, all affect the system's phase error. A comprehensive overview of the noise characteristics at each stage of the MLC and the system as a whole is provided by the chip designer [55].

Due to the complexity of the system, a figure for the phase error was determined for the typical operating conditions described in section 4.1.2; light intensity of $43\,\text{W}\,\text{m}^{-2}$ with a modulation depth of ~28 %, and a LO frequency of 15 MHz (500 mVpp). The MLC output amplitude was measured to be 11.8 mV; this was determined by capturing (in differential) V_I (8.5 mV) and V_Q (8.0 mV) using an oscilloscope with 512 averages, and applying a 15 MHz+1 Hz optical signal. The I/Q phase noise as an RMS voltage was measured to be $\Delta V_{\text{Irms}} = 3.1\,\text{mV}$ and $\Delta V_{\text{Qrms}} = 2.2\,\text{mV}$, again using the oscilloscope but with no averages, and applying a 15 MHz optical signal. Referring to equation 3.7, the phase error is equal to $\Delta\phi = \pm\ 0.16$ radians (~9°).

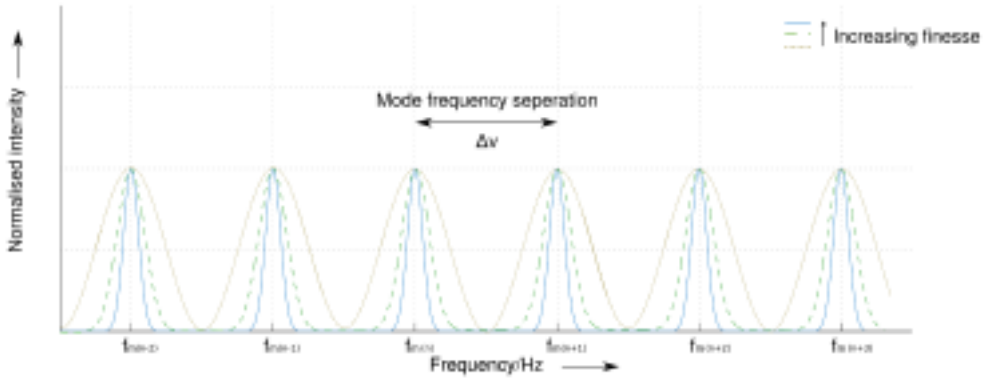

Figure 3.9: An example frequency plot of a laser's longitudinal modes. The modes have different emission centre frequencies, $f_{\mathrm{m(n)}}$ and is separated by Δv. Increasing the laser's cavity finesse (degree of feedback), shown in this example as yellow to green to blue indicating increasing finesse, increases the relative intensity at each mode's centre frequency.

3.2 Interferometer system methods and components

3.2.1 Laser sources

A laser is a device that emits light based on optical amplification through a stimulated emission process. A typical laser has a resonant optical cavity formed by mirrors; usually one mirror is slightly transmitting to allow the light out. A gain medium in the cavity provides amplification. The stimulated emission process means that photons in the cavity cause new photons to be emitted from the gain medium with the same wavelength, phase and direction.

The resonant cavity gives rise to different longitudinal and transverse modes. The laser cavity can be designed to suppress higher order transverse modes [106]. It is often the case that several longitudinal modes lase at the same time with different frequencies (f_m) separated by a mode separation frequency (Δv), as illustrated in figure 3.9. The frequencies of the longitudinal modes are determined by the properties of the laser cavity.

In continuous wave (CW) lasers, each mode has a narrow bandwidth. There is no correlation between each mode and a continuous beam is emitted from the

laser. It is possible for interference to occur between modes over brief periods of time, causing intensity fluctuations. This is lessened as the number of longitudinal modes increase (fluctuation is averaged over the number of modes). The narrow emission bandwidth of the CW laser indicates a large temporal coherence (section 1.4).

The interferometer arrangements described in this thesis use continuous wave helium neon (HeNe) lasers; a Uniphase 1100 series (1136p) 10 mW multi-mode CW laser [107] and two lab constructed stabilised two-mode 0.9 mW($\pm$0.5 mW) CW lasers [108]. A mixture of helium and neon gases in the laser's tubes are used as the gain medium. This gas medium determines the laser gain bandwidth (Δf_{gb}) and the centre frequency (f_{cf}) of the gain bandwidth. It is possible for a laser to have the centre frequency at different locations along the spectrum (with different gain bandwidths), however, the lasers used for this project are designed to emit at $f_{cf} = 474$ THz, or more usefully, at the red end of the visible spectrum at $\lambda_{cf} = 632.8$ nm. The gain bandwidth at this emission wavelength of a HeNe laser is $\Delta f_{gb} = 1.5$ GHz (full width half maximum) [109]; the laser will emit light with frequencies within this bandwidth.

By combining the gain bandwidth and the optical resonator conditions for the HeNe CW lasers, it is possible to see that only longitudinal modes that are present within the gain bandwidth region will be emitted from the laser; the number of potential emitted modes equals the number of mode separations within the gain bandwidth ($\frac{\Delta f_{gb}}{\Delta v}$). The Uniphase and the lab constructed lasers have a mode separation of 320 MHz and $\sim$650 MHz respectively. Additionally, each laser contains a lasing threshold (which exist due to absorption in the mirrors and scattering losses) which each mode must surpass for emission.

In the HeNe gas lasers, the frequency separation of the modes, and therefore the centre frequency of each mode, depend on the cavity length, L, (i.e. length between the mirrors). The mode frequency separation between each possible emitted frequency can be calculated by using equation 3.9. One of the features of a HeNe laser is that each alternative mode is orthogonally linearly polarised (maximum optical gain for a set of two longitudinal modes occurs when their polarisation is linear and perpendicular with respect to each other) [110].

$$\Delta v = \frac{c}{2L} \tag{3.9}$$

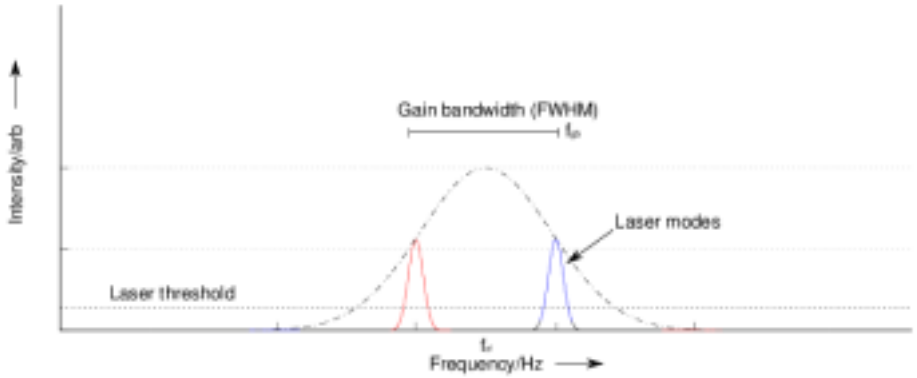

Figure 3.10: An example of a HeNe laser's emission spectrum. The laser will only emit modes that are within the gain bandwidth profile. The intensity of each mode must also be above the laser threshold. Each mode is linearly polarised and orthogonal to the proceeding mode, indicated in blue and red. Two linear and orthogonally polarised modes are emitted in this example laser; this changes as the cavity length varies.

HeNe CW lasers are used as the light source for the experiments in this thesis as they are inexpensive, simple, reliable and widely available with a variety of different optical powers. The narrow linewidth of each mode equates to a large temporal coherence, allowing for a degree of flexibility when designing the interferometers.

As discussed, the frequency (as well as the intensity) of each mode changes as the cavity length changes. The temperature of the laser can cause the contraction and expansion of the cavity (changing L). One of the requirements for the two laser interferometer system is a highly frequency stable (low drift) light source. The stabilised HeNe lasers used for the experiments described in chapter 6, constructed using inexpensive parts, provides this requirement.

3.2.2 Acousto-optic frequency shifters

In a heterodyne interferometer, beams with different optical frequencies are required. Heterodyne detection schemes have a limited operational bandwidth, and

crucially, the demodulation techniques they employ often require that the difference in the optical frequencies, and hence the phase relationship, is known and stationary (i.e. the interfering beams should be mutually coherent).

The simplest method of fulfilling this requirement is by using a single split source and shifting the optical frequency of one of the split beams. Since the function driving the shifting mechanism is known, the phase relationship between the shifted and un-shifted beam can be defined (as long as the coherence limits of the source are adhered to in the interferometer design). Another method involves phase-locking different laser sources using a common reference signal (section 2.4).

A common method of changing the optical frequency is by introducing a Doppler shift onto light [17]. As the position of the light source moves closer to or away from observation, the wavelength of the light wave shortens or lengthens respectively; this shift in wavelength (and therefore frequency) is dependent on the speed of the movement. In practice, having something move away or towards the detector indefinitely would be impossible, however, a variety of methods can be used to simulate the Doppler shift effect [111–117].

Acousto-optic frequency shifters (AOFS, also known as acousto-optic modulators or AOM) are used in the heterodyne interferometers described in this thesis to implement an optical frequency shift. An acousto-optic effect is produced by applying an acoustic wave into an optically transparent material (e.g. quartz). As the wave travels through the material, it causes periodic variations in the refractive index. This generates an effect analogous to a moving diffraction grating along the material with the site spacing equal to the wavelength of the acoustic wave.

An AOFS cell is constructed using a piezo-electric transducer to introduce the sound waves into the transparent material. A single cell can be designed to induce shifts centred within the 10^8-10^{11} Hz range (with a small bandwidth around this frequency).

The cells used for frequency shifting in the interferometer systems presented operate in the Raman-Nath regime [118] and are designed to generate multiple orders from incident light, all frequency shifted by an amount depending on their order.

This is in contrast to the Bragg regime, where only two orders are present at the exit of the cell, one of which is either up-shifted or down-shifted (depending on the angle of incidence) [119].

The AOFS diffraction pattern, showing the different orders generated, is shown in figure 3.11.

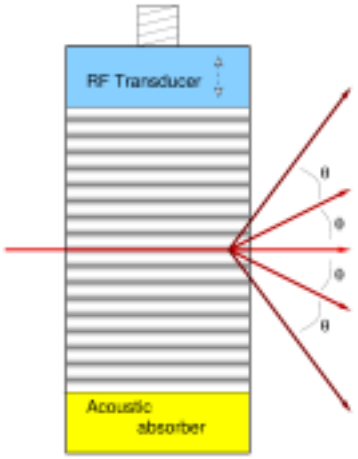

Figure 3.11: The operation diagram of an AOFS. A signal is fed to the transducer, which propagates an acoustic wave through the quartz (top to bottom). When light enters (left), the beam is diffracted at an angle and frequency shifted (right). The acoustic wave is absorbed on the other end of the quartz (bottom).

The angle of diffraction depends on the spacing between the 'grating fingers', which is determined by the wavelength of the sound wave. The angle of each order exiting the cell can be described using;

$$\sin\theta_m = \left(\frac{m\lambda}{\Lambda}\right) \tag{3.10}$$

where θ is the angle of diffraction for each m^{th} order ($m = \ldots, -2, -1, 0, 1, 2, \ldots$), and λ and Λ are the wavelengths of the light and sound waves respectively. The optical frequency is shifted on each diffraction order, such that;

$$f_{\mathrm{m-order}} \rightarrow f_{\mathrm{light}} + m f_{\mathrm{sound}} \tag{3.11}$$

where $f_{\mathrm{m-order}}$ is the frequency of the produced light at each m^{th} order, f_{light} is the frequency of the light entering the cell, and f_{sound} is frequency of the sound wave. The optical frequency shift is controlled by the frequency of the sound

wave. Interfering the 1^{st} and 0^{th} order beams from the AOFS would produce a pattern with a beat frequency equal to f_{sound}.

The experiments presented use AOFSs from Gooch and Housego (I-FS040). The devices are designed to operate at 40 MHz, with up to 99 % transmission at λ = 633 nm-680 nm [120, 121]. Working at this drive frequency (interfering $1^{st}/0^{th}$ orders), the interferogram modulation frequency would exceed the maximum operation frequency of the MLC (∼17 MHz).

One solution in producing lower frequency shifts is to use two AOFSs with slightly different frequencies to drive the cells (e.g. 40.0 MHz and 40.1 MHz). Combined, it is possible to generate a pattern ($1^{st}/1^{st}$ order interference) with a modulation frequency equal to the difference in driving frequencies (e.g. 100 kHz for 40.1 MHz and 40.0 MHz).

As mentioned, the AOFS diffraction angle is linked to the acoustic frequency and the AOFS is designed for this to be perpendicular to the device. If the AOFS is tilted by an angle, the angle of light incidence changes, along with the optimum drive frequency for the AOFS (i.e. a diffraction pattern can be generated if it is driven at a lower frequency). The AOFS cell in this new configuration is capable of shifting light down to ∼12 MHz, eliminating the need for a second cell at the expense of reduced light intensity for each diffracted order [122]. The heterodyne interferometers described in chapter 4 and chapter 5 use one AOFS. Each arrangement requires only one signal generator/amplifier (removing the need for a phase locking method if two AOFSs are used).

3.2.3 MLC interfacing

In each pixel of the MLC, incident light intensity is continuously detected and converted into an electronic signal. The signal is amplified, mixed with local reference signals and filtered, but remains continuous.

A diagram of the inputs and outputs of each pixel is illustrated in figure 3.12. Each pixel produces differential I (I^+_{out}/I^-_{out}) and Q (Q^+_{out}/Q^-_{out}) outputs, and a DC output. In addition, four pixels in the centre of the MLC array output an amplified version of the detected signal.

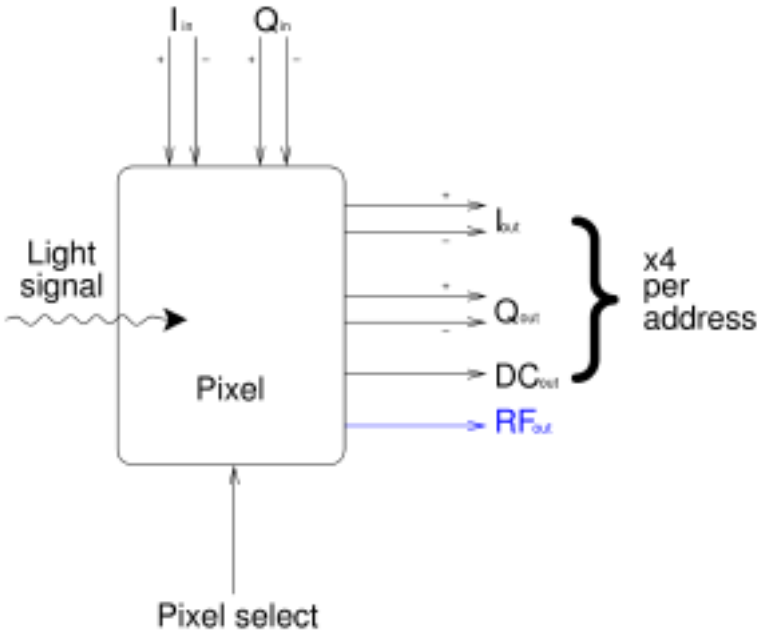

Figure 3.12: A diagram of the inputs and outputs of a single pixel in the MLC. The light intensity is detected, and mixed with local differential in-phase and quadrature sinusoidal signals. With one input address, four pixel are selected and their outputs can be observed at the output buffer.

The modulated light camera requires four local sinusoidal reference signals; each signal is the same except with a phase difference of 90° between them. The camera selects four pixels to output per address, hence a maximum of 20 outputs (plus 4 RF outputs) can be measured per address.

The acquisition and control system to extract and provide these signals is described in this section. It was built and written with the co-operation of Samuel Achamfuo-Yeboah [55].

3.2.3.1 Camera interface PCB

Over the course of the project, a variety of test PCBs had been designed and fabricated before the final version, described here, was used in the capture of the interferograms presented in chapter 4, chapter 5 and chapter 6. The PCB is used as an interface between the MLC chip and external devices; the aim was to directly link the MLC with a single signal generator, single ended 12 V power supply and an ADC (connected to a PC). The design of the PCB is based on the flow of signals around the acquisition system (in addition to external component

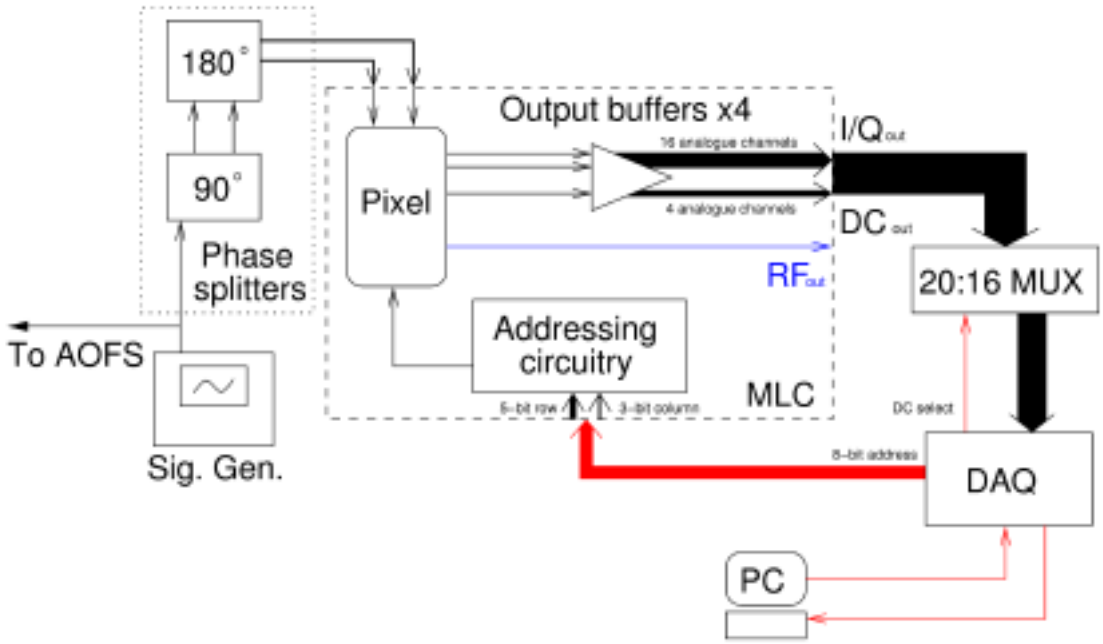

Figure 3.13: Schematic of image acquisition system. The MLC is represented by the centre block, with the local reference signal and addressing inputs, and I, Q and DC outputs the same as shown in figure 3.12. The local reference signal is taken from a signal generator and the output data is sent to the 16 input ADC under PC control. The PC sends addresses to the MLC via the ADC.

restrictions). A schematic of the acquisition system is illustrated in figure 3.13.

In the standard interferometer setup (chapter 4), the local oscillator signal is fed in to the PCB from a signal generator (Tektronix AFG 3252). This signal is also sent to the AOFS in the interferometer arrangement. Phase (differential I/Q) and DC output data is read using a 16 analogue-input data acquisition (DAQ) card (section 3.2.3.2) under PC control. The PC also sends in control signals to the MLC via the DAQ, most notably the pixel address (which selects four pixels for output). The schematic of the two-layer PCB used to interface these signals with the MLC is illustrated in figure 3.14.

This PCB contains power supply regulators (LM1117); two sets of the 3.3 V and 5 V versions (left of board) to supply power to the chip using the 12 V (top left of top layer) input, with the analogue supply separate to the digital supply. The local oscillator signal (input through an SMA connector in the top left of the board) is phase split on the PCB (left on the bottom layer); a Mini Circuits JSPQ-80+

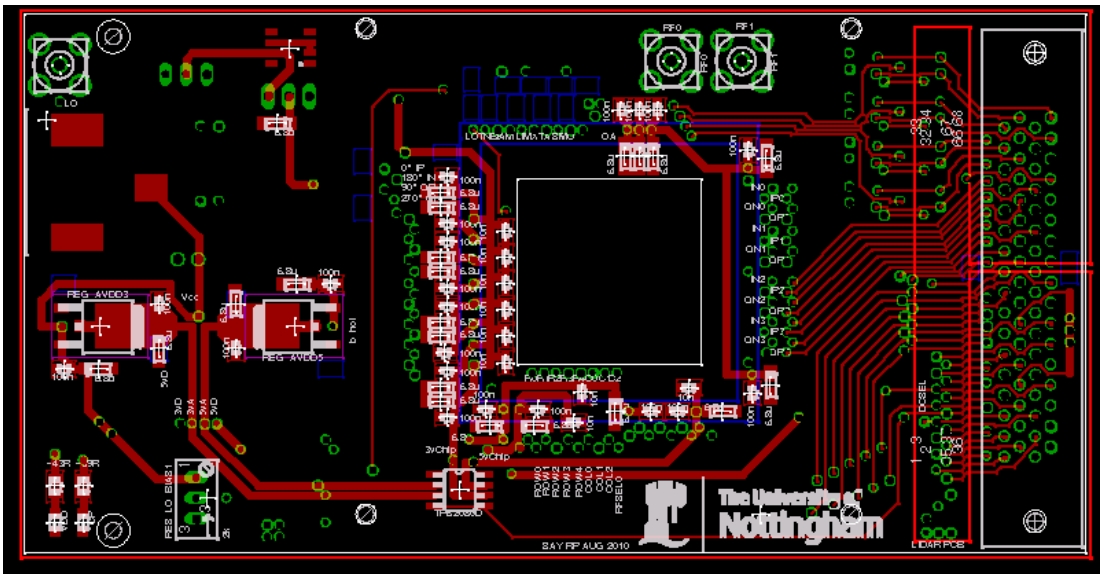

(a)

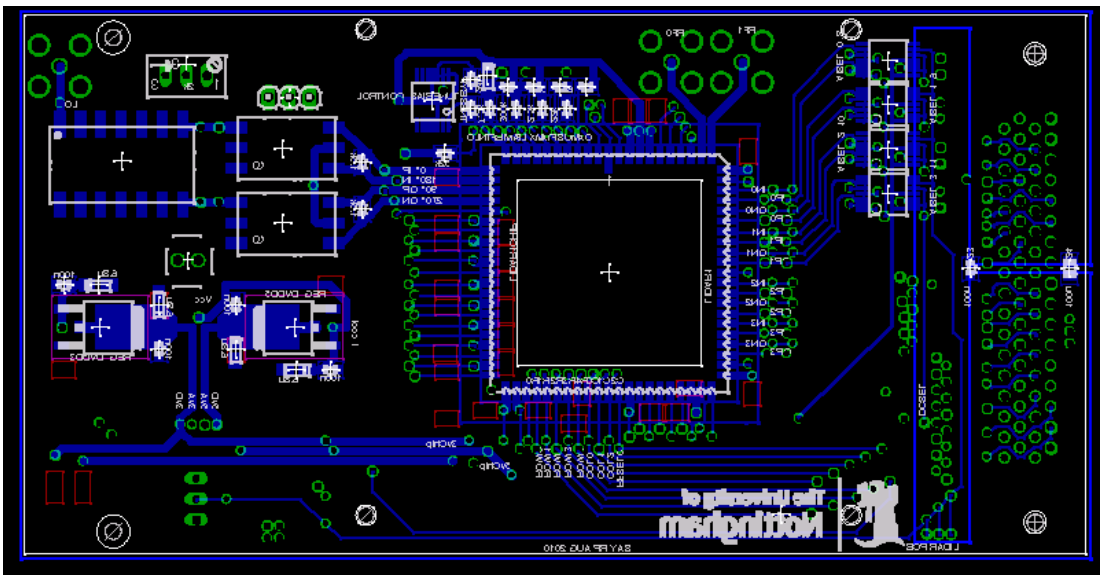

(b)

Figure 3.14: The top (a) and bottom (b) layer schematic of the PCB used to send and receive control and data signals from the MLC (chip holder), signal generator, oscilloscope (SMA) and PC (via DAQ board and SCSI 68-way port). The PCB was designed so that the majority of the inputs were kept on the left, the MLC in middle and the outputs on the right (with control signals on the top and bottom), as the MLC chip itself had been design in this manner.

and two T4-1 transformers are used to generate the in-phase and quadrature phase reference signals (90° split) and then into two sets of differential reference signals (180° split) respectively. These transformers have an operation band-

width of between 3 MHz and 80 MHz. The MLC itself fits in the centre of the PCB through a 84-pin chip holder.

The DAQ board interfaces with the PCB through a SCSI 68-way port (right). All 1024 pixels can be selected using an 8-bit address (5-bit row, 3-bit column), with four pixels selected at a time. Since there are 20 MLC outputs (Ip, In, Qp, Qn, DC $\times$ 4) and the DAQ only has 16 analogue inputs, a set of multiplexers (FSA2257) are used to switch between the DC outputs and arbitrarily chosen I/Q outputs. Whilst the MLC is capable of outputting four consistent RFout signals, only two have been chosen for output through SMA connectors (top of the board). This MLC chip has been designed with multiple pins to supply power to the internal circuitry [55]; each pin is fed the required voltage in series with individual bypass capacitors in order to prevent power spikes (which could potentially damage the chip). Finally, fixed resistors are used for biasing currents in the MLC (to control gain and bandwidth), with the resistor values chosen by the chip designer [55]. The chip consumes approximately 420 mA.

3.2.3.2 Acquisition and control ADC

Control signals to the MLC are sent from a PC, via a data acquisition (DAQ) card (NI PCI-6251) [123], using a 68-way SCSI port and shielded cable. The DAQ card has a 16-bit 16 channel ADC and is capable of a 1 Ms s^{-1} multi-channel acquisition rate, i.e. a single sample on a single channel can be measured in $t = \frac{1}{1(\mathrm{M})} = 1\,\mu$s. Given the multi-channel acquisition rate, a single DC intensity frame capture (1024 pixels) could be completed in 1 ms, with a complete phase image capture (I^+, I^-, Q^+ and Q^-) taking $\sim$4 ms, giving a maximum theoretical frame rate of 250 frames s^{-1}.

In addition to receiving data, the DAQ is also used to send control signals, such as the multiplexer switch signal and the 8-bit address, to the PCB.

3.2.3.3 PC interface programs

The acquisition and control software was written in C and Matlab. Comedi v0.8 [124] was used to communicate with the DAQ card. It was determined that the PC processing time was the bottleneck in the overall frame rate, so tech-

niques such as addressing in Gray code [125], which also prevents the possibility of spurious data as is possible in binary counting (i.e. different pixels selected if each address line has different propagation times), and saving the read data as a binary file, were employed to reduce the PC processing times. The averaging of each pixel's data was conducted before the data was saved. The total time for both image and phase frame grab (no averaging) was 25 ms, giving a frame rate of 40 frames s^{-1}.

Matlab was used to perform the `atan2` function to extract phase and for reshaping the raw data into images, which were both saved and displayed on-screen; this typically took around 0.4 s per frame.

3.2.4 Capture procedure

When capturing an image, a few considerations have to be made to minimise noise contributions to the image, as well as reduce the errors in the phase calculation due to the MLC's non-linear frontend.

Section 3.1.3.1 discusses how, in order to achieve a frontend response that appears linear, the incident light (equation 1.17) is required to have a large DC component (I_{DC}) and a small AC component (A). In other words, a high intensity, low modulation depth optical signal. Considering the heterodyne interference equation (equation 1.17), this can be achieved by interfering beams with large intensity differences. i.e. low and high intensity beams.

For the situation where random noise becomes prevalent in a captured image, data averaging can be used. Given that the random noise content (with a mean of zero) of the system has the value N without averaging, a decrease of this noise figure of $N/\sqrt{n}$ would be observable with averaging, where n is the number of averages. If the assumption is made that there is no correlation between the system signal and noise (and that the signal value remains constant in each captured image), the SNR increases by $\sqrt{n}$. This is analogous to increasing the integration time on a CCD camera. The disadvantage of averaging is a decrease in the system frame rate (increase in read time per pixel). In addition, low frequency drift in an interference fringe position will result in the reduction of fringe visibility (explored in section 1.7.5), as it will add systematic errors into an image (depending

on the frame capture time).

As discussed in section 1.7.4, the modular array design of the MLC ensures, in theory, that each pixel operates in the same way. However, in practice, factors such as slight physical variations and the power distribution introduces fixed pattern noise (FPN) into each image. One component of the FPN can be described as the dark signal non-uniformity. In a standard camera, this is an offset observable in each pixel's output with no light incident. It is eliminated post capture by capturing an initial 'dark' image (FPN image) and removing the offset from each 'irradiated' image captured. This becomes more complex for a camera with a logarithmic frontend pixel; the 'fixed' pattern noise is no longer independent of illumination and assumes non-linear behaviour [126]. Fortunately, since one of the major objectives is to operate in a 'linear' region of the camera, the FPN image is captured with DC light present (and no AC light). As long as images are captured with incident light intensity around this DC light level, the assumption is made that FPN is eliminated.

Chapter 4

Widefield heterodyne interferometer

In this chapter, the interferometer system developed to capture widefield heterodyne interferograms using the MLC is presented. The MLC is used to capture homodyne and heterodyne interferograms, with comparisons made between the images and system arrangements. Modelled images, calculated using knowledge of incident wavefronts, are compared with the measured results. As a proof-of-concept experiment, a phase shifting object is placed within the interferometer and the phase change in the interferogram is captured.

4.1 Widefield heterodyne interferometer outline

4.1.1 Interferometer system brief

Widefield interferograms show the phase variations across the spatial domain of an interference fringe pattern. Capturing this widefield phase information can be useful when determining the difference in the optical path length between interfering beams at individual spatial point of capture; the position of each pixel on a camera array determine these points (assuming a static camera is used for capture).

The focus of this initial investigation, presented in this chapter, is to show the MLC's capability of capturing, demodulating, and outputting the phase of an incident heterodyne interference pattern. The MLC is also able to capture static (DC) intensity; a comparison between the captured DC and modulated fringe

patterns can easily be made. The interferometer was setup to produce homodyne and heterodyne interference patterns separately.

The interferogram images captured by the MLC can be compared against expected modelled images. Fringe patterns generated in an interferometer depend on the wavefront properties of the interfering beams. By measuring and adjusting the distances between certain optical components (i.e. lenses) within the interferometer, and determining the characteristics of the wavefronts using these distances, an expected (i.e. incident on to each pixel of the MLC) phase image can be generated.

As a proof of concept experiment, a microscope slide was placed half way across one of the interfering beams. By measuring the fringe pattern before (control image) and after the slide was introduced, and determining the difference between them, a confirmation can be made that the phase shift observed in the output image was due to the slide (comparing the covered/uncovered side of the image).

4.1.2 Heterodyne interferometer arrangement

To capture widefield interferograms, the MLC was used in the configuration described in figure 3.13 and incorporated into a Mach-Zehnder interferometer. A light beam was split using a beamsplitter into object and reference arms. Taking separate paths, the beams were recombined using another beamsplitter, where interference occurred. One arm of the interferometer passed through an AOFS and a fixed spatial filter with a laterally movable entry lens. A schematic of the interferometer setup is illustrated in figure 4.1, with a photograph of the setup shown in figure 4.2.

The light source used in this system was a Uniphase 1100 series (1136p) 10 mW HeNe ($\lambda = 633\,\text{nm}$) laser [107]. The Uniphase 1100 series HeNe lasers have a coherence length of $\sim$40 cm [127]. In this Mach-Zehnder interferometer arrangement, the path length difference was less than the coherence length of the source (path length difference was the combination of the light through the AOFS, the modified spatial filter, and any difference in the wavefronts and the sample). With the light passing through the AOFS and the spatial filter arrangement, some of its intensity was lost (due to the low drive frequency and slight optics misalignment);

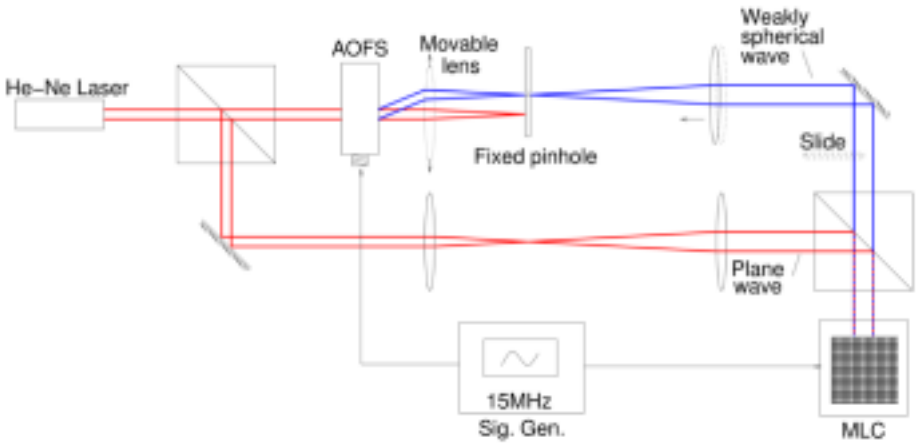

Figure 4.1: The Mach-Zehnder homodyne/heterodyne interferometer used a fixed spatial filter/pinhole and a movable lens so that it could switch between homodyne and heterodyne modes while preserving the generated interferogram. In heterodyne mode, the AOFS shifted the frequency of one arm of the interferometer, resulting in a modulated interferogram at the detector. A signal from the signal generator (sine wave with frequency $f = 15\,\mathrm{MHz}$) drove the AOFS via an amplifier. The same signal was also used (after phase splitting) as the local oscillator in the MLC for mixing.

the intensity of the object (blue) and reference (red) beams were measured (using an optical power-meter) to be $0.76\,\mathrm{W\,m^{-2}}$ and $42.03\,\mathrm{W\,m^{-2}}$ respectively. This measured value was the average profile intensity, as the beam emitted from the laser had a Gaussian profile (as indicated in figure 4.3(a)). While the reduction in intensity in one of the interferometer arms reduced the overall optical signal to the MLC, it was not entirely disadvantageous. As discussed in section 3.2.4, for the MLC's frontend to operate in the 'linear' region, the incident modulated light requires a high DC intensity and low modulation depth; this was achieved with this arrangement (approximately 28% modulation depth).

The MLC was capable of outputting (simultaneously) the DC intensity and AC phase information (after demodulation). The described setup was used to switch between homodyne and heterodyne modes; by moving the entrance lens of the spatial filter, either the 0^{th} or the 1^{st} order output (discussed in section 3.2.2) from the AOFS could be selected to pass through the pinhole which then interfered with the other arm of the interferometer. When the 0^{th} order was selected, both interfering beams had the same optical frequency (homodyne interference). When the 1^{st} order was selected, the interfering beams had a frequency difference equal to the AOFS drive frequency (heterodyne interference). The drive frequency was

chosen to be 15 MHz as this is within both the lower operating frequency threshold of the AOFS (discussed in section 3.2.2) and the upper operating limit of the MLC (expressed in section 3.1.1). The spatial filter arrangement allowed for a quick switch between the interferometer modes without changing the spatial phase relationship between the interferometer arms; i.e. the interferogram observed in the homodyne mode was the same as in the heterodyne mode. This aided in the alignment for the heterodyne mode, since the homodyne interference pattern was visible by eye.

The size and position of each beams were adjusted using a beam expander arrangement. The reference and object arms produced plane and weakly spherical waves respectively, generating a concentric circular fringe pattern. The images presented in this chapter used 50 averages to reduce the amount of random noise (discussed in section 3.2.4).

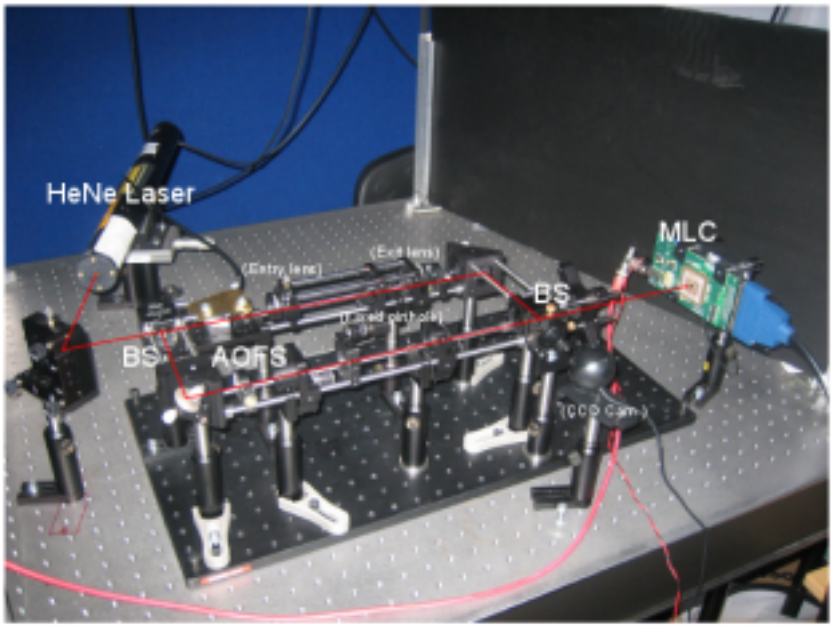

Figure 4.2: Photograph of the heterodyne interferometer shown in figure 4.1; beam path is indicated along with the key components in the arrangement.

4.2 Heterodyne-Homodyne mode image comparison

Since the beam profile from the laser was Gaussian, the light intensity incident on the MLC array was non-uniform. An intensity (DC) image captured of the object beam (the higher intensity beam) is illustrated in figure 4.3(a) (captured by covering up the reference beam). When the interferometer was set into homodyne mode (0^{th} order transmitted through), a DC fringe pattern was generated; the captured image is illustrated in figure 4.3(b).

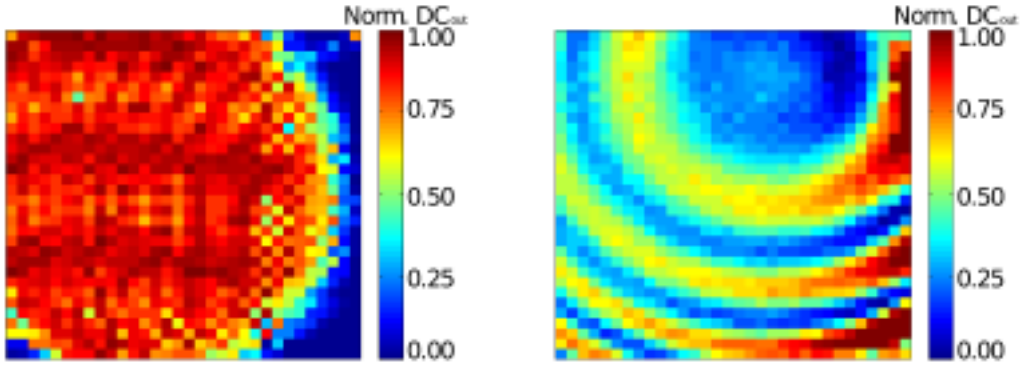

(a) **(b)**

Figure 4.3: Captured DC image of (a) the reference arm beam profile and of (b) a circular fringe pattern. Both images show normalised measured outputs.

A circular fringe pattern was visible in the homodyne interferogram image, with the centre of the circles apparent at the top. The pattern image (figure 4.3(b)) shows a variation in the fringe visibility, represented by the range between the peaks and troughs. The range variation correlates with the beam profile image (figure 4.3(a)), which shows that the DC intensity is inversely proportional to the homodyne fringe pattern visibility. This observation agrees with the camera's logarithmic frontend response (i.e. larger output voltage range with lower input photocurrents). Non-uniform DC offsets across a homodyne fringe pattern, such as in this instance, make direct phase determination difficult (discussed in section 1.3.4). Therefore, a phase extraction technique was required; a phase image was constructed using the spatial domain filtering method (discussed in section 1.3.5). The captured image was filtered digitally using a 2D FFT Matlab routine with aim of removing the DC spatial offset. Looking at the interferogram,

the centre of the concentric circle fringe pattern is at the top, so a simple ideal filter was applied to all positive y-axis spatial components (i.e. reduced to zero). A 2D IFFT was applied to the filtered output. A phase image was constructed by performing an inverse tangent operation on the imaginary part over the real part of the IFFT output; the resultant image is illustrated in figure 4.4.

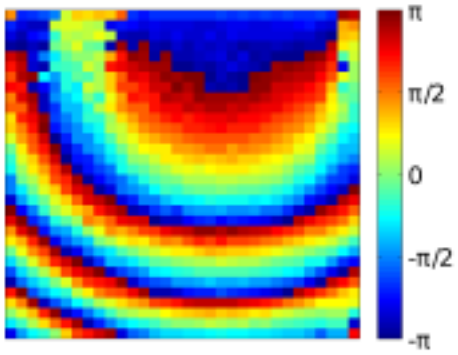

Figure 4.4: Constructed phase image using the DC fringe pattern. A Matlab script was used to perform a 2D FFT on the pattern and to apply an ideal filter. After an inverse FFT, an inverse tangent operation was performed using to the resultant real and imaginary parts in order to determine the phase.

The heterodyne interferogram was captured by switching the interferometer into heterodyne mode (transmitting 1^{st} order through). The phase information of the incident modulated light was determined by measuring the in-phase and quadrature phase outputs from of each pixel (I^+, I^-, Q^+ and Q^- outs); the captured differential I and Q outputs (in image form) are illustrated in figures 4.5(a) and (b).

The I/Q images show the heterodyne fringe pattern; the fringe pattern is in the same position as in the homodyne interferogram. The images show a phase difference between the patterns equal to 90°. The I/Q data was used to construct a phase image (equation 3.5), illustrated in figure 4.6.

As expected, the heterodyne interferogram phase image shows the same fringe pattern seen in the homodyne image. However, unlike the homodyne case, phase information was available immediately (after an inverse tangent operation) and displayed phase independent of the DC/low frequency offset.

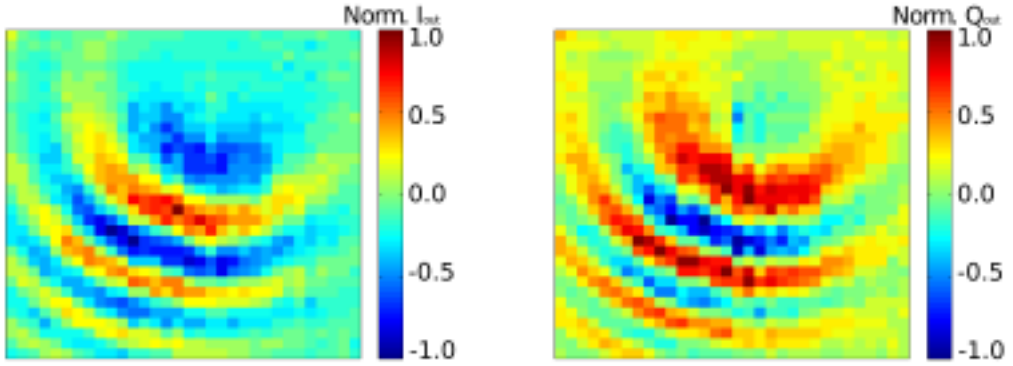

(a) (b)

Figure 4.5: The differential (a) in-phase (Ip-In) and (b) quadrature phase (Qp-Qn) images of the heterodyne interferometer fringe pattern. The colours represent the normalised measured signal from the MLC.

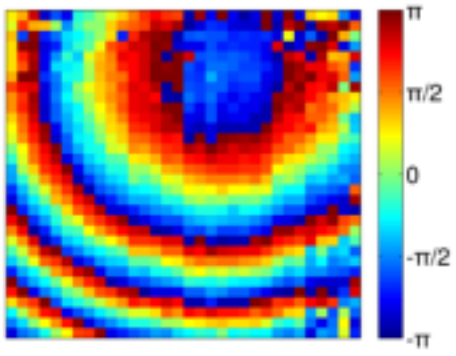

Figure 4.6: AC phase output image of the heterodyne interferogram. The output was generated using the IQ images.

4.3 Measured and modelled image comparisons

To ensure the MLC operated as expected, theoretical fringe pattern images were generated using a program to corroborate measurements made in the optical arrangement setup. Circular fringe patterns in this setup were generated by interfering a weakly spherical wave and a plane wave. A diagram and the parameters of the setup is described in Appendix A.

The heterodyne fringe pattern captured using this setup is illustrated in figure 4.7(a). The program, written in Matlab, produced theoretical fringe pattern images using the data described in Appendix A, except for δm_L (ref. equation A.1), which was varied to find a theory image of best fit with respect to the

measured image, shown in figure 4.7(b). The theoretical image (a), was calculated given the distances between the lens and the detector.

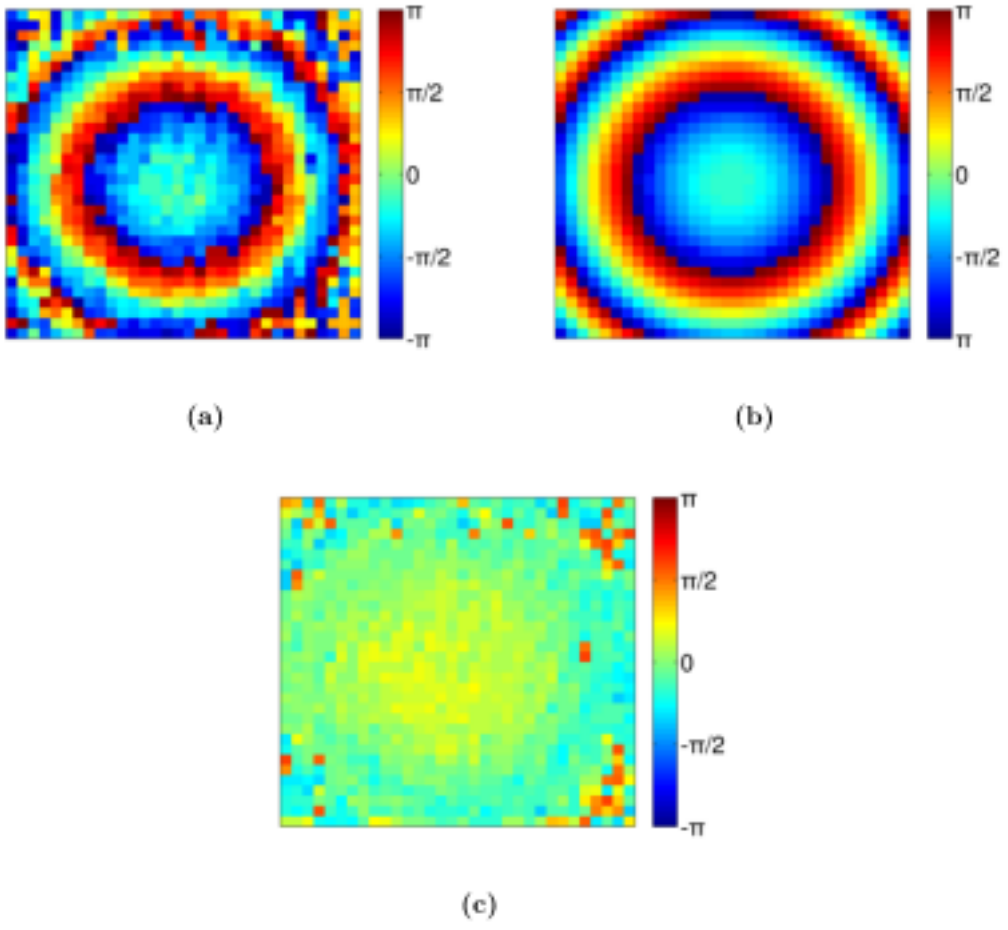

Figure 4.7: Circular fringe pattern images. The measured image (a) was capture under the conditions described in this section, with the theory image (b) determined using a Matlab program, varying lens displacement and beam angle parameters to find an image of best fit. The difference (c) between the measured and theory images is displayed as a modulo 2π image.

Excepting the noise, the theory and measured interferograms appear similar; the position and size of the circular fringes are comparable. Figure 4.7(c) illustrates the difference between the measured and theory images as a modulo 2π image (to remove phase steps and restrict the difference range to 2π). The δm_L value determined by the program was equal to 4.8 mm (with parameter steps of 0.1 mm). The difference image does indicate that there is a slight fringe pattern difference, however, this can be explained as experimental error for all the parameters described at beginning of this section. Additionally, the best fit determination could

have been skewed by the noise prevalent near the edges of the image.

4.4 Object characterisation experiment

To perform an interferometry experiment, a microscope slide was placed over half the object beam; this changed the phase relationship $\phi(x, y)$ across the covered half. To capture the phase change, the MLC was used to capture the heterodyne fringe pattern before and after the microscope slide had been introduced into the interferometer; the captured images are illustrated in figure 4.8(a) (no-slide image) and figure 4.8(c) (slide image) respectively.

To aid in determining the phase change, each image had been unwrapped; the unwrapping process extends the phase measurement range beyond the 2π range, removing phase steps. The complexity of the unwrapping process depends on whether the captured phase data is in 1D or 2D, and on the fringe pattern shape (an advantage of capturing a simple circular fringe pattern). This process was implemented post-capture; figure 4.8(b) and figure 4.8(d) illustrates the difference images between a non-slide and slide image respectively, and a control image, after applying a 2D unwrapping routine (in Matlab [128]).

The slide covered the left half of the MLC (x-axis pixels approximately less than 16), with the right half of the MLC (x-axis pixels approximately more than 18) being uncovered. Figure 4.8(c) shows the phase image measured with the slide placed in the setup and figure 4.8(d) shows the unwrapped difference image between the slide and control image. The right side of the image is constant as in figure 4.8(b) meaning that this side has the same fringe pattern as the control image (therefore no slide is present). The phase on the left side of the image has changed in figure 4.8(d) as is consistent with the introduction of the slide.

4.5 Widefield heterodyne system discussion

The heterodyne interferometer system described in this chapter was used to investigate the viability of capturing a widefield fringe pattern using the MLC described in section 3.1. The MLC is capable of capturing a modulated optical

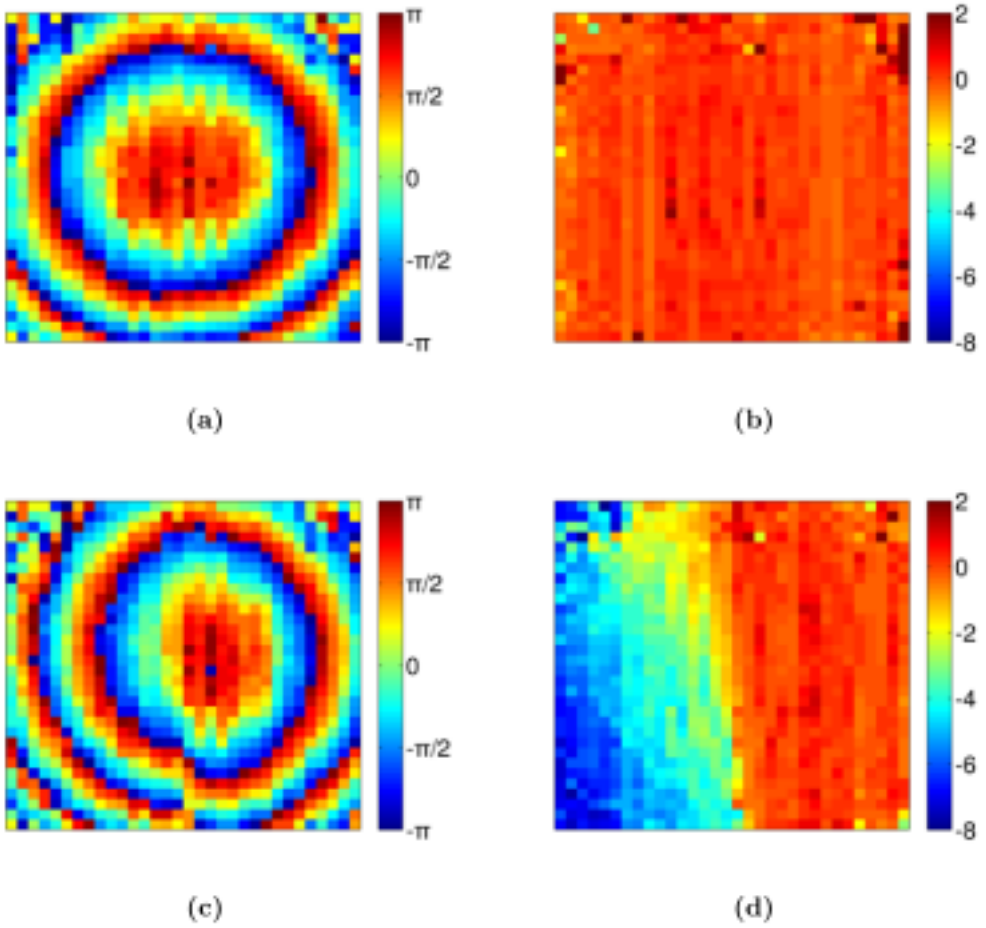

Figure 4.8: Phase images of (left) heterodyne fringe patterns (a) without a slide, (c) with a slide present in the left half of the object arm (incident on the left half of the MLC array). The images are unwrapped, and the difference between them and a control image are presented (right) (b) without the slide, (d) with a slide. Colour represents the phase in radians (which extend beyond the 2π range in the unwrapped images).

signal and outputting readily (after pixel select) continuous DC and AC phase values in quadrature, which are directly proportional (assuming linear operation) to the respective optical signal components; the continuous output is available due to the camera's use of HF amplifiers instead of using signal bins. Real time widefield images can be captured using the camera without relying on a scanning technique. The size of MLC chip (3.68 mm × 3.68 mm) is comparable with other digital camera sensor arrays, and its CMOS architecture allows for random individual pixel access (allowing information capture on a smaller selection of pixels for increased frame rates).

As the MLC is capable of outputting the low frequency intensity information and the high frequency phase information of an incident optical signal, the device was used to capture both homodyne and heterodyne widefield interferograms using a modified Mach-Zehnder arrangement. Using an AOFS and spatial filter combination, the interferometer was capable of generating both homodyne and heterodyne fringe patterns by switching between whether the 0^{th} or 1^{st} AOFS order interfered with the reference arm. The AOFS was driven using an externally generated 15 MHz sinusoidal signal. The captured homodyne and heterodyne fringe pattern is illustrated in figure 4.3(b) and figure 4.6 (derived using the I/Q outputs illustrated in figure 4.5(a)/(b)) respectively. As well as confirming that the MLC functions as expected, the similar pattern images showed that by using the modified spatial filter, the spatial phase relationship was maintained between the object and reference beam independent of the AOFS order selected.

One method of extracting the phase from a homodyne pattern is by using the spatial domain filtering method (discussed in section 1.3.5). Considering the setup described in this chapter, this method was preferred over other methods such as phase shifting interferometry as only one DC pattern image was required, whilst pattern range variations (DC background influences and low frequency background influences) are removed. The resultant image is illustrated in figure 4.4. Some information was lost from the top of the image and a more complicated filter could be applied to avoid the loss of this information. However, the image is in good agreement with the heterodyne phase image (figure 4.6). Both images produce phase images without influence from intensity offset variations.

While the spatially filtered images display less random noise than the measured heterodyne image, there will be increased phase uncertainty due to errors introduced by the filtering process. For a more diverse range of generated fringe patterns or a changing fringe pattern, different and complex filters would need to be applied. In contrast, the heterodyne setup produces a fringe pattern directly, independent of the fringe pattern generated.

To show a proof of system concept, two measurement experiments were conducted. The first of the two experiments compared the measurements made when capturing a heterodyne fringe pattern against values used in a computer generated theory image (illustrated in figure 4.7(a)). The theory image of best

fit, illustrated in figure 4.7(b), was determined by adjusting one value, δm_L, in the model illustrated in figure A.1; 4.8 mm was calculated whilst the measured result was 5.0 mm, which is within a margin of human measurement error. The second experiment conducted involved placing a microscope slide in the object arm of the interferometer. Unwrapped pattern images captured before and after the introduction of the slide was illustrated in figure 4.8(b) and figure 4.8(d).

Each of the pattern images captured contain errors due to random noise influencing the measured I/Q voltage signals (e.g. notable between the measured and theory images in figure 4.7(a) and figure 4.7(b)). An analysis of the phase error was presented in section 3.1.3.3. Conducting a full noise analysis on the MLC is complicated (an in-depth analysis is provided by the chip designer [55]), so the phase error of $\Delta\phi = \pm 9.1^\circ$ was determined under the conditions described in section 4.1.2. The light intensity measurement of $43\,\mathrm{W\,m^{-2}}$ was made using an optical power meter (which averages the incident power received across its detection head), and in determining the phase error, the assumption was made that this intensity was uniform across the array. In practice, the images show more noise nearer the edges, where the SNR was lower due to the laser's Gaussian beam profile (receiving less light than at the centre). To reduce the amount of random noise visible in each image, sample averaging could be used. Random noise would be reduced by $\sqrt{n}$, where n is the number of samples taken for averaging (explored in section 3.2.4). However, this process would increase the image capture time.

The performance of the system described in this chapter can be compared against other widefield heterodyne detection systems described in section 2.2. The parallel detection (64 device) system developed by Massie [15] for use in capturing heterodyne fringe patterns, was reported to have a phase accuracy of $\lambda/100$ (3.6°), working with modulation frequency of 1 MHz, capturing at a frame rate of 100K fps. However, a complex parallel system such as this is unsuitable for many applications due to its size, cost and power requirements. The 58×58 smart pixel CMOS camera designed by Bourquin was used in a heterodyne reflectometer application [77, 78]; the camera could detect modulation frequencies of upto 1 MHz, with readout speeds of upto 300 fps and had a maximum output SNR of $\mathrm{SNR_{out}} = (\frac{1560\,\mathrm{mV}}{0.81\,\mathrm{mV}})^2 = 65.7\mathrm{dB}$. However, as this camera used a rectifier circuit for signal demodulation, only the signal amplitude was obtainable (and

not the phase). The 64×64 pixel 3PCIS CMOS camera developed by Kimachi was used in a heterodyne Michelson interferometer system and was capable extracting phase information from a 25 kHz optical signal at 30 fps [25]. A phase accuracy of 0.85° was reported (an updated camera design includes a 200×200 pixel array [16]). The camera units used in these systems can be compared with modern commercially available modulated light cameras, such as the PMD [129]; the camera contains a 160×120 pixel array, capturing optical signals with modulation frequencies of upto 80 MHz at 90 fps with a typical LIDAR measurement error (at 10 MHz) of 5 mm/1500 mm (1.2°).

An initial comparison show that these other detection systems are superior to the system described in this chapter, when considering phase error, modulation frequency and pixel count. However, there are some advantages that the MLC has over these other systems. The notable feature of the MLC is its ability to output continuous phase information (by using amplifiers and mixers instead of using sampling bins). The phase of a fringe pattern can be determined (in the widefield region) directly, without waiting for an integration period, without performing phase stepping, and without an extensive post capture processing. The MLC is able to demodulate in the 10^6Hz region (tests conducted by the chip creator reported on detecting upto 50 MHz [55]) using on-chip circuitry. In combination with the output low pass filter (which is the equivelent of applying a sharp filter at the high modulation frequency, shown in figure 3.7(d)), the MLC has the potential to reduce the influence of noise (e.g. flicker noise) on an output that other systems may not be able to. However, the MLC is a prototype device, and as such, is not as optimised as it could be. It should be possible for an improved MLC design to feature a higher modulation frequency and a reduction of in-system noise [55].

Chapter 5

Ultrastable widefield heterodyne interferometer

This chapter describes the operation of the ultrastable heterodyne interferometer system. The stability of the system is compared with the standard interferometer setup by inducing vibration into the system. Images of interferograms are presented as well as an analysis of the system and its immunity.

5.1 Ultrastable interferometer outline

5.1.1 Ultrastable system brief

Microphonics and vibration on interferometers introduce an unwanted time varying phase variation (with an unknown function) into each arm. If this variation is fast compared with the frame rate of the detector, the fringe visibility could be lost entirely (as discussed section 1.7.5). One common form of vibration observed in an interferometer system is piston phase, where the same temporally varying OPL is seen across the interferogram.

In the standard interferometer scheme described in chapter 4, the local reference signal fed to the mixers was derived from the signal generator (which also drove the AOFS). The system described in this chapter utilised the same interferometer arrangement but was converted into an ultrastable system by using the RFout from one of the four special pixels on the camera that output the raw detected signal, as the local reference signal.

The ultrastable interferometer system was tested in a modified Mach-Zehnder arrangement by applying a vibration to one of the interferometer mirrors which was implemented by fixing the driver from a disassembled loudspeaker to an object arm mirror. As the vibration could be controlled, and the switch between the standard and ultrastable modes could simply be made by changing over a lead in the setup, comparisons could easily be made between the stable relative images captured using the ultrastable system and the unstable absolute images captured using the standard setup.

The vibrating mirror experiment could only be used as long as the OPL change was uniform across the array (i.e. only piston vibration), and it was observed that at large mirror vibration amplitudes, this was no longer the case. Hence, an experiment was designed to simulate the effects of vibration on the system. This was achieved by varying the modulation frequency, as this was related to the amount of constant OPL change. The ultrastable system was also used in a practical experiment, profiling the height of a chrome grating ($\sim$150 nm depth) in real time and in the widefield region.

5.1.2 Ultrastable system operation

The interferometer setup described in section 4.1.2 (described here as the standard interferometer arrangement) used the signal taken from an external signal generator as the LO reference for the quadrature mixing process. In contrast, the ultrastable interferometer uses the RFout signal as a feedback to compensate for the temporally varying phase observable across an entire interferogram (i.e. changing piston phase); this internal reference signal contains the same temporally varying phase term seen on each pixel. The interferograms generated using the ultrastable system display the phase captured (at each pixel) relative to the phase observed at a single pixel on the MLC array. The RFout signal is continuously output, i.e. no need to be addressed, and is routed off chip, amplified and filtered. A schematic of the operation is illustrated in figure 5.1.

The detected intensity of an incident heterodyne fringe pattern expressed by equation 1.17 describes a stable pattern, where the frequency difference between the interfering beams (i.e. beat or modulation frequency) do not change (making the function simple to express). If vibration is introduced into the system,

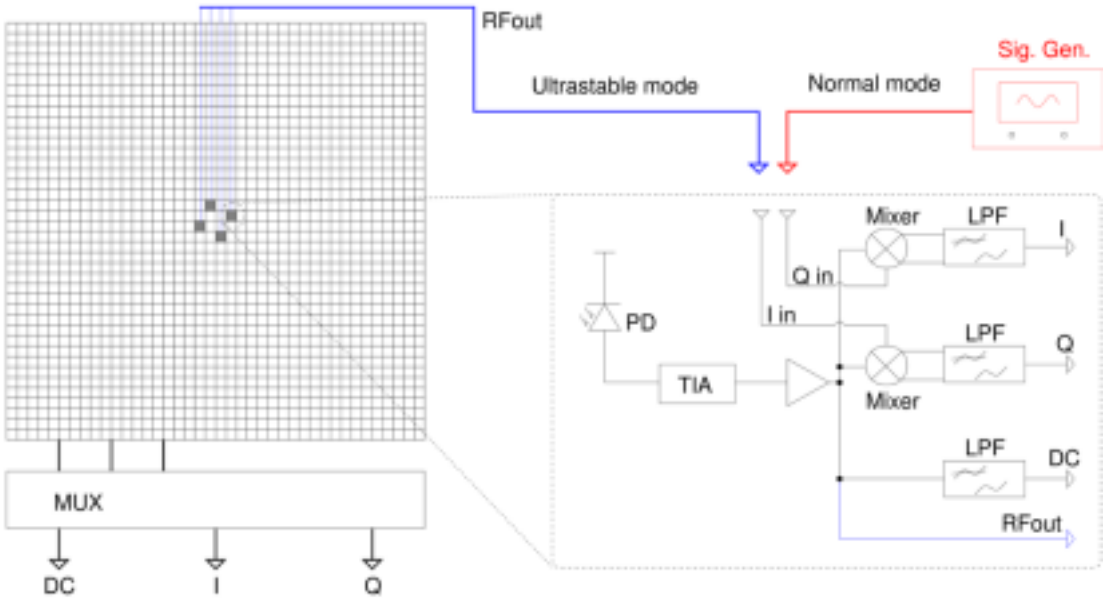

Figure 5.1: A schematic of the MLC camera array and of an RFout pixel. Four pixels in the array contain additional circuitry that allows them to output the raw RF (pre-mixed) signal. In the standard mode of operation, the I_{LO} and Q_{LO} inputs are driven by a signal generator. In the ultrastable mode, they are driven by signals derived from the RFout signal (i.e. signal feedback). The signal is filtered and amplified before being phase split.

an additional temporally varying phase term is required in the expression. The expression of a constant carrier beat frequency signal (plus phase offset) and an introduced phase variation is analogous to phase modulation in analogue communication systems [33], such that the AC angle function varies linearly with the phase change induced by the OPL shift due to vibration. Equation 5.1 expresses the heterodyne fringe pattern intensity with this additional unknown temporally varying vibration term, $\psi_d(t)$, between the interfering arms;

$$I = I_{\mathrm{DC}} + A\cos(\omega_d t + \phi_d + \psi_d(t)) \tag{5.1}$$

The goal of producing a stable interferogram is achieved by extracting the 'useful' phase difference ϕ, while eliminating ψ. For example, in a common path interferometer, the beam paths are almost identical (therefore the temporally varying phase difference $\psi_d \approx 0$).

5.1.2.1 Eliminating instability

In the ultrastable system described by figure 5.1, the temporally varying phase difference, ψ_d, is eliminated by using the signal from a single RFout pixel (equation 5.1) as the LO mixer signal. This is implemented on each individual pixel and requires spatial coherence in the fringe pattern (i.e. the same ψ_d and ω_d measured on each pixel). Considering the MLC mixing process discussed in section 3.1.2, the in-phase and quadrature phase outputs from the camera in this ultrastable configuration can be described by;

$$\begin{aligned} I_{\text{out}} &= V_{\text{DC}}V_{\text{RFDC}} + \frac{V_{\text{AC}}V_{\text{RFAC}}}{2}\cos(\phi_d(x,y) - \phi_{\text{RFd}} + \psi_d(t) - \psi_{\text{RFd}}(t)) \\ &= V_{\text{DC}}V_{\text{RFDC}} + \frac{V_{\text{AC}}V_{\text{RFAC}}}{2}\cos(\phi_d(x,y) - \phi_{\text{RFd}}) \\ Q_{\text{out}} &= V_{\text{DC}}V_{\text{RFDC}} + \frac{V_{\text{AC}}V_{\text{RFAC}}}{2}\sin(\phi_d(x,y) - \phi_{\text{RFd}} + \psi_d(t) - \psi_{\text{RFd}}(t)) \\ &= V_{\text{DC}}V_{\text{RFDC}} + \frac{V_{\text{AC}}V_{\text{RFAC}}}{2}\sin(\phi_d(x,y) - \phi_{\text{RFd}}) \end{aligned} \tag{5.2}$$

The phase can be extracted using;

$$\phi_d(x,y) - \phi_{\text{RFd}} = \arctan\left(\frac{Q^+_{\text{out}} - Q^-_{\text{out}}}{I^+_{\text{out}} - I^-_{\text{out}}}\right) \tag{5.3}$$

The phase determined using this setup does not contain the temporally varying phase term, $\psi_d(t)$. The determined phase does contain the RF pixel's phase term (ϕ_{RFd}), i.e. relative phase is measured, however it is possible to remove this post capture if the absolute phase is measured separately.

5.1.2.2 Limitations of the system

It is important to note that the ultrastable system is only immune to piston phase vibrations (i.e. the same temporal phase shifts in the fringe pattern observable across the whole camera array). It is possible for the temporally varying phase to vary with different functions at different points across the beam, i.e. has spatial and temporal dependence, $\psi(t) \rightarrow \psi(x,y,t)$.

Another potentially restrictive factor of using the ultrastable system is that each interferogram will be a relative phase pattern (to RFout pixel). This is in contrast with the standard interferometer setup (section 4.1.2), which measures the absolute phase (i.e. total OPL difference is measured). In a point detection scheme,

solely detecting the relative phase may not be useful, but in the widefield region (captured either through scans or multi-point detectors), it is possible to directly determine the interfering wavefront information. It should be noted however, that by using an external fringe counting system with the RFout signal, it would be possible to acquire the absolute phase (combining this information with the relative phase image would generate an absolute phase image).

The fundamental requisite for this system to successfully operate is for the RFout pixel on the MLC to receive an incident signal (which includes the same ψ_d observable at all other pixel). There may be scenarios where not all pixels on the array receive the modulated light (e.g. speckle, object edges, local opaque regions). Under these conditions measures are required to ensure that an optical signal is incident on the RFout pixel (e.g. focusing a split beam or realignment of the apparatus).

5.1.2.3 System based vibration immunity limit

The maximum change in piston phase the ultrastable system can tolerate is dependant on the range of frequencies the system is able to demodulate. A change in the pattern modulation frequency can be modelled simplest when there is a uniform OPL difference change; any change in the piston phase is equivalent to a linear change in the beat frequency (referring to equation 5.1).

An OPL difference change of one wavelength (e.g. $\Delta d_{\mathrm{OPL}} = \lambda = 633\,\mathrm{nm}$) over 1 second (e.g. a constant OPL change in one arm with velocity $v_{\mathrm{OPL}} = 633\,\mathrm{nm\,s^{-1}}$) results in modulation frequency change of 1 Hz. It follows that for any change in the OPL difference, a shift in the modulation frequency, f_{mod}, would result, such that;

$$\Delta f_{\mathrm{mod}} = \frac{v_{\mathrm{OPL}}}{\lambda} \tag{5.4}$$

The MLC will continue to produce ultrastable images given the condition that any resultant shift in the modulation frequency is within the operational bandwidth of the MLC (the camera will adapt to the changes in the modulation frequency). This model assumes a constant change in OPL and is therefore, theoretically, not limited to a maximum OPL difference. This scheme could be useful for an experiment where the subject being analysed is constantly moving away.

In another scenario, a vibration introduced into the system moves the apparatus; this movement could be periodic or random. The vibration on an object can be measured by its peak vibration displacement, d_{vib}, vibration velocity, v_{vib}, or vibration acceleration, a_{vib}, and can be converted to and from each other by integrating or differentiating the vibration function over time.

Making the assumption that a piston phase vibration introduced into the interferometer has a simple harmonic motion, the OPL would change as a sinusoidal function with a frequency, f_{vib}, where the vibration displacement, velocity and acceleration can all expressed by;

$$a_{\text{vib}} = v_{\text{vib}}(2\pi f_{\text{vib}}) = d_{\text{vib}}(4\pi {f_{\text{vib}}}^2) \tag{5.5}$$

In this model, the displacement is dependent on the vibration velocity and frequency, and there is a limit on the amount of OPL movement that can be tolerated by the ultrastable system. Assuming that the MLC is capable of demodulating light from DC to 15 MHz without error (i.e. the operation bandwidth of the MLC), in an interferometer with a 633 nm light source, the theoretical velocity immunity limit for the system would be $9.4\,\text{m}\,\text{s}^{-1}$ (referring to equation 5.4).

It is possible to translate this into a vibration acceleration and displacement limit using equation 5.5. For example, assuming a vibration frequency f_{vib} =1 Hz, the vibration acceleration and displacement limit would equal $a_{\text{vib}} = 59.0\,\text{m}\,\text{s}^{-2}$ and $d_{\text{vib}} = 1.5\,\text{m}$ respectively. In practice, the tolerable vibration velocity is much lower as it is dependent on the actual bandwidth of the MLC, the surrounding electronics and filter responses (explored further in section 5.3).

5.1.3 Ultrastable interferometer with internal vibration

The most direct way of testing the ultrastable system was by introducing a controlled vibration into the interferometer system. For an ideal test, the vibration induced would have changed the OPL of one arm uniformly (described in section 5.1.2.3), practically however, this was challenging. Basing the ultrastable system on the Mach-Zehnder interferometer described in section 4.1.2, a vibrating mirror was placed into one arm of the interferometer as illustrated in figure 5.2; a photograph of the arrangement is show in figure 5.3.

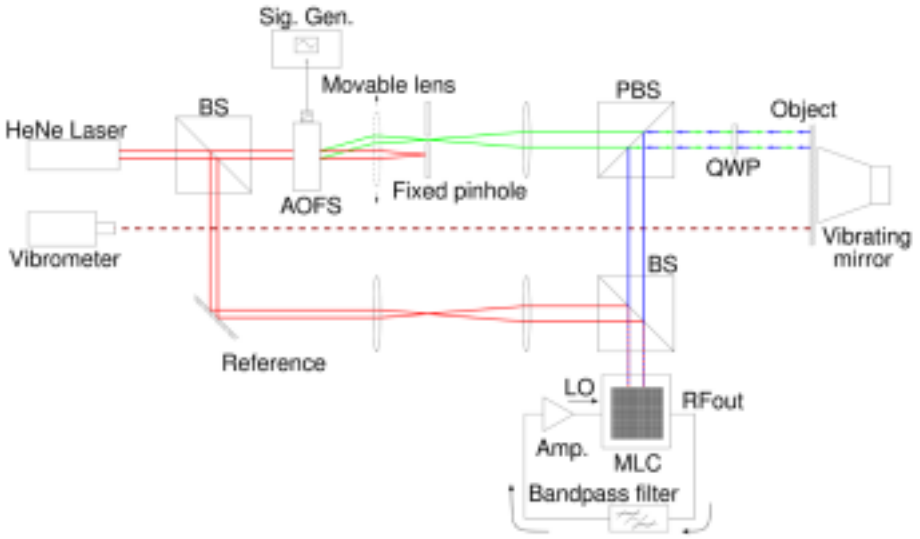

Figure 5.2: Mach-Zehnder ultrastable interferometer. The optical setup was based on the system presented in the previous chapter (figure 4.1). The object arm mirror had been replaced by a PBS, with the object beam propagating to a mirror mounted on a speaker (vibrating mirror), inducing large OPL changes in the arm. A vibrometer was aimed at the vibrating mirror to determine the vibration velocity. The local reference (LO) signal was derived from the RFout of a single pixel.

The ultrastable interferometer presented retained the modified spatial filter (from the previous setup), which allowed quick switching between homodyne and heterodyne modes (to aid alignment). A polarising beamsplitter (PBS) was placed in the object arm, replacing the mirror from the previous setup. The object beam propagated through the AOFS and spatial filter arrangement, and passed through the PBS and a quarter wave plate (QWP). The light reflected off the mirror mounted on a speaker and back through the PBS, where it continued to interfere with the reference beam. An externally generated signal (sine wave) with frequency f =15 MHz was used to drive the AOFS, however, unlike the previous arrangement, this signal was not used as the LO reference signal in the MLC. Instead, the RFout signal was fed in as the LO (as discussed in section 5.1.2) through a filter/amplifier chain; the signal was low pass filtered (<15 MHz) to remove high frequency noise induced by the MLC, amplified with a gain of 40 dB, boosting the signal for mixing, and band pass filtered (8 MHz to 15 MHz) in order to reduce the DC and low frequency content in the signal. The filter chain was employed in this ultrastable arrangement to prevent the saturation of the electronic components on the camera chip. The measured propagation (phase) delay

through this chain was negligible.

An OPL change was implemented by mounting the large object arm mirror onto a speaker, producing roughly uniform OPL changes. The speaker was driven using a separate signal generator and was capable of producing vibrations on to the mirror with frequencies from 18 Hz to 20 kHz at various amplitudes. A vibrometer (Polytec OFV-2570) was used to determine the mirror displacement, operated by targeting the device's probe beam on to the vibrating mirror.

The interferometer was switched between ultrastable mode and the standard mode by moving the local oscillator reference line from the MLC's RFout to a signal generator output, and vice versa; comparisons of the images captured using the MLC in both modes are made.

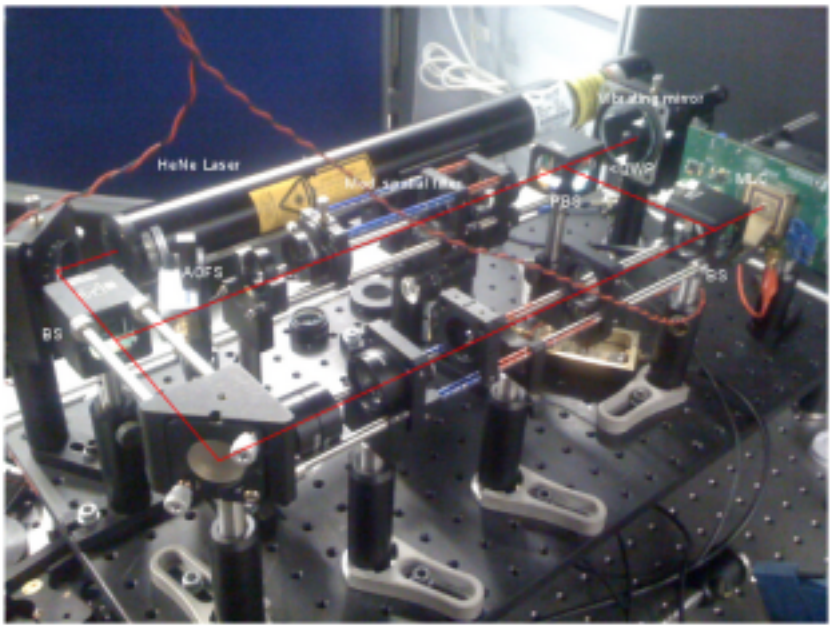

Figure 5.3: Photograph of the ultrastable Mach-Zehnder heterodyne interferometer shown in figure 5.2; precision alignment was required of the vibrating mirror to maximise the amount of uniform OPL available (misalignment would produce unstable images).

5.1.3.1 The effect of the vibrating mirror

The RFout pixel in the middle of the array outputs the raw measured light. In the experiment described, modulated light (i.e. heterodyne fringe pattern) was incident on this pixel and had a beat frequency of 15 MHz; the RFout pixel outputs

a signal with this 15 MHz component similar to an independent point detector (e.g. a photodiode). Figure 5.4(a) (bottom trace) illustrates the RFout signal after amplification/filtering (top trace shows a 15 MHz reference signal) measured using an oscilloscope (Tektronix MSO 4034).

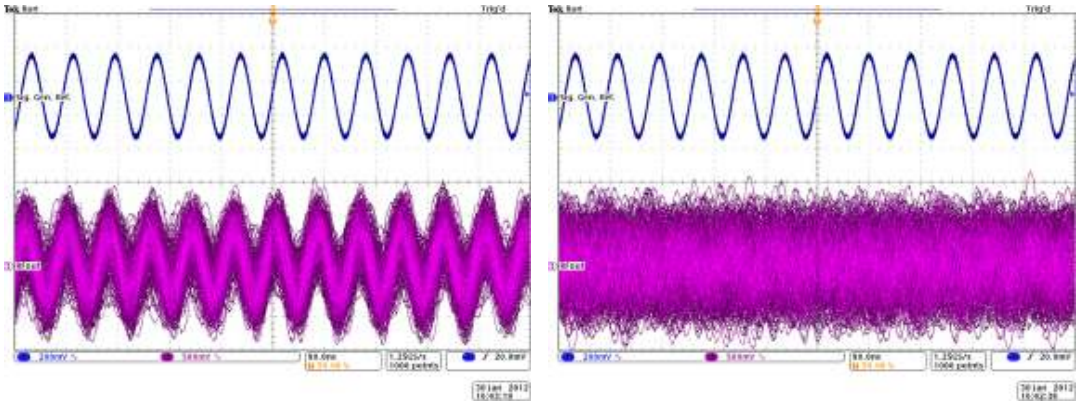

(a) **(b)**

Figure 5.4: High frequency capture of incoming signals using the oscilloscope . In both images, the top (blue) trace is of the clean (15 MHz) reference signal from the signal generator and the bottom (magenta) trace is of the signal measured from the RFout pixel. The left (a) image was taken without vibration induced and the right (b) image was taken with vibration induced on to the mirror mount.

A constant OPL shift would change the phase of the RFout signal over time (or as a shift in modulation frequency). This is observable in figure 5.4(b) (bottom trace), where a 10 Hz sine wave signal was applied to the mirror mounted speaker; the measured RFout signal has no single distinguishable frequency.

5.1.4 Ultrastable interferometer with simulated vibration

Referring to equation 5.4, a vibration introduced into a heterodyne interferometer will shift the modulation frequency; the limit of the ultrastable system's vibration immunity limit is dependant on the system's operational bandwidth (inc. filters, amplifiers and MLC). Practically, determining the vibration limit mechanically is difficult (massive piston phase vibration). Instead, the effect of vibration can be simulated experimentally by varying the optical frequency difference in a heterodyne interferometer (and therefore determine the system operational bandwidth).

The Mach-Zehnder arrangement used in the previous sections was unsuitable for varying the modulation frequency, and therefore a Michelson interferometer arrangement, illustrated in figure 5.5, was used; a photograph of the interferometer setup is shown in figure 5.7.

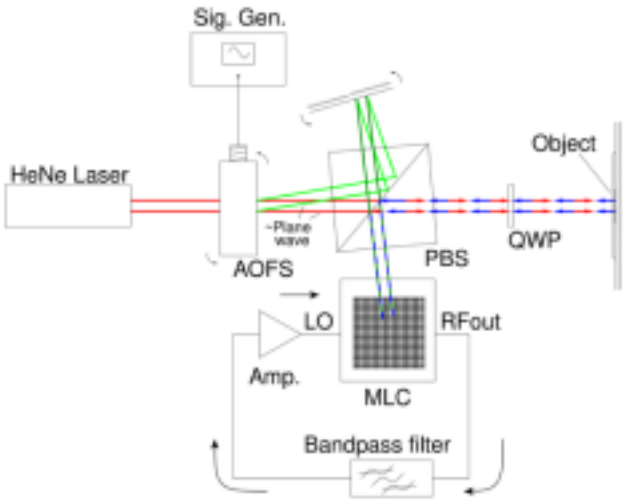

Figure 5.5: Michelson ultrastable interferometer. The AOFS (driven at various frequencies) splits the incident beam into two orders with different frequencies. They took different paths after going through a polarising beamsplitter as each order was orthogonally polarised. One beam reflected off the object, and both beams interfered when they passed through the beamsplitter the second time. As the AOFS drive frequency is varied, the diffraction angle changed; adjustments to the reference arm mirror and the AOFS were made to obtain similar fringe pattern images. The setup retained the RFout/LO feedback circuit from the Mach-Zehnder ultrastable interferometer.

The 0^{th} and 1^{st} order output from the AOFS are orthogonally polarised [120]. In the Michelson ultrastable interferometer shown, the beams were 'split', using a polarising beamsplitter (i.e. sent in different directions, as indicated). The beams are reflected off mirrors, with the object beam passing through a wave plate, and interfered at the same PBS.

The optical frequency difference (and therefore the modulation frequency) was changed by adjusting the input drive frequency of the AOFS. Changing the AOFS's drive frequency also changed the angle of diffraction of the 1^{st} order output beam. Careful realignment of the tilt angle of both the AOFS and refer-

ence mirror was required whenever the frequency was changed. This would have been difficult in the Mach-Zehnder ultrastable interferometer due to the rigidity of the spatial filter (specifically the translatable entry lens). The wavefronts of both arms were the same in this interferometer and were assumed to be roughly plane. With no object present in either arm, a uniform phase interferogram was observed by the MLC.

In contrast to the Mach-Zehnder arrangement, light intensity was retained through the optics until detection, (absence of pinhole, less light lost through light splitting), which maximised the optical signal. Averaging was no longer needed, which increased the frame rate up to the maximum 40 frames s^{-1}.

In addition to testing the system bandwidth, a surface profiling experiment was conducted. A chrome plated substrate with a chrome relief grating pattern was placed on the object arm mirror. The entire pattern was a few millimetres in width and height, with the interferometer only probing a small portion of the pattern. An image of one finger in the pattern was measured using an atomic force microscope (AFM) and is illustrated in figure 5.6.

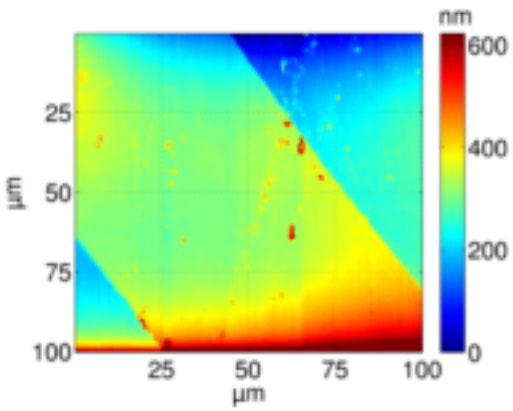

Figure 5.6: A profile image of a finger in the grating used to test the ultrastable system, captured using an AFM system. The colour indicates the height in nanometres. The height difference between the top of the finger to the substrate is between 120-160 nm.

The AFM probe area of 100 μm × 100 μm showed that the height of a finger in the grating was 140 ± 20nm. The AFM capture process took around 10 minutes.

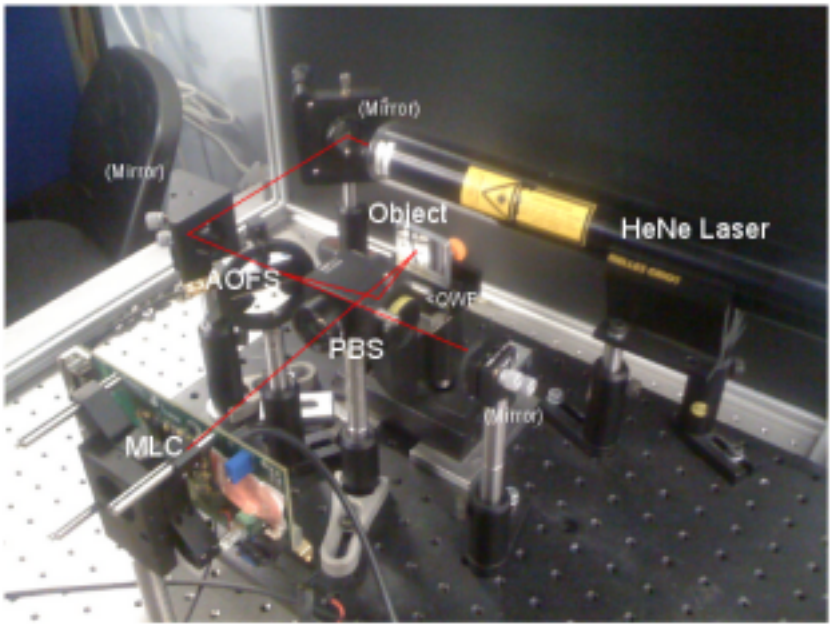

Figure 5.7: Photograph of the ultrastable Michelson heterodyne interferometer shown in figure 5.5; the AOFS was used to both split and frequency shift the incident beam. As each order emitted has a different polarisation plane, they were split effectively using the PBS. The arrangement shown in this photograph has swapped object and reference paths.

5.2 Comparison of standard and ultrastable system

The difference between the standard (figure 4.1) and ultrastable (figure 5.2) interferometer modes was the LO reference signal source, which in this experiment could be conveniently switched via a fly lead, allowing for a direct comparison between both systems (as well as produce both relative and absolute phase interferograms).

Similar to the setup presented in chapter 4, circular fringe patterns were captured (weakly spherical wave on plane wave). Each image presented in this section used 20 frame averages. A set of four images had been captured, in both the standard and ultrastable modes, under three mirror-speaker signal (i.e. piston phase vibration) conditions; with no signal, a 1 Hz square wave signal, and a 62 Hz sine wave signal. The vibration velocities of the mirror were measured with the vibrometer; the measured plot (recorded using the oscilloscope) under each scenario is illustrated in figure 5.8. It is possible to determine the vibration displacement by integrating each plot. Given the number of averages (20) and frame rate (40 fps),

each complete frame capture took 0.5 s. Each image was captured with roughly a minute time separation (no fixed time period between capture).

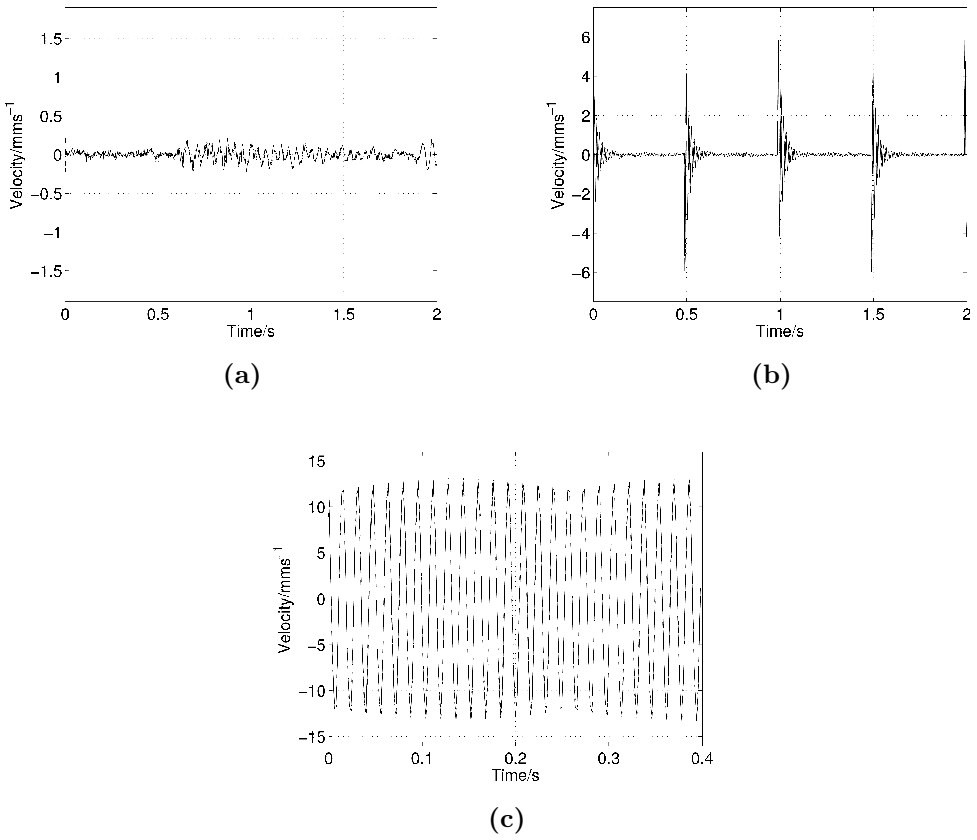

Figure 5.8: Plotted results from the vibrometer for the three piston phase vibration scenarios, (a) no signal, (b) 1 Hz square wave signal, and (c) 62 Hz sine wave signal applied to the mirror speaker, used to test the immunity of the ultrastable system. Integrating the measured velocity reveals the mirror displacement (or $\frac{1}{2}$OPL); the maximum displacement for these measurement windows equals (a) 3.9mm, (b) 7.5mm, and (c) 14.5mm from the resting position.

The first set of images were taken under the stable state (figure 5.8(a)); figures 5.9(a) to (d) show fringe pattern images captured using the standard mode setup (sig. gen. $\rightarrow$ LO), figures 5.9(e) to (h) show images captured in the ultrastable mode setup (RFout $\rightarrow$ LO).

Both the standard mode (figures 5.9(a) to (d)) and ultrastable mode (figures 5.9(e) to (h)) interferograms show the expected concentric circle fringe pattern. The 'stable' state vibrometer plot shown in figure 5.8(a), reveals the presence of

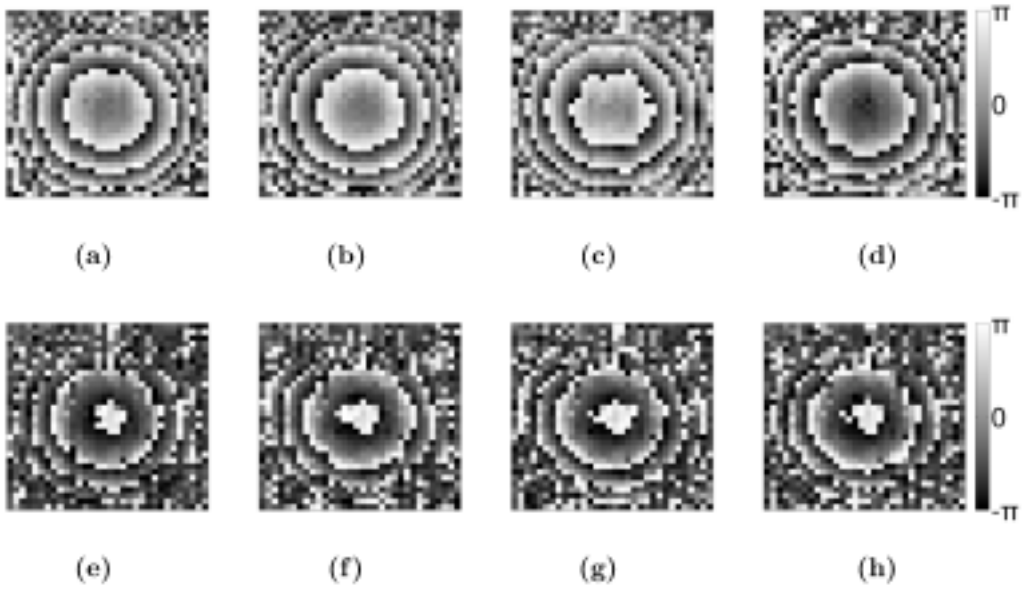

Figure 5.9: Sets of four images, separated by time, taken of a circular fringe pattern. Top images (a to d) were taken with the standard setup and the bottom images (e to h) were taken in the ultrastable configuration; the phase is represented in greyscale.

microphonics in the interferometer. This is observable in the standard mode interferogram images, which were taken over a period of approximately four minutes; a random/unknown piston phase change is present between the images (most noticeable between figure 5.9(c) and figure 5.9(d)). The ultrastable mode images, in contrast, show a relative phase interferogram; the ultrastable fringe patterns are all the same. Any piston phase variation over time is eliminated in these images. However, there is a larger presences of noise in the ultrastable mode images than in the standard mode images, this is discussed further in section 5.4.2.

The second set of images were taken with the mirror-speaker driven using a 1 Hz square wave. The interferograms captured in the standard and ultrastable interferometer modes are shown in figures 5.10(a) to (d) and figures 5.10(e) to (h) respectively.

The vibrometer plot in figure 5.8(b), shows a disturbance every 0.5 s. This is consistent with the expected vibration velocities with a 1 Hz square wave applied to the mirror speaker; a peak vibration velocity of $\sim$4 mm s^{-1} was measured. Due to the sudden changes in the OPL, the standard interferometer mode interferograms, shown in figures 5.10(a) to (d), appear distorted. Within the time period

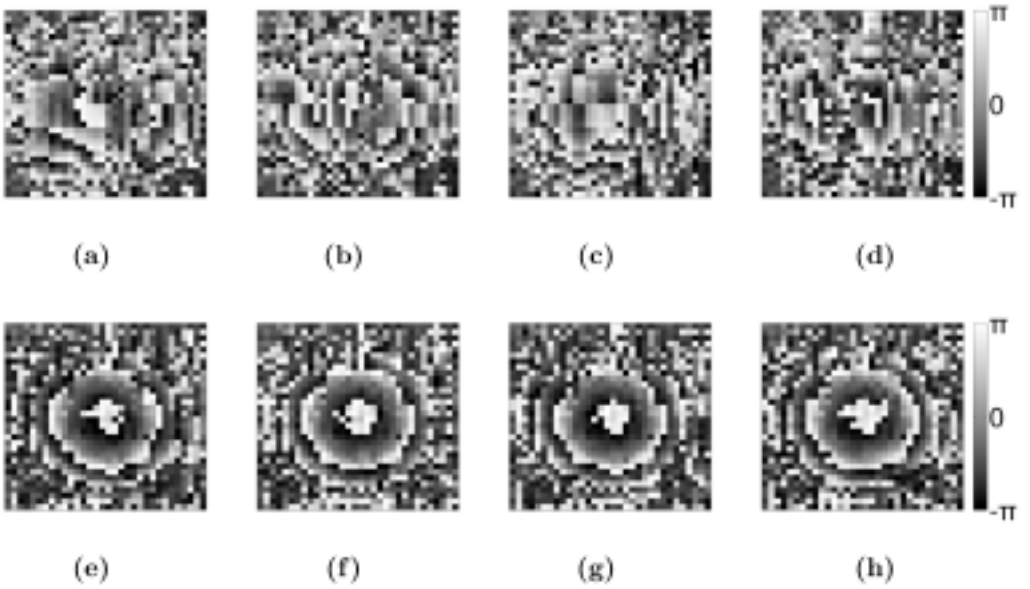

Figure 5.10: Sets of four fringe pattern images taken with a 1 Hz square wave induced on the object arm mirror; top images (a to d) in the standard mode and bottom images (e to h) in the ultrastable mode.

in which one image was captured, including averaging (0.5 s), the mirror was disturbed (caused by the square wave); this induced a severe distortion to interferogram. The ultrastable images, however, show no distortion in the patterns. The interferograms in figures 5.9(e) to (h) (no vibration) and figures 5.10(e) to (h) are almost identical (with the exception of noise).

A third set of images were taken with the speaker driven at a larger amplitude and at a higher frequency; a 62 Hz sine wave was used to drive the speaker. The standard and ultrastable interferometer mode images are shown in figures 5.11(a) to (d) and figures 5.11(e) to (h) respectively. The drive frequency of 62 Hz was chosen, as the maximum mirror displacement was achieved at this frequency (referring to the speaker response).

Firstly, the vibrometer plot in figure 5.8(c) shows a sinusoidal movement of the object mirror at 62 Hz with a total peak vibration velocity of $\sim$26 mm s^{-1}. Using the formula expressed in equation 5.5, this equates to a peak mirror displacement of $\sim$66 μm (around 105 wavelengths). A rate of change in the OPL of this magnitude is beyond the immunity range for the standard mode setup (discussed in section 1.7.5), evident by interferograms shown in figures 5.11(a) to (d), where no discernible fringe pattern is observable. This is again in contrast with the ultra-

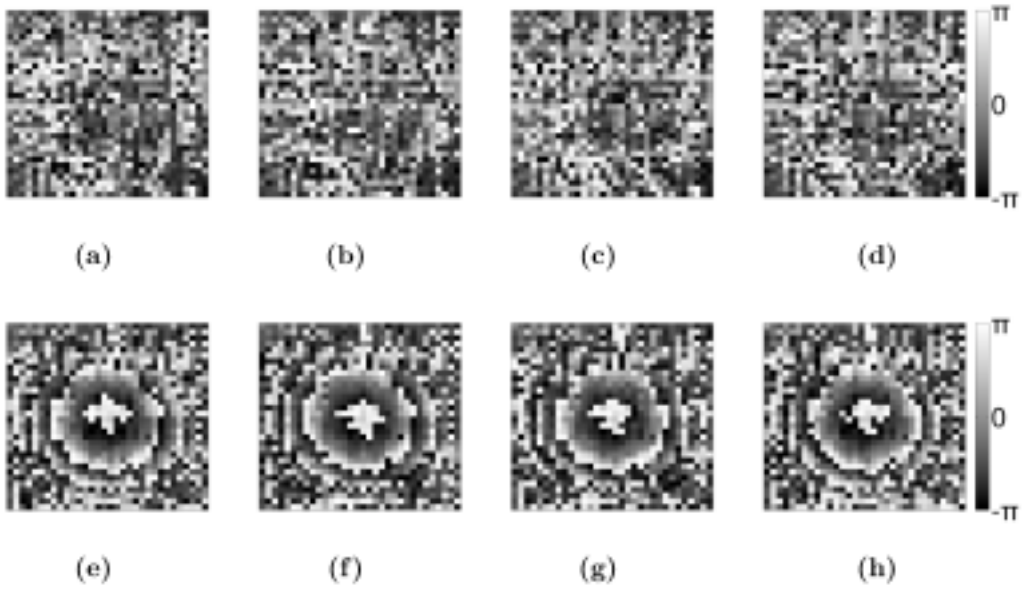

Figure 5.11: Sets of fringe pattern images taken with a 62 Hz sine wave induced on the object arm mirror; top images (a to d) with the standard setup and the bottom images (e to h) in the ultrastable configuration.

stable mode images, which are identical to the two previous vibration condition interferograms (figures 5.9(e) to (h) and figures 5.10(e) to (h)), which shows that the system was unaffected by the induced vibrations.

Fringe patterns were observable until the object mirror vibration velocity measurement exceeded 85 mm s^{-1}, above which, the fringe patterns were progressively lost; at 62 Hz, this velocity correspond to a sinusoidal motion with a displacement of 0.22 mm. In terms vibration immunity this can be considered large, but it is considerably lower than the theoretical maximum limit of the system (discussed in section 5.1.2.3). It was deduced that at large displacements, the motion of the mirror was not purely translational, i.e. no longer piston phase vibration, and as such, the ultrastable system was no longer immune to the vibration. A variety of different drivers were tried, all of which produced similar results at different frequencies and amplitudes.

5.3 Characterisation of object using the ultrastable system

The aim of this experiment was to simulate the effect of a changing OPL distance. This was achieved by adjusting the beat frequency of a heterodyne fringe pattern; the operating bandwidth of the system determines the vibration immunity limit (section 5.1.2.3).

The modified Michelson interferometer (figure 5.7) was used to capture the surface profile of a chrome grating (figure 5.6). An initial phase image (control image) was captured using a non-grated section of the substrate and compared with all subsequent pattern images. The AOFS drive frequency was swept until the phase image of the grating fingers deteriorated. Figure 5.12 illustrates the interferograms captured of the fingers in the grating pattern at various drive frequencies.

The interferograms show the same grating configuration in all images; this includes both the shape and phase (represented by the colour of the peaks and troughs). A phase measurement of 2π signifies a height range in the object of 316.5 nm. The height of each finger (relative to the substrate) is comparable with the AFM measurement (figure 5.6) of the grating, where the height for the AFM = 120-160 nm and MLC = 150-175 nm.

There is a significant noise presence in the images at both ends of the frequency range, due to the diminishing RFout signal. In addition to the filters used in the RFout feedback chain, in this arrangement the upper modulation frequency limit was determined by the MLC's frequency response and the lower frequency limit was determined by the AOFS. Outside this band range, either the optical or electronic signal was diminished (the system produces a phase image where the pattern was indistinguishable from noise). The images shown in figures 5.12(a) and (d) still display the grating pattern, and as such, a conservative estimate for this system's operational band range is between 11.2 MHz and 16.0 MHz ($\sim$5 MHz bandwidth) with no averaging. Using equation 5.4, this operation bandwidth corresponds to an object velocity tolerance of $\sim 3.1\,\mathrm{m\,s^{-1}}$. This is equivalent to a vibration with a sinusoidal displacement of $\sim$0.5 mm at 1 kHz, or $\sim$8 mm at 62 Hz. This is significantly larger than the limit determined by the vibrating mirror ex-

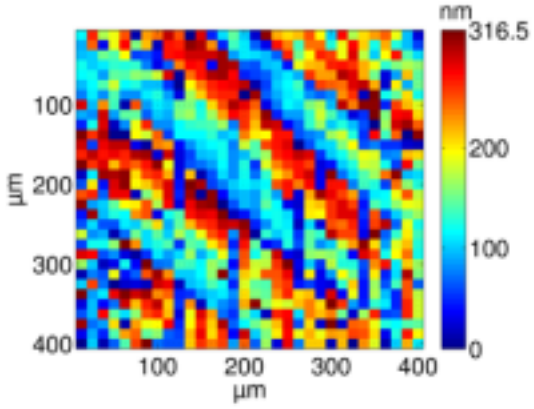

(a) Measured depth, Mod freq. = 11.2 MHz

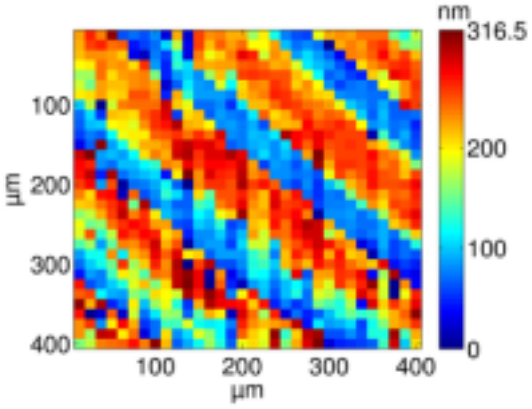

(b) Measured depth, Mod freq. = 12.9 MHz

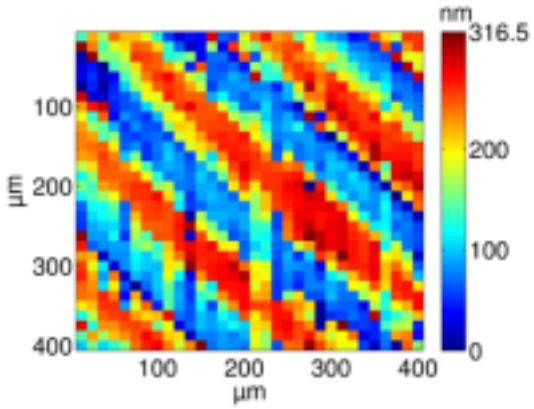

(c) Measured depth, Mod freq. = 15.0 MHz

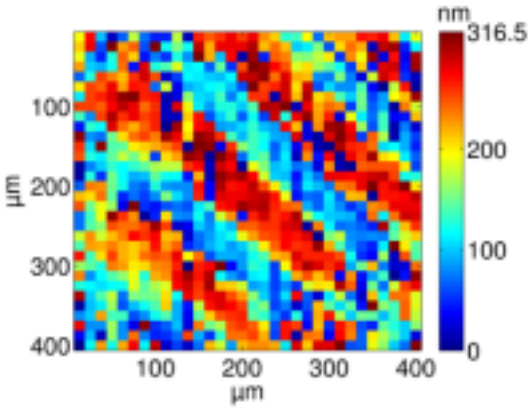

(d) Measured depth, Mod freq. = 16.0 MHz

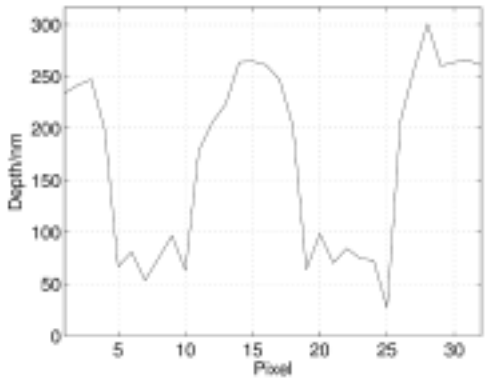

(e) 1D profile of grating pattern

Figure 5.12: Ultrastable grating interferogram images captured using (a) 11.2 MHz, (b) 12.9 MHz, (c) 15 MHz and (d) 16 MHz as the modulation frequency. The colour of the fingers indicate the surface depth, measured to be about 150-175 nm. The extreme upper (a) and lower (d) modulation limit can be increased further if averaging was introduced. A 1D surface profile plot using this setup (line x=15 at f=15 MHz) (e) of the grating pattern is shown for reference.

periment.

5.4 Ultrastable system discussion

5.4.1 System summary

The aim of the ultrastable system presented in this chapter was to facilitate the capture of modulated fringe patterns in the presence of large OPL changes. The ultrastable system does this by using the beat signal measured at a single pixel (RFout) to mix with the detected signal at all other pixels. Given the condition that any OPL change seen on one arm of the interferometer was uniform, the generated fringe pattern would experience a piston phase change. As the RFout signal was mixed with the detected signal at all other pixels, the piston phase shift observed in both signals cancels out, leaving only the position dependant phase (outputting a relative interferogram rather than an absolute interferogram). The limit of the ultrastable system's vibration immunity (discussed further in section 5.4.3) is related to the range in beat frequency the system was able to demodulate (i.e. operational bandwidth) and the wavelength of light, as described by equation 5.5.

The ultrastable system achieves vibration immunity without the need of external signals or post capture processing; the same read and addressing routine was used for both the standard and ultrastable mode system. Additionally, as the local reference (LO) input no longer required an external signal generator, there was a reduction in the number of inputs (and components) in this system.

In practice, piston phase is often observed when vibrations act on a probe object independent to the rest of the interferometer. The first experiment described in this chapter (section 5.1.3) was designed to emulate this occurrence by using a mirror-speaker mount. This ultrastable system test was restricted, as at high amplitudes, the OPL change induced by the vibrating mirror was no longer uniform (not piston phase). To this end, another experiment was conducted (section 5.1.4) to simulate the process of a probe object moving at different velocities by adjusting the fringe pattern modulation frequency (i.e. varying the AOFS drive frequency to determine the bandwidth of the system).

Interferometers are capable of making sub-wavelength OPL measurements, however the slightest vibration can have a major effect on the image captured if there are no techniques used to compensate. Under typical conditions within the laboratory, small amounts of vibrations were induced on the apparatus (figure 5.8(a)). The OPL change was seen as phase offsets in the interferograms over time; this was observable in the standard mode images shown in figures 5.9(a) to (d). In this standard mode setup, the system's ability to compensate for piston phase change was dependant on the frame capture rate (discussed in section 1.7.5). Increasing the vibration amplitude by a small amount was seen to severely distort the interferograms, seen in figures 5.10(a) to (d), and increasing the vibration by a large amount destroyed the interferogram entirely, seen in figures 5.11(a) to (d); vibrations influencing the standard interferometer mode setup could severely limit the usefulness of a system.

The ultrastable system was immune to piston phase vibrations, all images captured in the vibrating mirror experiment (figures 5.9(e) to (h), figures 5.10(e) to (h) and figures 5.11(e) to (h)) display an unchanging fringe pattern, independent of the time the image was captured or the vibration induced (up to a limit).

5.4.2 Additional pixel noise

In section 3.1.3.3, an analysis of the error through the MLC system was described; the assumption was made that in the MLC mixer stage, the LO input contained no noise (i.e. a clean reference signal). This assumption was adequate for the standard interferometer mode setup explored in chapter 4, and for the images shown in figure 5.9(a)-(c), figure 5.10(a)-(c), and figure 5.11(a)-(c). If the additional assumption is made that the mixer adds negligible noise to its output, the mixer input SNR (SNR_{Sig}) would equal the mixer output SNR (SNR_{Out}).

However, for the ultrastable arrangement described in this chapter, the fed-back RFout signal used as the LO input does contain noise. This is apparent in the oscilloscope trace of the RFout signal shown in figure 5.4(a). Referring to equation 3.7, the presence of noise on the LO input increases the error at the output of the mixer (assuming that the measured and LO input noise is uncorrelated). The equation can be rearranged to show the effect this has on the mixer's output SNR (SNR_{Out});

$$\begin{aligned}
\Delta \mathrm{Mix_{out}} &= \sqrt{\mathrm{LO}^2.\Delta\mathrm{Sig}^2 + \mathrm{Sig}^2.\Delta\mathrm{LO}^2} \\
\frac{\Delta \mathrm{Mix_{out}}^2}{\mathrm{Mix_{out}}^2} &= \frac{\mathrm{LO}^2.\Delta\mathrm{Sig}^2 + \mathrm{Sig}^2.\Delta\mathrm{LO}^2}{\mathrm{LO}^2.\mathrm{Sig}^2} \\
&= \frac{\Delta\mathrm{Sig}^2}{\mathrm{Sig}^2} + \frac{\Delta\mathrm{LO}^2}{\mathrm{LO}^2} \\
\frac{1}{\mathrm{SNR_{Out}}} &= \frac{1}{\mathrm{SNR_{Sig}}} + \frac{1}{\mathrm{SNR_{LO}}} \qquad (5.6)
\end{aligned}$$

where $\mathrm{SNR_{LO}}$ is the SNR of the LO input. The addition of the LO noise into the mixer operation increases the MLC output noise (decreasing the SNR).

The schematic in figure 5.13 shows the noise on the LO contributes to the noise at the output. This can be compared with the noiseless LO case described in figure 3.7. The output of the mixer contains the noise components from both the measured input and LO input, which is low pass filtered as depicted in figure 5.13(c).

As with the standard setup, this is analogous to applying a band pass filter at the modulation frequency F_{mod}, as shown in figure 5.13(d).

The standard mode (figure 4.1) and ultrastable mode (figure 5.2) interferometer setup operate under similar circumstances (e.g. AD/DC light intensity, modulation frequency, etc.). Therefore, $\mathrm{SNR_{Sig}}$ value from section 3.1.3.3 can be transferred over to this model. The RFout signal and noise have been measured (after passing through the filter/amplifier chain); the RFout signal amplitude was measured to be 1.4 V by applying a large degree of averages, and the noise on the RFout was determined to be $2.4\,\mathrm{mV_{rms}}$ by capturing a 'dark' signal and using a digital filter to simulate the MLC output filter.

Using equation 5.6 and equation 3.7, the phase uncertainty was determined to be $\phi_{\mathrm{ultrastable}} = 0.18$ radians ($\sim 10°$).

The output for this prototype sensor does contain significant electronic noise, which limits the practical applicability of this particular system. The noise performance is below some of the detection schemes described in section 2.3, however,

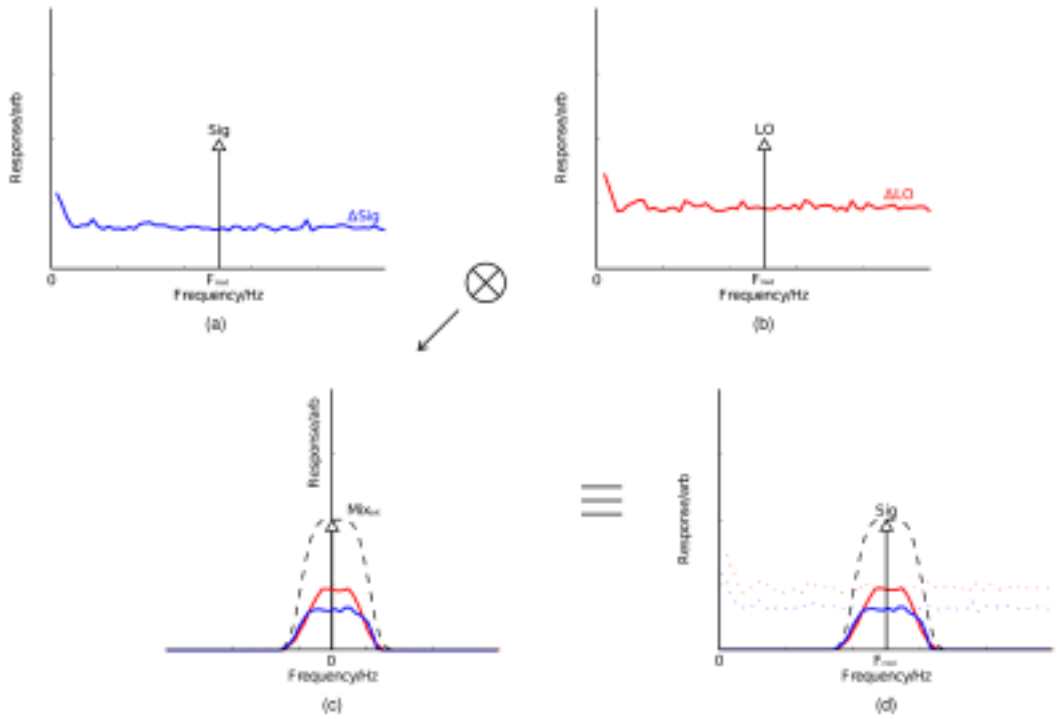

Figure 5.13: Schematic of frequency spectra depicting the inputs and output of the MLC mixer stage under the ultrastable configuration. Both the measured signal input (a) and the LO signal input (b) contains random noise. Similar to the widefield setup (figure 3.7), the output of the mixer (c) will be a down-mixed version of measure signal, but with additional noise due to the RFout noise, as shown in equation 5.6. The signal is filtered.

this experiment provides a proof of concept for a system that can capture widefield ultrastable interferograms in real time.

5.4.3 Vibration immunity context

If an object is moving uniformly (e.g. along the optical axis), it is possible to capture a fringe pattern off the object using the ultrastable system if the object velocity is within the system's immunity limit. The immunity limit is derived from the system's operation bandwidth; probing an object moving with velocity v_{OPL} shifts the modulation frequency of the generated fringe pattern by the amount expressed in equation 5.4. Assuming an MLC operation bandwidth of 15 MHz, theoretically, a relative fringe pattern could be captured off an object moving at a peak velocity of $9.4\,\mathrm{m\,s^{-1}}$ ($\lambda = 633\,\mathrm{nm}$). This model can be extended

to vibrations, where an object moves with a function (e.g. sinusoidally) along one axis. The ultrastable system is able to capture interferograms given this type of movement, but is limited by the amount displacement and frequency.

To practically determine vibration velocity limits, two experiments were conducted. Fringe patterns were captured in the vibrating mirror experiment with the mirror moving with a peak vibration velocity of $v_{\text{vib}} = 85.0\,\text{mm}\,\text{s}^{-1}$ (measured using a vibrometer), above which it was determined that the mirror was no longer vibrating uniformly. As the system's operational bandwidth is related to the vibration velocity (equation 5.4), an experiment was conducted to determine the bandwidth (simulating an object moving at different velocities); relative phase images of a chrome grating were obtainable between 11.2 MHz and 16.0 MHz, which gives a bandwidth of 5 MHz, and velocity limit of $v_{\text{vib}} = 3.1\,\text{m}\,\text{s}^{-1}$. The bandwidth in this experiment was limited by the MLC's upper operational frequency threshold as well as the AOFS's lower frequency threshold.

Given these different vibration velocity limits (measured, simulated and theoretical), v_{vib}, table 5.1 shows the peak vibration displacement, d_{vib}, at various vibration frequencies, f_{vib} (assuming purely sinusoidal movement, using equation 5.5).

	$\mathbf{v}_{\text{vib}}$	**Peak** $\mathbf{d}_{\text{vib}}$ **@** $\mathbf{f}_{\text{vib}} = \mathbf{0.5\,Hz}$	**Peak** $\mathbf{d}_{\text{vib}}$ **@** $\mathbf{f}_{\text{vib}} = \mathbf{10\,Hz}$	**Peak** $\mathbf{d}_{\text{vib}}$ **@** $\mathbf{f}_{\text{vib}} = \mathbf{62\,Hz}$	**Peak** $\mathbf{d}_{\text{vib}}$ **@** $\mathbf{f}_{\text{vib}} = \mathbf{1\,kHz}$
Measured	$85.0\,\text{mm}\,\text{s}^{-1}$	27 mm	1.3 mm	220 μm	14 μm
Simulated	$3.1\,\text{m}\,\text{s}^{-1}$	1 m	50 mm	8 mm	0.5 mm
Theoretical	$9.4\,\text{m}\,\text{s}^{-1}$	3 m	150 mm	24 mm	1.5 mm

Table 5.1: Table summarising the vibration immunity limits of the ultrastable interferometer. The right hand columns indicate the amplitude of sinusoidal vibration at various vibration frequencies.

To put these object displacement immunity limits into context, they can be compared with real world environmental vibrations. A stand-alone building experiences vibrations of $0.1\,\text{m}\,\text{s}^{-2}$ due to environmental effects such as traffic and up to $1.0\,\text{m}\,\text{s}^{-2}$ of shock vibration, both situations have vibration frequencies below 10 Hz [130]. Other examples include a car travelling at 30 kph and 60 kph, and a train experiencing vibration acceleration of $0.87\,\text{m}\,\text{s}^{-2}$, $0.96\,\text{m}\,\text{s}^{-2}$ [131], and

$0.32\,\mathrm{m\,s^{-2}}$ [132] respectively, again with vibration frequencies below 10 Hz.

Table 5.2 shows the peak change in displacement at two vibration frequency (0.5 Hz and 10 Hz, i.e. within the frequency range of the environmental vibrations). The vibration displacement increases as the frequency decreases. Assuming that the vibration experienced in these examples act on an object (e.g. such as the chrome grating shown in figure 5.5) along one axis, the ultrastable system (given the theoretical and simulated immunity limits) would be able to capture stable interferograms.

	$\mathbf{a_{vib}}$	**Peak** $\mathbf{d_{vib}}$ **@** $\mathbf{f_{vib} = 0.5\,Hz}$	**Peak** $\mathbf{d_{vib}}$ **@** $\mathbf{f_{vib} = 10\,Hz}$
Building background	$0.1\,\mathrm{m\,s^{-2}}$	10.1 mm	25.3 μm
Building shock	$1.0\,\mathrm{m\,s^{-2}}$	101.3 mm	253.3 μm
Car 30 kph	$0.87\,\mathrm{m\,s^{-2}}$	88.1 mm	220.3 μm
Car 60 kph	$0.96\,\mathrm{m\,s^{-2}}$	97.2 mm	243.2 μm
Train	$0.32\,\mathrm{m\,s^{-2}}$	32.4 mm	81.0 μm

Table 5.2: Table showing the measured vibration accelerations and the peak vibration displacements (given that the vibration frequency is 0.5 Hz and 10 Hz) of various environmental conditions.

Other examples of vibrations include the largest set of ISO2631 guidelines, which state that the maximum vibration displacement experienced should be 6.4 μm and 12.7 μm (at 10 Hz) for an office and a workshop respectively [133], which is within the vibration immunity limits.

The ultrastable system could also be used under a degree of seismic activity. Large seismic shocks from earthquakes have peak amplitudes at 0.55 Hz [134, 135] and can reach amplitudes of $\sim$1 m. At 0.55 Hz, the ultrastable system would be able to cope with up to $32.4\,\mathrm{m\,s^{-2}}$ of sinusoidal ground vibration, which is beyond any acceleration that any real recorded earthquake has caused (beyond a Richter scale of 10 and the Shindo rating of 7 [136]).

The vibration immunity feature of this ultrastable system can be compared against other widefield interferometer systems. One method involves using a high speed acquisition technique for fringe pattern capture [137]. In such a system, the phase uncertainty due to an introduced vibration would depend on the frame

rate of the camera (which would be in addition to the random electronic/optical noise of the system). For a system experiencing a vibration/movement with a peak velocity, v_{peak}, the minimum frame rate required, fr_{min}, would depend on the maximum phase error allowable (due to vibration), $\Delta\phi_{\text{req}}$, such that;

$$\text{fr}_{\text{min}} = \frac{2\pi v_{\text{peak}}}{\Delta\phi_{\text{req}}\lambda} \tag{5.7}$$

where the phase error is a value in radians, and λ is the wavelength of light used in the interferometer. If compared with the ultrastable system (phase error of $\sim$0.18 radians, using light where $\lambda = 633\,\text{nm}$), a limited vibration velocity of around $66\,\mu\text{m}\,\text{s}^{-1}$ (as shown in section 5.2) would require a camera frame rate of 3600 fps. If a vibration with velocity $3.0\,\text{m}\,\text{s}^{-1}$ was induced in to the system, a frame rate of 165 Mfps would be required (a widefield detection system with a frame rate in this region would be prohibitively expensive and sizeable). However, the major advantage of using a high speed acquisition system is its tolerance of all types of vibration and movement, not just piston phase vibration. Therefore, for the relatively small vibrations observed in some test areas (microphonics), it is often the preferred solution.

Another solution is to use a common-path interferometer. Due to the common-path arrangement, it is immune to piston phase vibration; as both the reference and object beams travel along similar paths, common temporally varying phase shifts cancel out optically when they interfere. However, in certain scenarios it is not always convenient to construct a common path interferometer.

The ultrastable system presented in this chapter is a solution in between the two systems described; it offers a high degree of piston phase vibration immunity (by using electronic self-referencing) with a practical frame rate, and allows for some flexibility in the interferometer arrangement. For example, the separate reference beam could be used to increase a signal's amplitude optically (if the object beam becomes heavily attenuated).

Chapter 6

Two-laser widefield heterodyne interferometer

The work presented in this chapter is an extension of the ultrastable system, where it is used to perform multiple source interferometry. The challenges in producing two-laser interferograms are explored. To produce the light used in two laser interferometry, stabilised lasers were constructed; these are analysed. The images captured are shown and the advantages of the interferometer are explored.

6.1 Two-laser interferometry outline

6.1.1 Two-laser interferometer brief

The ability to observe interference fringe patterns is predicated on the phase function of the interfering light as well as the detection method used. If the phase relationship between two interfering beams is definable, a measurable fringe pattern can be captured by using the knowledge of the phase relationship. In an amplitude splitting interferometer (e.g. Michelson/Mach-Zehnder interferometers), a definite phase relationship is obtained by splitting a single source to generate the two interfering beams (even if one/both are frequency shifted). The phase relationship between the two beams can be considered predictable as long as the optical path length difference is less than the coherence length of the source.

In contrast to a single split beam, the phase relationship between the light from two separate sources are prone to fluctuate randomly as their phase functions are independent of each other and therefore can be considered incoherent over a

large period of time. This can be viewed as a variation in the source emission frequency and makes continuous capture of fringe patterns difficult.

The signal feedback arrangement (RFout → LO) used in the ultrastable interferometer system (described in chapter 5) allowed for a major relaxation in the temporal coherence requirement for the light source. The unknown optical frequency difference between the interfering beams (i.e. phase relationship) was detected using an RFout pixel on the MLC. This signal was used to demodulate the incident fringe pattern captured at other pixels. Given the condition that the beat frequency was within the operation bandwidth of the MLC, continuous fringe patterns could be captured, even as the beat frequency shifted.

The system could have also been used to capture the patterns from an amplitude splitting interferometer where the OPL difference between each arm was larger than the coherence length of the split source.

6.1.2 Adapting the ultrastable system for two-laser interferometry

The continuous capture of interferograms, produced by interfering two independent lasers, can be modelled using a similar approach to the ultrastable system (section 5.1.2.1). The intensity of the heterodyne interference pattern can be described using the equation B.1, which consists of an AC component defined by an unknown angle function, $\theta(t)$. As described in Appendix B, the instantaneous beat frequency, $\omega_i(t)$, for the interference pattern is equal to the differential of the unknown angle. As a result, the intensity pattern can be described by equation B.4; the described model is analogous to frequency modulation in analogue communication systems [33].

The ultrastable system showed that temporal phase shifts due to environmental vibration could be eliminated. In this two laser system, the same feedback methodology was applied to capture stable and continuous two laser interferograms. Both the RFout signal and the signal detected at all other pixels contain an AC component with the same unknown instantaneous frequency, $\omega_i(t)$. After the mixing process and filtering, the unknown frequency component cancels out, leaving the I and Q outputs; the relative phase of the incident pattern can be

determined by using the inverse tangent function expressed in equation 5.2. This system can eliminate the effects of both frequency shifts and piston phase shifts from interferograms. However, similar to the ultrastable configuration, the system is limited by the optical frequency difference (beat) between the two separate lasers being within the operational bandwidth of the MLC and the supporting electronics. If the independent light sources are kept stable (within a few MHz), two lasers fringe patterns could be captured continuously.

6.1.3 Construction of stabilised HeNe lasers

As discussed in section 3.2.1, the optical frequency emitted by a gas laser (e.g. of a single mode) is linked to its cavity length. This length can change due to the environmental changes, and in particular the temperature of the laser and surroundings. Stabilised lasers were constructed in order to maintain a steady output frequency with minimal frequency drift. It would have been possible to purchase a commercially available stabilised laser with low frequency drift (e.g. ± 5 MHz over 24 hours, iodine stabilised HeNe laser [138]). However, stabilised lasers were built in lab at a fraction of the cost. In addition, some degree of frequency tuning was required (to set the beat frequency to within the system's operation range) and commercially available stabilised lasers with this feature had additional costs.

The laser emission frequency varies as the heat generated from within the tube causes it to expand until a steady equilibrium is attained with the environmental temperature. If the environmental temperature fluctuates, so too does the emission frequency, causing frequency instability. Balhorn et al. proposed a technique to use optical and electrical feedback to maintain a fixed cavity length [139]. This method used a two mode HeNe laser, where the gas tube consisted of two silvered mirrors, allowing light to exit both ends of the tube; the main exit and waste exit. The main exit operated as normal (e.g. the emitted light from this side of the laser was used for the interferometry experiment), however the beam observed at the waste exit was used for feedback.

The importance of using a HeNe laser is that each alternative mode is orthogonally polarised. Experiments conducted by Tang et al. indicated that for a HeNe gas laser, maximum optical amplification occurs when a set of two longitudinal modes have polarisation that was linear and perpendicular with respect to each

other [110]. As the two modes are orthogonally polarised, they can be split using a polarising beamsplitter (PBS). Referring to the laser gain-band plot shown in figure 3.10 and frequency mode separation equation expressed in equation 3.9, as the laser cavity length changes, the frequency of the emitted modes also changes. Due to the laser gain band, the intensity of each mode also changes (depending on its position inside the band).

The HeNe lasers constructed for use in the experiment were made in-lab using cheap readily available parts. They are based on an updated design of one presented by Bennett et al. [140], which itself was based on the stabilisation technique described by Balhorn at al. [139]. The laser tubes and instructions on how to build the lasers were provided by Sam Goldwasser [108]. Figure 6.1 shows a schematic of the feedback stabilisation circuitry used in the laser.

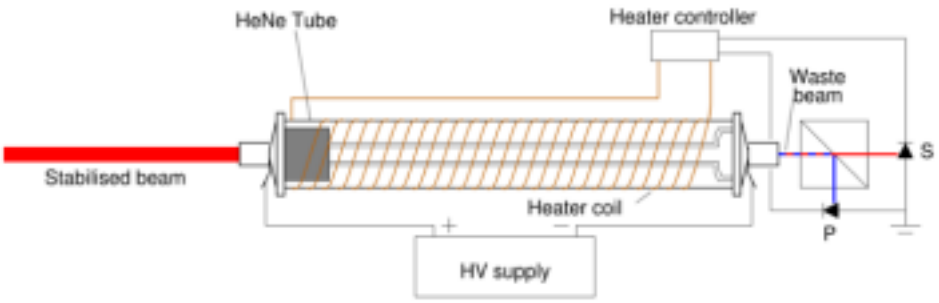

Figure 6.1: Stabilised laser system. Each HeNe laser outputs two longitudinal modes which are orthogonally polarised. As the tubes expand and contract (due to the temperature), the optical frequency and intensity of these modes shift. The intensities are detected at the waste exit, compared, and the current into the tube coiling changes to maintain an adaptive tube length. This feedback system was used to maintain a constant frequency for each mode.

The intensities of the two laser modes (separated at the waste exit using the PBS) were measured using photodiodes. These signals were fed into a comparator circuit to generate an error/difference signal. The changes in the mode intensities, and therefore emission frequencies, generated a shift in error signal. Balhorn et al. used this error signal to vary the discharge current going into the laser itself [139]. This idea was later adapted by Bennett et al. [140] (simplified by Gordon and Jacobs [141]) which used the error signal to drive a current through a coil wound round the laser tube. The current heats (expands) the tube or allows the tube to cool (contract) as required, which increased or decreased the cavity length re-

spectively. The comparator circuit also contained a bias offset input, which was used to apply/remove current to the heater to shift the laser modes up or down the gain curve. This allowed the user to tune the laser output frequency. The comparator circuit used is detailed further in Appendix C.

The lasers built have a laser gain bandwidth of ∼650 MHz centred at 632.8 nm. A trait of keeping a laser frequency stabilised is intensity variations while frequency stability is being achieved. The measured output intensity of each laser varied between ∼0.4 mW and ∼1.2 mW.

6.1.4 Two-laser interferometer arrangement

The optical setup required to capture widefield heterodyne interferograms produced by two lasers is much less complex than most other interferometer designs. An interference pattern can be generated by simply imposing one laser's beam onto the other (and captured by the MLC). The interferometer setup used in this chapter used a beamsplitter, polarisers, a mirror and collimating lenses to enable more convenient imaging; a schematic of the setup is illustrated in figure 6.2, along with a photograph of the setup, shown in figure 6.3.

The external photodiode in the setup has a much larger frequency response (around 150 MHz) when compared with the MLC, and was used to observe the beat frequency as the lasers stabilised. Once the lasers were in a relatively stable state, a bias was applied to the comparator circuit to shift the beat frequency into the operational region of the MLC.

Measuring the absolute emission spectrum of each laser would be difficult and resource intensive, however, measuring the beat frequency generated by interfering the two beams gives a good indication of the lasers stability with respect to each other. After the initial warm up, the beat frequency stability was measured to be (at the very least) ∼1 MHz over 10 minutes and ∼3 MHz over 30 minutes. Measurements to acquire these figures are explored in Appendix D.

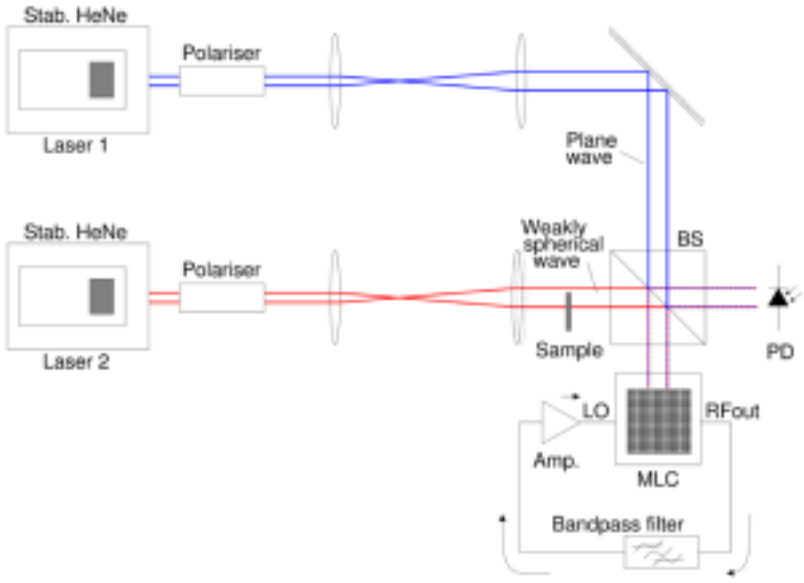

Figure 6.2: The two laser interferometer system. Each laser was completely independent, with separate power supply units, heated using individual tube coiling and were aligned separately. Polarisers were used to select a mode of the laser for interference. The photodiode was used to keep track of the beat frequency. The MLC detector was kept in the ultrastable configuration as described in section 5.1.3. The lasers were separated by ~35 cm.

6.2 Captured two laser interferograms

6.2.1 Fringe patterns in stable laser conditions

In this interferometer setup, the optics were aligned to produce roughly horizontal fringes (instead of circular fringes shown in previous chapters). Once the two lasers had become relatively stable in their environment, the MLC was used to capture the interference fringe patterns; three phase images were captured over time, illustrated in figures 6.4(a), (b) and (c). At the same time as the image capture, a snapshot of the RFout waveform, measured using an oscilloscope (data transferred to a PC), was also captured, illustrated in figures 6.4(d), (e) and (f) under their respective phase images. An FFT of the RFout waveforms was conducted to show the frequency components present in the captured waveform, and is illustrated in figures 6.4(g), (h) and (i), under their respective waveforms.

As expected, the FFT plots show that there was a modulation frequency shift over time. Even with this change in beat frequency, the same fringe pattern had been observed using the MLC (pattern was relative to the RFout pixel). As

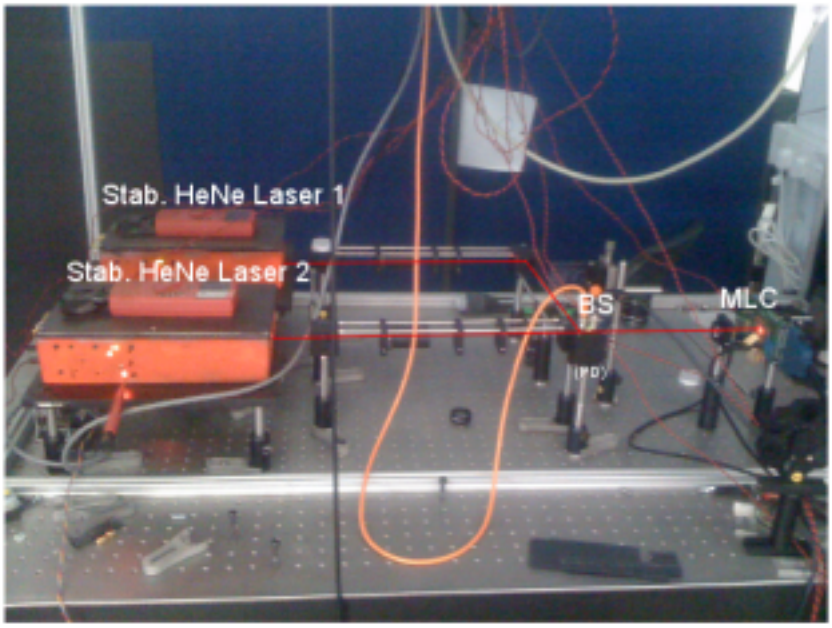

Figure 6.3: Photograph of the two-laser heterodyne interferometer shown in figure 6.2; the photograph shows no interaction between the two lasers, and the only input into each laser is the power supply (12v and 24v).

long as the lasers were kept stable enough to generate a beat frequency within the operating range of the MLC, two laser interferograms could be continuously captured. More importantly, undistorted images were captured even as the beat frequency varied during the capture process (i.e. pixel-by-pixel). These images were captured with no averaging and took the same time to read and process as with the previous interferometer setup (25 ms read time, 0.4 s processing time).

6.2.2 Fringe patterns in shifting laser conditions

Much like the ultrastable experiment conducted to explore the upper operational frequency limit of the MLC/feedback arrangement (section 5.3), this two laser setup was used to explore the effects at the lower operational frequency limits (as there was no lower optical limit due to an AOFS). Lowering the bias input of one laser caused it to destabilise, lowering beat frequency to ~2 MHz. Figures 6.5 (a) to (c) illustrate the interferograms captured at this lower beat frequency, measured using the RFout signals illustrated in figures 6.5 (d) to (f), with the FFT plots of these signals illustrated in figures 6.5 (g) to (i).

The phase at each point of the interferogram was fixed with respect to the phase

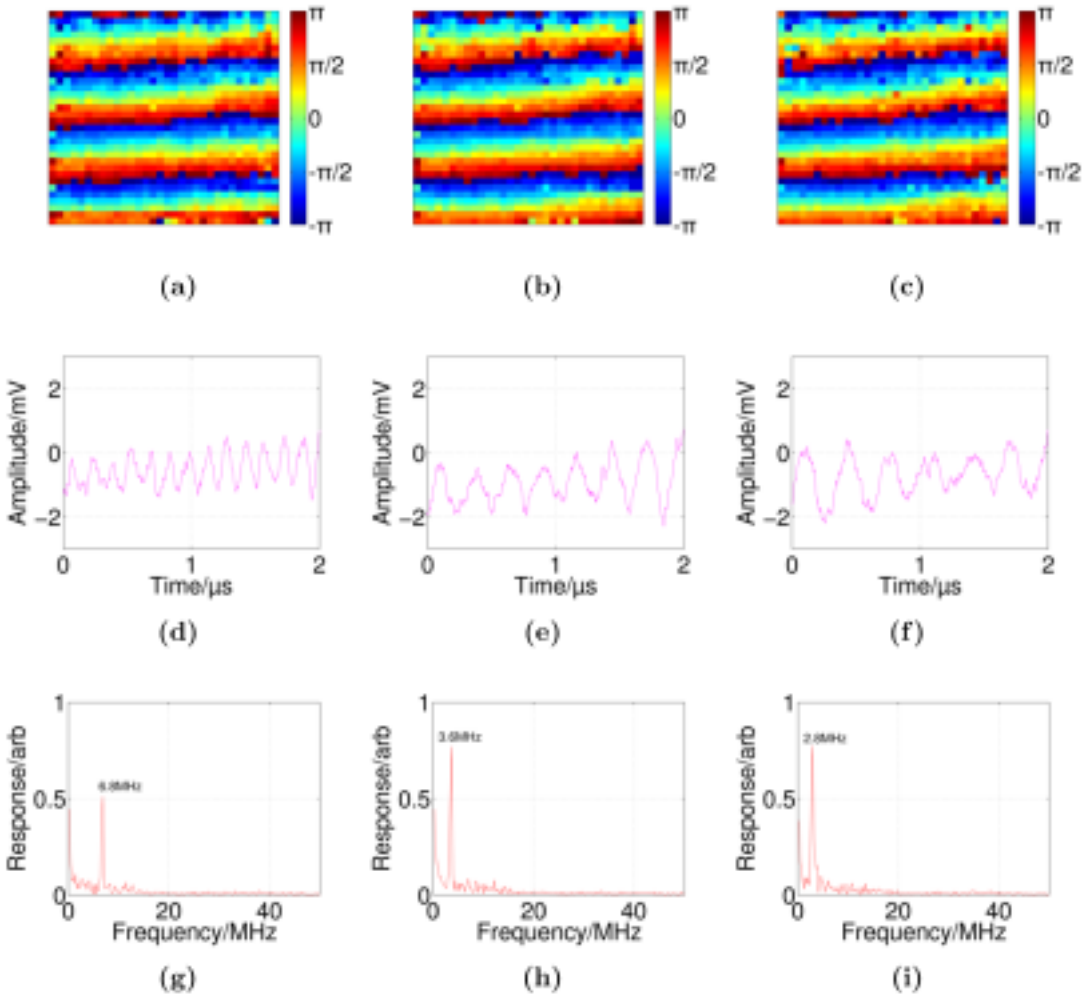

Figure 6.4: The images of interference fringe patterns generated using two lasers. The lasers were in a stable state; the top (a to c) images show three images over a length of time. The RFout was also captured at the point of image capture, shown in the middle (d to f) and FFT plots that were generated from the snapshot RFout waveform, shown at the bottom (g to i).

of the RFout signal and by the delay in the external electronic devices (filters, amplifiers, phase splitters, etc). The phase response (delay) of some of these electronics changed below 2 MHz. This explains the shift in relative phase pattern seen across each of the interferograms.

6.2.3 Fringe patterns as beat frequency approaches 0 Hz

Further tests of the interferometer at low modulation frequencies were conducted by reducing the bias input further. Figures 6.6(a) and (d) illustrate the captured

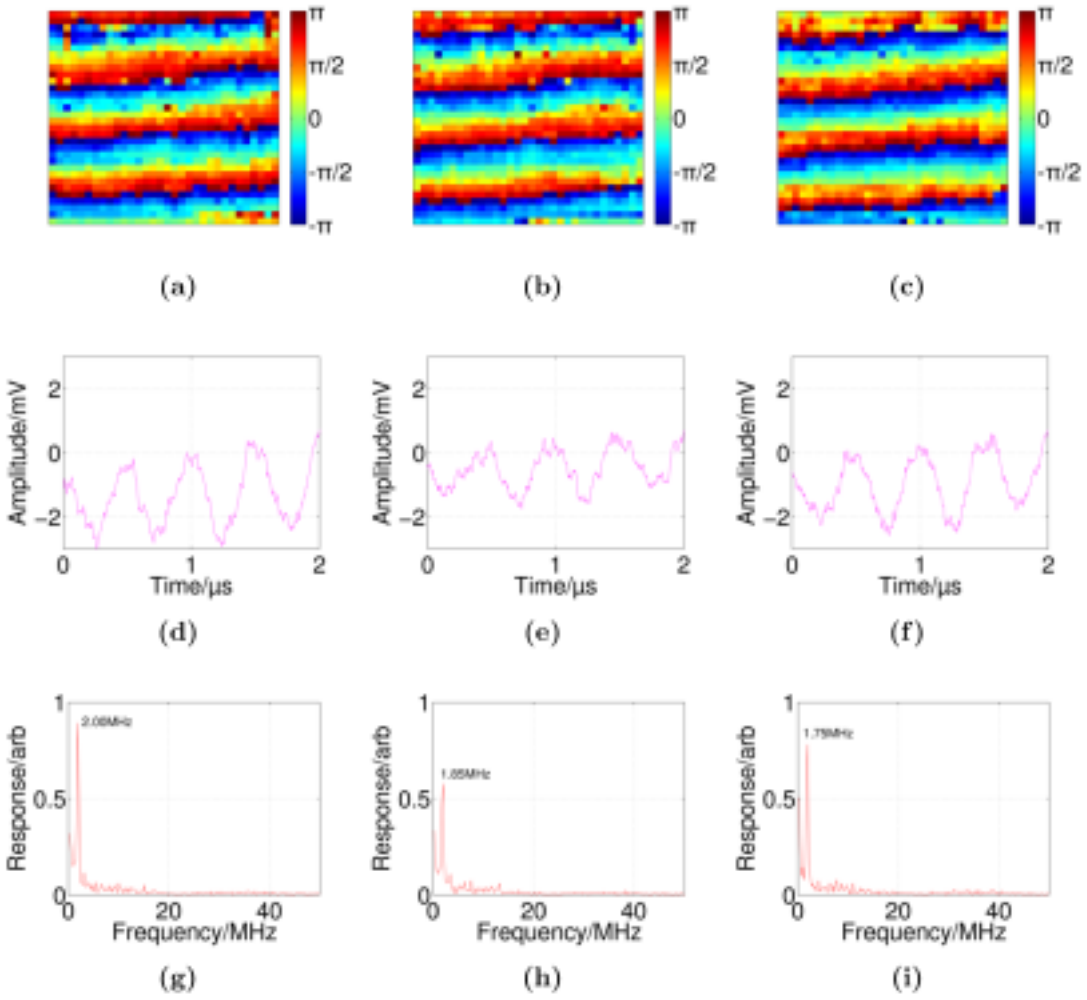

Figure 6.5: Phase images captured by the MLC of the two lasers interfering shown on top (a to c), the RFout signal measured at the time of fringe pattern capture shown in the middle (d to f) and the FFT of the RFout signals shown at the bottom (g to i). The phase images show a shift in the phase as the modulation frequency decreased.

phase images, figures 6.6(b) and (e) illustrate the RFout signals recorded at the time of capture, and figures 6.6(c) and (f) illustrate the FFTs of the RFout signals.

As the lowering of the beat frequency continued (as shown in figure 6.6(c)), the output interferograms became distorted, shown in figure 6.6(a). The fringes appeared to show signs of clipping; this was due to the low frequency cutoff of the electronic components (amplifiers, phase splitters) and of the MLC itself.

After falling to a DC beat frequency, the observed beat frequency began to climb again, illustrated in figure 6.6(f). The interferogram, shown in figure 6.6(d),

appears to be an inverted version of the fringe patterns seen thus far due to a cross-over in frequency between the two lasers. This gives a relative 'negative' frequency, which appears as a rise in the detected beat frequency at RFout, and 'negative' phase, showing an inversion in the fringes.

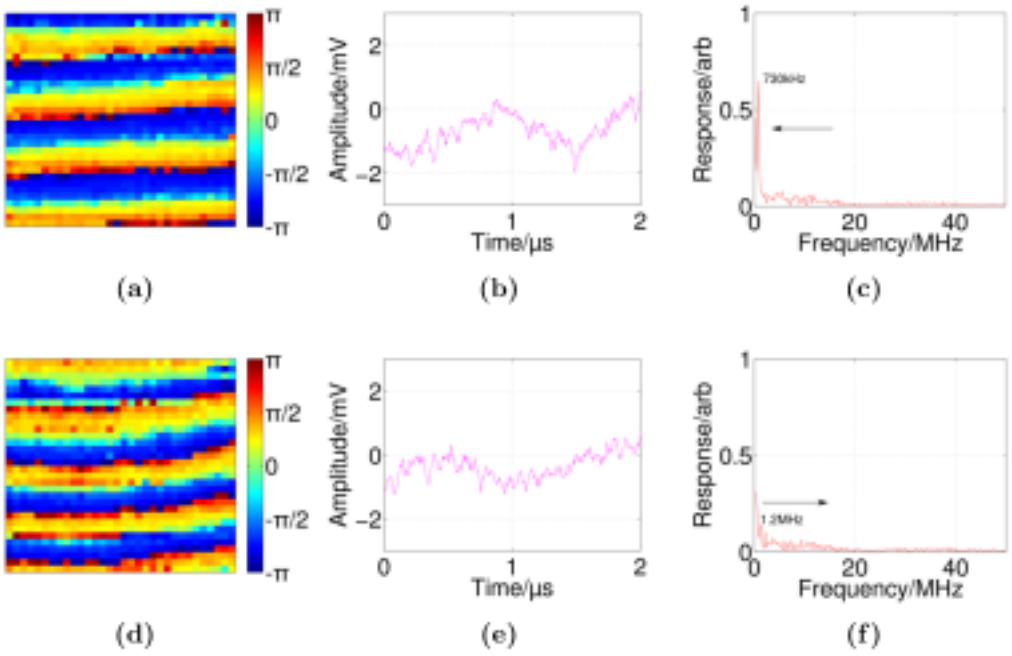

Figure 6.6: Fringe pattern phase images shown at left (a)(d), RFout plots of these images shown in middle (b)(e), and FFT of these RFout plots shown at right (c)(f) of the two lasers interfering as the beat frequency near DC (0 Hz). The captured fringe patterns appear distorted and an inversion in the fringe pattern was seen as the observed beat frequency fell to zero and began to rise again.

6.2.4 Inversion of fringe patterns

An inversion in the fringe patterns was produced when there was a crossover in the interfering beams' optical frequency. The beat frequency was equal to $\Delta f = f_1 - f_2$, where the frequencies of laser 1 and laser 2 are represented by f_1 and f_2 respectively. If $f_1 > f_2$, the beat frequency could be thought of as being 'positive', and as f_1 decreased until $f_1 < f_2$, the beat frequency changed sign, i.e. relative 'negative' frequency.

The inverted fringe patterns captured exhibit similar behaviour with respect to

their 'positive' frequency counterparts. Figures 6.7(a) to (c) illustrate the captured inverted interferograms, with the measured RFout signal illustrated in figures 6.7(d) to (f), and the relative 'negative' frequency spectra at the point of capture illustrated in figures 6.7(g) to (i).

The fringes seen in the previous interferograms (e.g. figure 6.4(a)) have increasing phase from the top of the pattern to the bottom, whilst in these inverted fringes, the phase decreases from the top to the bottom (indicated by the colour). The inversion and the 'negative' frequency observed is only relative and depends on perspective.

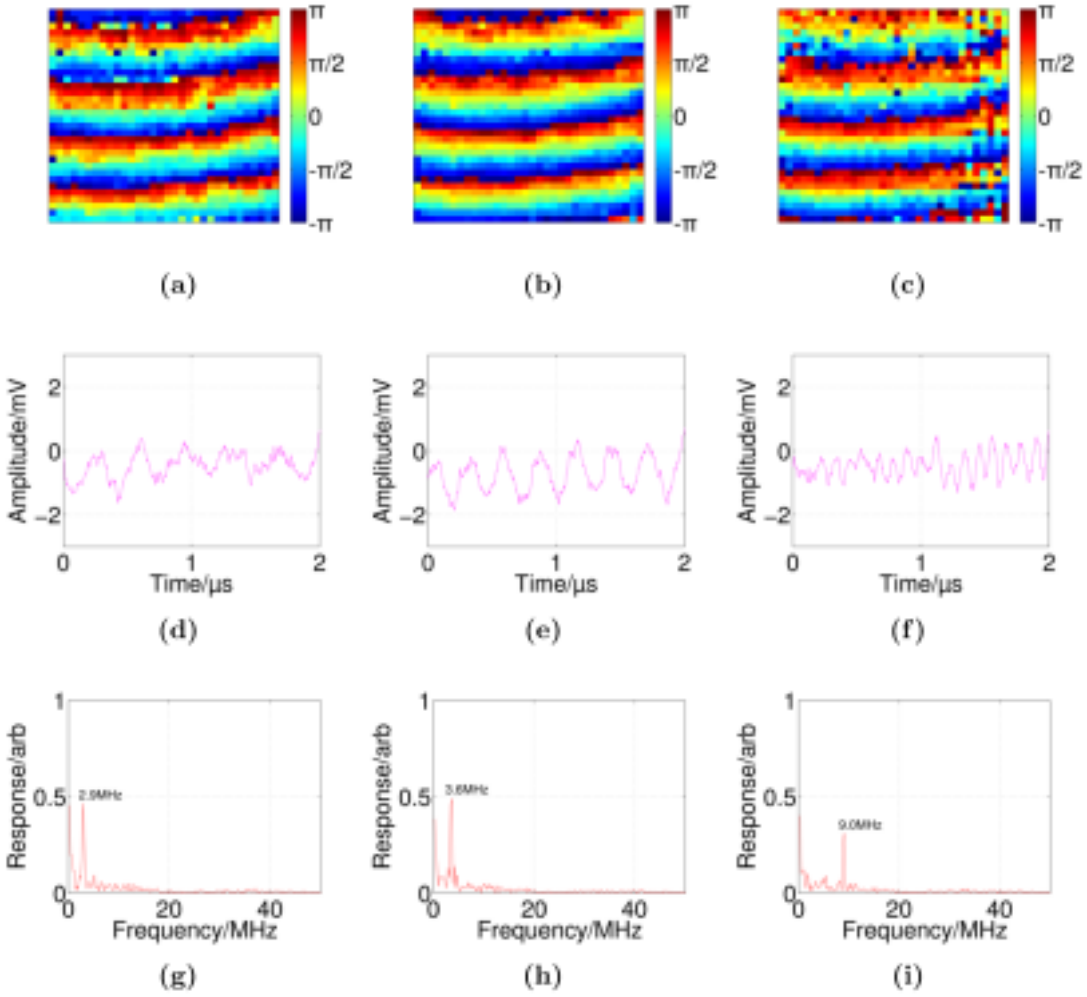

Figure 6.7: Fringe patterns of two lasers interfering, shown top (a to c), the RFout signal shown in the middle (d to f), and the FFT of the RFout signal is shown at the bottom (g to i). The phase images are inverted when compared with earlier images (figure 6.4(a) to (c)).

6.2.5 Two-laser interferometer object experiment

Similar to the experiment conducted in section 4.4, an object was placed in to the path of one of the laser beams to induce a phase step. In this case, a microscope slide was placed on the right-hand side of one of the beams. The experiment was conducted at both a 'negative' frequency, illustrated in figure 6.8(a), and a 'positive' frequency, illustrated in figure 6.8(b). These images were unwrapped; figures 6.8(c) and (d) illustrate the 'negative' and 'positive' unwrapped images respectively.

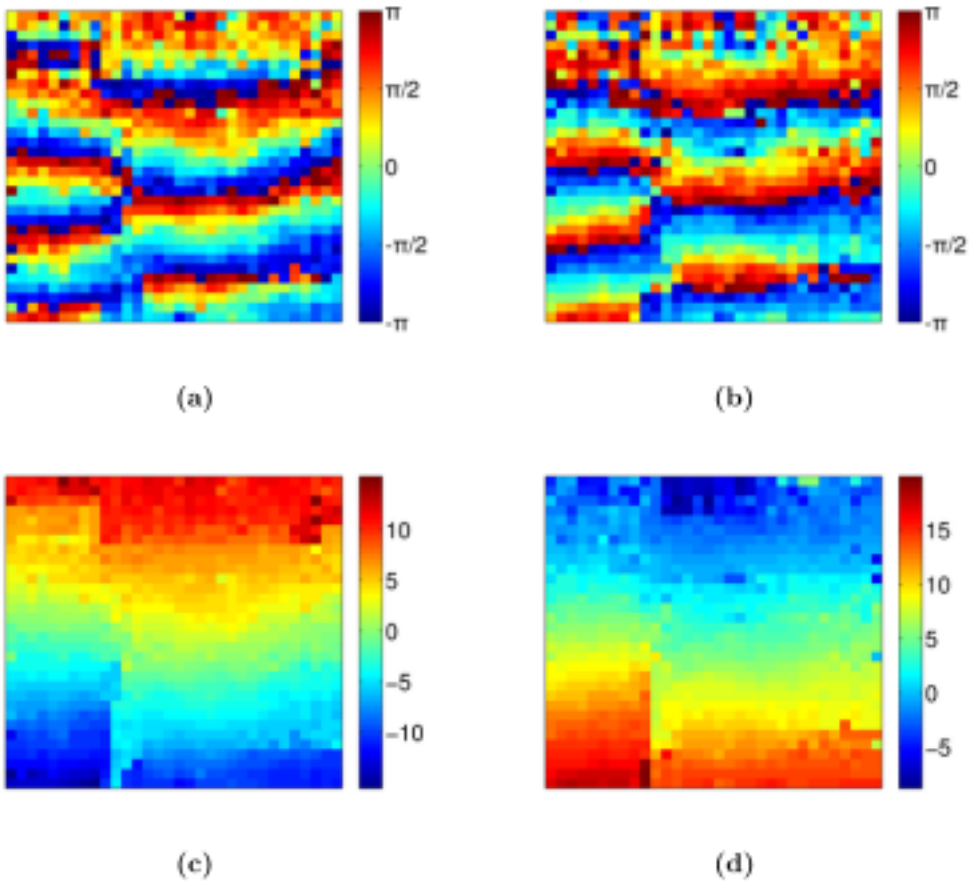

Figure 6.8: Fringe patterns generated by interfering two lasers and introducing a microscope slide in front of one laser. Wrapped captured images are shown on top (a and b) and unwrapped processed images are shown at the bottom (c and d), colour represents radians. The left (a and c) and right (b and d) images have been taken with the beat frequency at either sides of DC and are inverted versions of each other. The slide can be seen to cause a phase step on the right hand side of the images.

The unwrapped images were normalised using control images, illustrated in fig-

ures 6.9(a) and (b). Both images show constant phase on the left section of the image, where no slide was present, and phase change on the right part of the image, where light passed through the slide.

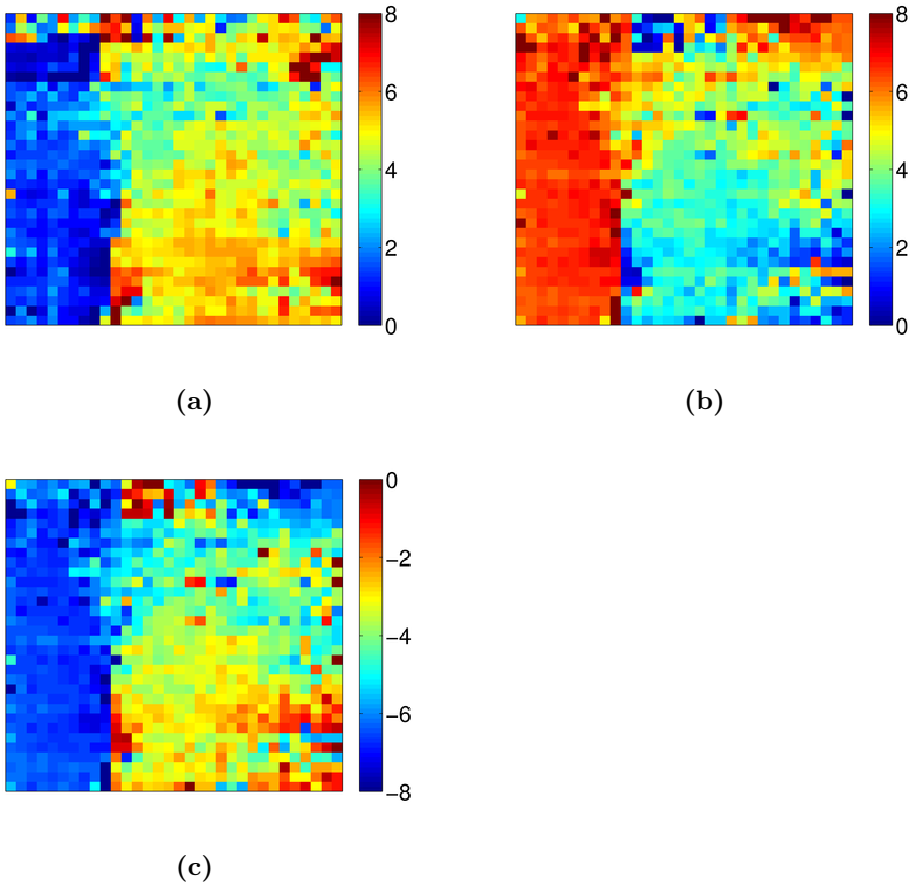

Figure 6.9: Normalised unwrapped images of the interferogram with a slide introduced (on the right side of the images), the normalised images on the top (a and b) are of figure 6.8(c) and (d) respectively. Both images show constant phase on the left half of the images, and the phase step due to the slide on the right half. The bottom (c) image is the inverted (× -1) outcome of image (b).

Figure 6.9(c) shows the post-capture inversion of figure 6.9(b) (i.e. image was multiplied by -1). Even though the scale had been shifted (phase offset by -8 radians), both figure 6.9(a) and (c) look similar, as the pattern shape and aberrations are roughly in similar areas. This shows that with an object being characterised, the same result can be obtained, independent of whether the MLC captures with a relative 'positive' or 'negative' fringe pattern.

6.3 Two-laser interferometer system conclusions

The two laser interferometer system explored in this chapter was an extension to the ultrastable system presented in chapter 5. The system's capability to adapt to large beat (modulation) frequency changes lead to this two laser interferometer application.

The two lasers used for interfering were truly independent as the stabilisation system does not depend on the other laser source. After interfering the beams of the two lasers, the beat frequency generated drifts over time ($\sim$3 MHz over 30 minutes). The interferometer, and specifically the MLC's RFout feedback loop, was used to not only capture interferograms at different frequencies, but also to capture interferograms as the frequency changed mid-capture. The pixel data can be read in real time after being addressed, and the I/Q output was determined continuously on all pixels using the instantaneous modulation frequency observable at the RFout. The major disadvantage of operating the system with a varying modulation frequency was the varying phase response due to that frequency (i.e. phase response of the MLC/phase-splitters/filters/etc), however this could have been counteracted by performing calibration experiments and measuring the instantaneous frequency.

The lasers themselves were simple to create, built using readily available components. Although the lasers are required to have a degree of frequency stability, the system would be able to cope if the frequency difference between them drifted by several MHz. The optical arrangement itself was also much simpler than the single light source equivalent interferometer; no optical components are required, meaning less aberrations and systematic errors would be present in the interferograms. For the end user, these factors mean simple assembly and alignment of the apparatus (as well as lower costs), leading to certain applications not requiring an optical/laser engineer to build the system.

The two laser interferometer also has other advantages over the single split source interferometer. The two individually stabilised lasers can be separated by a large distance (and therefore have a large OPL difference) with no interaction needed between them (figure 6.2) without losing fringe visibility; in the presented interferometer the lasers are kept 35 cm apart.

Chapter 7

Summary and discussion

This final chapter summarises the content explored in this thesis. The operation and observations of the presented experiments are discussed and possible improvements to the systems are analysed.

7.1 Summary of thesis

Chapter 1 presented an overview of interferometry. This included the purpose of using interferometry, the implication of an observable phase shift in a wave, and the theory behind a generated interference pattern. Different methods of extracting the phase from an interference pattern was explored as well as a selection of interferometer arrangements. Electronic methods of light capture were also explored, along with the practical limitations of detection, such as source coherence limits and sources of signal noise.

Chapter 2 presented a literature review of different modulated light cameras and other light demodulating schemes. The chapter also reviewed interferometer systems that were comparable to the three experimental arrangements discussed in this thesis; these included widefield or parallel multi-point heterodyne interferometer systems, techniques to stabilise a captured interferogram using electronic feedback, and a systems that captured interferograms generated by two lasers.

Chapter 3 discussed the different components and methods used to capture the widefield heterodyne interferograms shown in this thesis. Most notably, an overview of the MLC chip was given, exploring the key features of the camera and an anal-

ysis of its operating principle. Other components reviewed included the HeNe laser sources and the AOFS. The chapter also explored the MLC interface setup.

In chapter 4, the widefield interferogram images captured using the MLC were presented. The MLC was used to capture both homodyne and heterodyne widefield interference patterns; the images captured were compared. The MLC was also tested by comparing a theoretical interference image (using optical setup measurements) against a captured image. Finally, a phase shift of part of a pattern, introduced by a microscope slide, was detected as a proof-of-concept experiment.

In chapter 5, the ultrastable widefield interferometer system was presented. Instability in captured interferograms was likened to temporary changes in phase difference. The MLC ultrastable system used a feedback loop (electronic self-reference) to eliminate the temporally varying phase, leaving only a relative fringe pattern. The limits of the system were discussed and the fringe patterns captured using the MLC were shown. Comparisons were made between the standard (chapter 4) and ultrastable interferometer system by introducing a vibration element into one of the arms of an interferometer. A second experiment to determine the system operational bandwidth was conducted (the bandwidth determined the system's vibration velocity immunity limit). Images were captured of a chrome grating to verify the correct operation of the detector.

In chapter 6, a novel interferometer design using two separate (independent) lasers was presented. The challenges in obtaining fringe patterns modulated at a randomly varying frequency was explored and how the ultrastable system could be used to overcome these challenges. Two frequency stabilised HeNe lasers were built in-lab (using a He-Ne laser tube, 34AWG wire, photodiodes, op-amps and other readily available components). Interference fringe patterns were captured continuously using the ultrastable system even as the beat frequency between the lasers varied. Inversions in the pattern were detected as the beat entered the relative 'negative' frequencies.

7.2 Discussion

The interference patterns generated by beams of light are dependent on the phase difference between them. This in turn can be used to determine the dissimilarities between each beams propagation path (e.g. object placed into a beam path or change in path length, as shown in figure 1.3). Often, the phase across an area (i.e. widefield region) is required, for example, in surface profilometry. In homodyne interferometry, the phase is represented as a static intensity which is easy to digitally capture but may be susceptible to background optical influences (e.g. sunlight). Techniques such as spatial domain filtering and phase stepping interferometry could be employed to extract the phase, however, these methods have drawbacks such as not being immune to low frequency influence or additional phase error (discussed further in section 1.3).

A solution to this is to use heterodyne interferometry where the pattern is modulated by interfering beams with different optical frequencies. Using this method is advantageous; by using a high modulation frequency, low frequency contributions to an interferogram can be filtered out. However, detecting/extracting phase information in the widefield region is challenging; the work presented in this thesis used a modulated light camera (MLC) to capture and demodulate widefield heterodyne interferograms. All the positives of a homodyne interferometer system, such as a simple and cost effective interferometer setup (assuming mass production of the MLC), real time data measurements, and widefield capture, are all attributes of the presented systems.

The interferometer system was modified to also capture ultrastable interferograms, where the system used a feedback loop to track changes in temporally varying phase (e.g. due to vibrations). This provided a relative widefield interferogram (phase relative to a single point on the MLC). The ultrastable system was capable of being immune to large amounts of piston phase change, which is useful in vibration heavy or temperature variant environments, or where the propagation medium changes rapidly (e.g. in the atmosphere). The system is also compact and simple in its design. The presented ultrastable system was incorporated into a double path interferometer which retained a separate reference beam; the separate beam could be used to increase the amplitude of the incident optical signal. This increase in amplitude is comparable to electronically amplifying a detected signal, but will not be subject to additional electronic amplifier

noise.

As an extension to the ultrastable system, the MLC was also used to capture the phase pattern generated by two independent lasers. This had been difficult in the past as the beat frequency generated between the two lasers would appear to randomly change, however, the ultrastable system was used to track this temporally varying change and capture continuous two laser interference fringe patterns. Effectively, as long as the sources remain stable, they could be kept an indefinite distance apart (as they are completely independent) and the system would still be able to capture interference patterns. With the light sources separated, interferometer designs are no longer confined to the usual optical restrictions (e.g. include splitting a beam).

7.3 Noise contributions

The limiting factor in determining the phase of the presented interferometer fringe patterns was on the uncertainty of the system output (i.e. system performance). Noise introduced at the different design stages of the modulated light camera contribute towards the phase uncertainty (causing undesired random fluctuations of the useful information signal). The sources of electronic noise include thermal noise, which varies depending on the device temperature (detailed in section 1.7.2), electronic shot noise, which varies with the signal magnitude (detailed in section 1.7.1), and flicker noise, which varies depending on the device properties and operating frequency (detailed in section 1.7.3). In addition, integrated circuit devices such as the MLC are susceptible to crosstalk (electronic interference) where signals are affected by other nearby signals [33] (either in-pixel or cross pixel). When capturing interferograms, environmental effects, such as vibration acting on the interferometer also add to the phase error (discussed in section 1.7.5 and section 5.4.3). The ultrastable system employs a reference signal feedback (RFout) to eliminate the piston phase variation from the captured interferogram. However, noise in the feedback signal increases the phase uncertainty (detailed in section 5.4.2).

To reduce the amount of noise (and phase uncertainty) in the system, preventative methods can be used. Thermal noise can be reduced by better regulating

the temperature of the device. The MLC drew in $\sim$420 μA and temperatures upto 60 °C were measured on the device; effective use of heatsinks, heat extraction fans (although this may increase vibration) or more comprehensive cooling methods (e.g. liquid cooling, Peltier cooler, etc.) would decrease thermal noise. Flicker noise can be the dominant noise source at low operational frequencies and operating the MLC at higher frequencies (by using a high intensity light source, using the vtune bias, or by increasing the pixel fill factor) would reduce the flicker noise influence. A larger signal would also decrease the relative influence of shot noise, since show noise increases only by the square root of the signal magnitude. Additionally, all random noise can be reduced by decreasing the system bandwidth (decreasing and sharpening the cut off for the low pass output filters) and increasing data averaging (discussed in section 3.2.4); a faster acquisition card could be used to maintain similar frame rates. To reduce IC crosstalk, design techniques such as increased spacing between adjacent modules or signal line redesigning could be employed [46].

7.4 Future considerations

To continue to take this work forward, ideally, the next iteration of the MLC would be required. A few specification enhancements could relax the design criteria of the interferometers, and improve the quality and accuracy of the images captured. These include a higher pixel resolution, a decrease of in-pixel noise contributions (and improve the phase output and RFout SNR), an increase in the operation frequency bandwidth and an improvement of the pixel frontend design to make use of a larger 'linear' response region. However, designing a camera with these enhancements would require time (including simulation time) and cost due to a smaller fabrication processes being used or by using a bespoke design (e.g. buried multi-junction photodiodes).

Whilst these design considerations for the MLC would improve the image SNR, it is key to note that the current MLC has yet to be tested extensively. More comprehensive tests of the camera should be conducted, where the phase error is measured against modulation frequencies, DC light intensities, modulation depths, and different on-chip biasing conditions, to see if an improvement could be made to the error figure determined in section 3.1.3.3. Additional tests could

be performed to observe the effects on the phase output if the LO signal was changed, such as different voltage offsets and modulation depths, waveforms, and the influence of varying degrees of noise.

As described in section 3.2.3.1, there were several iterations of the PCB design; some of the components (such as the phase splitters) as well as the PCB design itself, may not be optimised for small signal or RF signal transfer. A more comprehensive PCB design software could be used to simulate the performance of an interface board and components (using datasheet information) before fabrication to improve output SNR.

One of the other camera functions, introduced in the MLCv6, was the input of a vtune bias current. This current is fed in as an addition to the photodiode current. The system presented in this thesis did not make use of this function as it could have been used to 'push' the incident signal further up into the apparent 'linear' region of the logarithmic response curve (figure 3.2); i.e. higher DC current seen at the transimpedance amplifier (photocurrent + vtune bias current). This function warrants further investigation to see if this expands system limits.

Many of the experimental system limits determined (such as the ultrastable immunity limits) were mainly due to the equipment used to test the system; for example, the mirror mount and filters/amplifiers in the ultrastable system, and the stability of the lasers in the two laser interferometer setup. These external components could have been better optimised to provide experimental results closer to the theoretical limits.

The next stage of the ultrastable interferometer test would be to implement it into a real system. It could be compared with a comparable common-path interferometer on the phase acquisition speed and performance under various conditions, for example, low light levels or scattered light (each system has advantage and disadvantages in these scenarios). Another experiment that could be conducted would be to use the ultrastable system to construct both relative and absolute interferograms; an external fringe counter could be integrated into the system using the RFout pixel as an independent photodiode.

Unlike most other interferometers, the two laser system is free from many of lim-

itations/conditions that are required from interferometer setups. The ability to put separate lasers anywhere could enable a new range of widefield interferometer designs. Considerations should be made in order to deduce situations/scenarios that would warrant the use of a two laser interferometer. Building optical systems to demonstrate these interferometers (e.g. free space communications or long distance interferometry) could be included as part of future work.

Appendix A

Appendix: Optical setup

To generate the concentric fringe pattern shown in section 4.3, a spherical wave was interfered with a plane wave. To generate the spherical wave, the lens arrangement shown in figure A.1 is used.

The position of the exit lens is moved by δm_L so that $S_1 < F_L$. The virtual point source for this beam is a distance S_2 from the exit lens and d_i from the real point source.

The distance between the virtual point source and the detector, z_s, is determined using the identities;

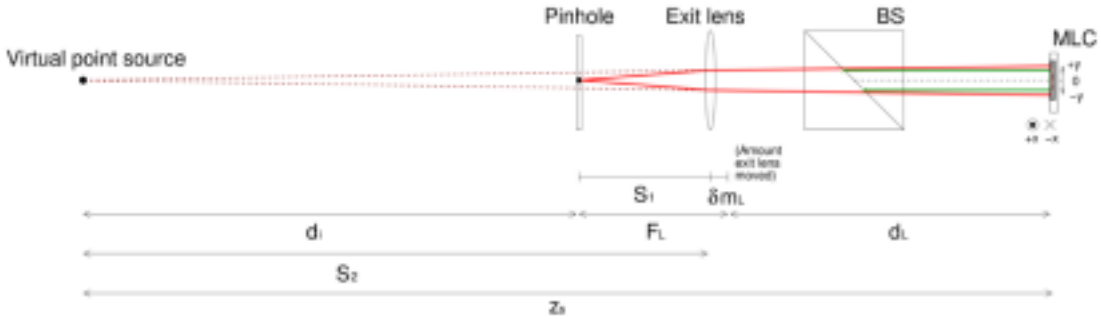

(a)

Figure A.1: A diagram showing the weakly spherical wave (red line) and plane wave (green line) incident on a detector (MLC). The weakly spherical wave is generated by moving the exit lens creating a virtual point source a fixed distance z_s away, calculable using F_L, d_L and S_1; x and y distances on the camera array (pixel pitch) are already known.

$$\begin{aligned} z_s &= d_i + F_L + d_L \\ F_L &= S_1 + \delta m_L \\ S_2 + \delta m_L &= d_i + F_L \end{aligned} \tag{A.1}$$

where F_L, δm_L, d_L are either known or measured, and S_2 is calculated using the thin lens formula $\frac{1}{f_L} = \frac{1}{S_1} + \frac{1}{S_2}$ [17].

An expected fringe pattern (as used in section 4.3) is generated using these equations, and is used to compare with a captured image to test the MLC system.

The focal length of the exit lens was equal to $F_L = 0.1\,\text{m}$ and the distance from the point of beam collimation to the detector was equal to $d_L = 0.3\,\text{m}$. The lens was moved back by $\delta m_L = 5\,\text{mm}$, and the point source (beam focus point) distance was equal to $S_1 = 0.095\,\text{m}$ from the exit lens. The virtual point source distance from the lens was therefore equal S_2 = -1.9 m. The distance from the virtual point source to the centre of the fringe pattern was equal to $z_s = 2.205\,\text{m}$.

Appendix B

Appendix: Modulated light with unknown AC function

If in a heterodyne interferometer an undefinable vibration is introduced into the system, or if the incoherent light sources are interfered, the AC component of the pattern intensity will contain a temporally varying unknown angle function. The detected signal can only be expressed as;

$$I(t) = I_{\mathrm{dc}} + A\cos\left(\theta(t)\right) \tag{B.1}$$

where $\theta(t)$ is an unknown angle function that varies over time; an example plot of such a function is shown in figure B.1 as a black trace.

The instantaneous frequency, $\omega_i(t)$, of an unknown angle function can be expressed as the differential of the function, i.e. the frequency over an infinitesimally small period of time, such that;

$$\frac{d\theta}{dt} = \omega_i(t) \tag{B.2}$$

This instantaneous frequency is also unknown. As a comparison, a stable angle function (from a stable heterodyne fringe pattern) is plotted in figure B.1 (blue trace) alongside the unknown angle function; over the short time Δt, the stable and unstable fringe patterns have the same frequency ($\omega_i = \omega_0$). The instantaneous frequency can be substituted back into the fringe pattern intensity equation (equation 1.17) after integration, such that;

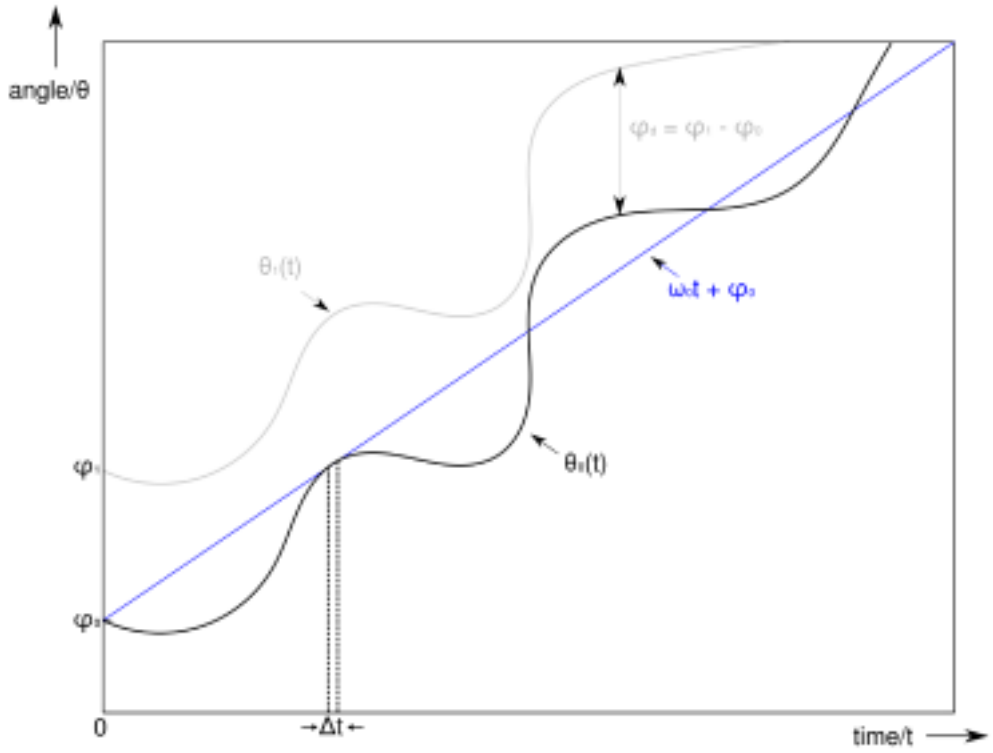

Figure B.1: Example plot of an unknown angle function (black), $\theta_0(t)$. The graph also includes an example plot of a stable heterodyne angle function with the same phase offset (blue), and the same unknown angle function with a different phase offset (grey).

$$\begin{aligned} I(t) &= I_{\mathrm{dc}} + A\cos\left(\int_{-\infty}^{t}[\omega_i(\tau)]d\tau\right) \\ &= I_{\mathrm{dc}} + A\cos\left(\int_{0}^{t}[\omega_i(\tau)]d\tau + \phi_d\right) \end{aligned} \tag{B.3}$$

The limits of the frequency integral range from $-\infty$ to t (the time of the measurement), however, from $-\infty$ to time 0, it can be replaced by a phase offset relative to a signal with the same unknown frequency function; this is shown in figure B.1 as the difference between the $\omega_0(t)$ (black) and $\omega_1(t)$ (grey) plots.

Appendix C

Appendix: Laser stabilisation comparator circuitry

A stabilisation circuit was used to compare the two emitted modes from the built laser. Each mode has different polarisation states and by using a polarising beam-splitter, the different intensities of the modes was measured using photodiodes. The current generated from each mode was compared; depending on their ratio, the amount of current going to a heater coil was adjusted. An offset bias current could also be controlled to manually adjust the heater current, which was used to shift the mode frequency. All circuit boards, laser tubes and some of the parts for the lasers were purchased from the *Repair FAQs* website [108], owned and run by Sam Goldwasser. He also provided direct support for some of the construction of the laser units themselves.

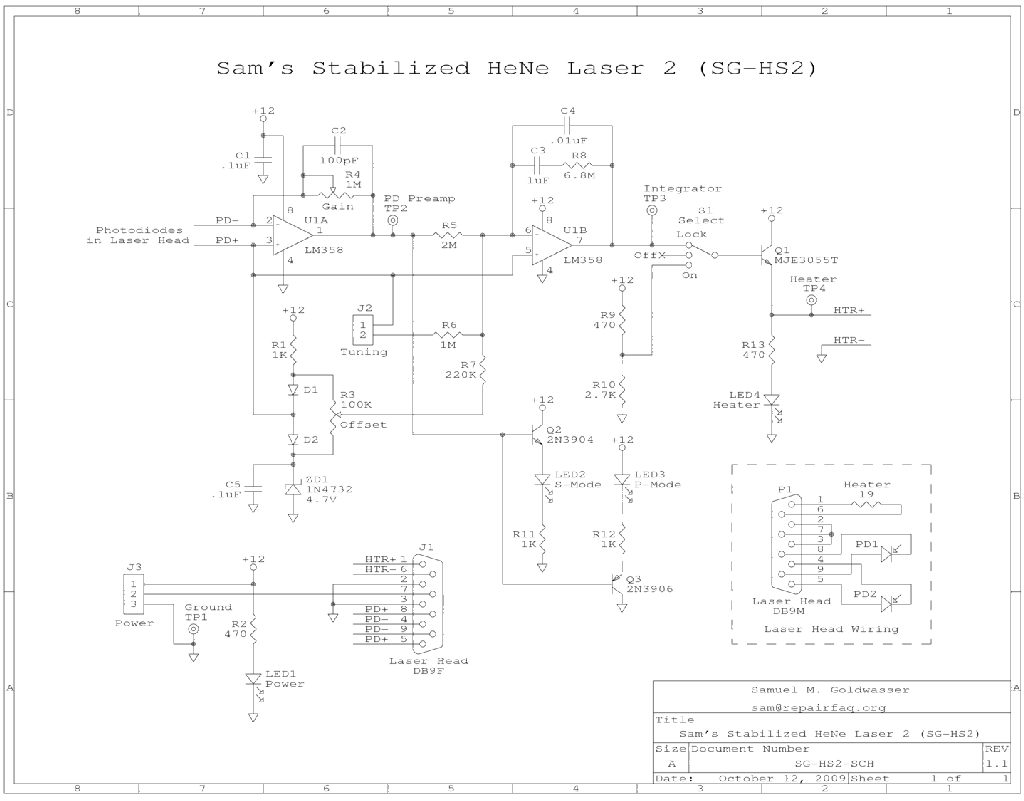

(a)

Figure C.1: Circuit used to compare the photocurrents detected at the waste exit of the stabilised laser; designed by Sam Goldwasser [108]. The photodiode currents are detected at PD+ and PD- which control the current sent to the heater at HTR+ and HTR-. An offset can also be set using resistor R3 to bias the current going into the heater.

Appendix D

Appendix: HeNe laser stability measurements

To measure the performance of the stabilised He-Ne, the beat frequency of the lasers as they interfere was measured. Even though the lasers themselves may not be emitting a stable optical frequency, their ability to maintain a constant frequency difference with respect to each other could be measured, and is the end value of interest. Figure D.1 (a) to (f) show the measured beat frequency.

The beat frequency was measured using a commercially available photodiode, shown in figure 6.2, which output a cleaner signal than can be measured using the RFout on the MLC. Over the course of around 30 minutes, the beat frequency changed by about 3 MHz ($\sim$5 MHz down to $\sim$2 MHz and eventually back up to $\sim$4 MHz). Looking at figure D.1(e) and (f), the frequency only changes by about 1 MHz over 10 Minutes.

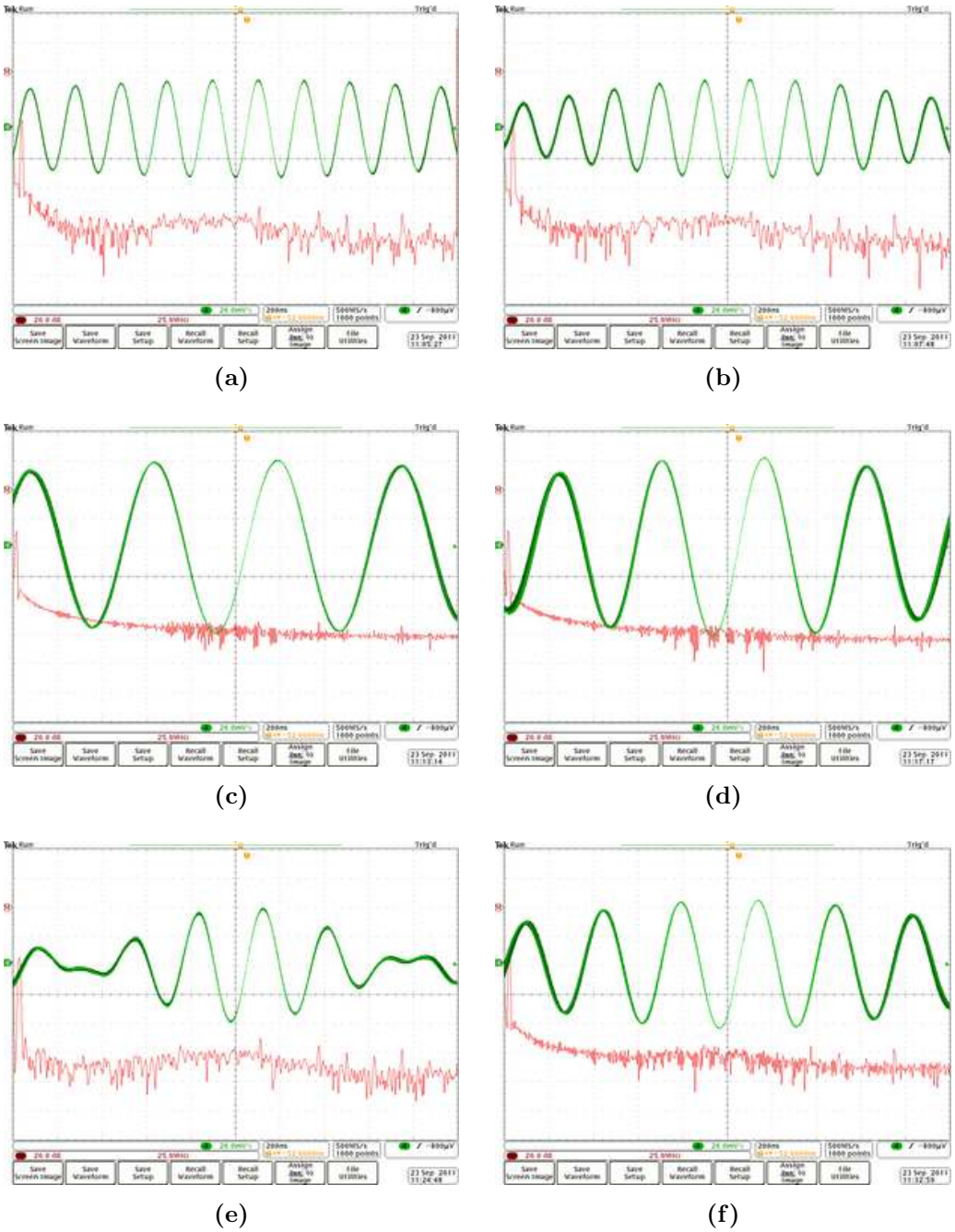

(a) **(b)**

(c) **(d)**

(e) **(f)**

Figure D.1: The stability measurements of the two in-lab designed/built He-Ne lasers. The beat frequency, generated by interfering the two lasers, is measured (green plot) at the times indicated in the bottom right of each image. An FFT of the beat signal is also shown (red plot).

Bibliography

[1] D. A. Neamen, *Semiconductor physics and devices: basic principles*. No. 978-007-108902-9, McGraw.Hill, 2012.

[2] F. M. Grimaldi, "Lumen propagatur jeu diffunditur non solum directe, refracte, ac reflexe, sed etiam alio quodam quarto modo, diffracte," *Physico mathesis de lumine, coloribus, et iride, aliisque annexis libri duo*, pp. 1–11, 1665.

[3] T. Young, "Outlines of experiments and inquiries respecting sound and light. by thomas young, m. d. f. r. s. in a letter to edward whitaker gray, m. d. sec. r. s.," *Philos. Trans. R. Soc. London*, vol. 90, pp. 106–150, Jan. 1800.

[4] I. Newton, *Opticks or, a treatise of the reflexions, refractions, inflexions and colours of light*. London Press, first edition ed., 1704.

[5] T. Young, "The bakerian lecture: Experiments and calculations relative to physical optics," *Philos. Trans. R. Soc. London*, vol. 94, pp. 1–16, Jan. 1804.

[6] T. Young, "Experimental demonstration of the general law of the interference of light," *Philos. Trans. R. Soc. London*, vol. 93, Jan. 1803.

[7] A. A. Michelson, "The relative motion of the earth and the luminiferous ether," *Am. J. Sci.*, vol. 22, pp. 120–129, 1881.

[8] J. C. Maxwell, "On physical lines of force, part ii, the theory of molecular vortices applied to electric currents," *Phil. Mag.*, vol. 21, pp. 338–348, 1861.

[9] G. G. Stokes, "On the theories of the internal friction of fluids in motion, and of the equilibrium and motion of elastic solids," *Trans. Cambridge Philos. Soc.*, vol. 8, pp. 287–319, 1949.

[10] A. Michelson and E. Morley, "On the relative motion of the earth and the luminiferous ether," *Am. J. Sci.*, vol. 34, pp. 333–345, 1887.

[11] P. Hariharan, *Basics of interferometry*. No. 978-0-12-373589-8, Academic press, 2007.

[12] P. Hariharan, *Optical interferometry*. No. 9780123116307, Academic press, 2003.

[13] Y. Ohtsuka and I. Sasaki, "Laser heterodyne measurement of small arbitrary displacements," *Opt. Comm.*, vol. 10, no. 4, pp. 362 – 365, 1974.

[14] N. A. Riza and M. A. Arain, "Angstrom-range optical path-length measurement with a high-speed scanning heterodyne optical interferometer," *Appl. Opt.*, vol. 42, no. 13, pp. 2341 – 2345, 2003.

[15] N. A. Massie, M. Dunn, D. Swain, S. Muenter, and J. Morris, "Measuring laser flow fields with a 64-channel heterodyne interferometer," *Appl. Opt.*, vol. 22, pp. 2141–2151, Jul 1983.

[16] A. Kimachi, "Real-time heterodyne speckle pattern interferometry using the correlation image sensor," *Appl. Opt.*, vol. 49, no. 35, pp. 6808 – 6815, 2010.

[17] E. Hecht, *Optics*. No. 0-321-18878-0, Addison Wesley, 2002.

[18] J. C. Maxwell, "On physical lines of force, part i, the theory of molecular vortices applied to magnetic phenomena," *Phil. Mag.*, vol. 21, pp. 161–175, 1861.

[19] J. C. Maxwell, "On physical lines of force, part iii, the theory of molecular vortices applied to static electricity," *Phil. Mag.*, vol. 23, pp. 12–24, 1862.

[20] J. C. Maxwell, "On physical lines of force, part iv, the theory of molecular vortices applied to action of magnetism on polarisation," *Phil. Mag.*, vol. 23, pp. 85–95, 1862.

[21] M. Shur, *Introduction to electronic devices*. John Wiley and sons, 1996.

[22] J. Budzinski, "Snop: a method for skeletonization of a fringe pattern along the fringe direction," *Appl. Opt.*, vol. 31, pp. 3109–3113, Jun 1992.

[23] D. W. Robinson, "Automatic fringe analysis with a computer image-processing system," *Appl. Opt.*, vol. 22, pp. 2169–2176, Jul 1983.

[24] M. Takeda, H. Ina, and S. Kobayashi, "Fourier-transform method of fringe-pattern analysis for computer-based topography and interferometry," *J. Opt. Soc. Am.*, vol. 72, pp. 156–160, Jan 1982.

[25] A. Kimachi, "Real-time heterodyne imaging interferometry: Focal-plane amplitude and phase demodulation using a three-phase correlation image sensor," *Appl. Opt.*, vol. 46, no. 1, pp. 87 – 94, 2007.

[26] J. H. Bruning, D. R. Herriott, J. E. Gallagher, D. P. Rosenfeld, A. D. White, and D. J. Brangaccio, "Digital wavefront measuring interferometer for testing optical surfaces and lenses," *Appl. Opt.*, vol. 13, pp. 2693–2703, Nov 1974.

[27] P. Carre, "Installation et utilisation du comparateur photoelectrique et interfrential du bureau international des poids et mesures," *Metrologia*, vol. 2, pp. 13–23, 1966.

[28] L. M. Frantz, A. A. Sawchuk, and W. von der Ohe, "Optical phase measurement in real time," *Appl. Opt.*, vol. 18, pp. 3301–3306, Oct 1979.

[29] P. Hariharan, B. F. Oreb, and T. Eiju, "Digital phase-shifting interferometry: a simple error-compensating phase calculation algorithm," *Appl. Opt.*, vol. 26, pp. 2504–2506, Jul 1987.

[30] R. Crane, "Interference phase measurement," *Appl. Opt.*, vol. 8, pp. 538–542, 1969.

[31] M. J. Lavan, W. K. Cadwallender, G. E. V. Damme, and T. F. D. Young, "Optical heterodyne interferometer with improved two-channel crosstalk signal-to-noise ratio," *Rev. Sci. Instrum.*, vol. 47, no. 10, pp. 1306–1307, 1976.

[32] H. Povel, H. Aebersold, and J. O. Stenflo, "Charge-coupled device image sensor as a demodulator in a 2-d polarimeter with a piezoelastic modulator," *Appl. Opt.*, vol. 29, pp. 1186–1190, Mar 1990.

[33] B. P. Lathi, *Modern design and analog communication systems*. No. 0-19-511009-9, Oxford University Press, 1998.

[34] F. Twyman and A. Green, *British Patent No. 103832*. 1916.

[35] F. Twyman, "Interferometers for the experimental study of optical systems from the point of view of the wave theory," *Phil. Mag.*, vol. 35, p. 49, 1918.

[36] F. Twyman, "On the correction of optical surfaces," *Astrophys. J.*, vol. 48, p. 256, 1918.

[37] L. Zehnder, "Ein neuer interferenzrefraktor," *Zeitschrift fr Instrumentenkunde*, vol. 11, p. 275285, 1891.

[38] L. Mach, "Ueber einen interferenzrefraktor," *Zeitschrift fr Instrumentenkunde*, vol. 12, p. 8993, 1892.

[39] M. V. R. K. Murty, "The use of a single plane parallel plate as a lateral shearing interferometer with a visible gas laser source," *Appl. Opt.*, vol. 3, pp. 531–534, Apr 1964.

[40] M. Riley and M. Gusinow, "Laser beam divergence utilizing a lateral shearing interferometer," *Appl. Opt.*, vol. 16, pp. 2753–2756, 1977.

[41] O. Bryngdahl, "Applications of shearing interferometry," *Prog. Opt.*, vol. 4, p. 3783, 1966.

[42] W. P. Linnik, "A simple interferometer for the investigation of optical systems," *C. R. Acad. Sci. URSS*, vol. 5, pp. 208–210, 1933.

[43] R. N. Smartt and W. H. Steel, "Theory and application of point-diffraction interferometers," *Jpn. J. App. Phys.*, vol. 14S1, no. Supplement 14-1, pp. 351–356, 1975.

[44] G. Sagnac, "L'ether lumineux demontre par l'effet du vent relatif d'ether dans un interferometre en rotation uniforme," *C.R.*, vol. 157, pp. 708–710, 1913.

[45] G. Sagnac, "Sur la preuve de la realite de l'ether lumineux par l'experience de l'interferographe tournant," *C.R.*, vol. 157, pp. 1410–1413, 1913.

[46] A. Hastings, *The art of analog layout*. Prentice Hall, 2001.

[47] W. S. Boyle and G. E. Smith, "Charge coupled semiconductor devices," *Bell Sys. Tech. J.*, vol. 49, no. 4, p. 587593, 1970.

[48] R. Light, *Design and Implementation of an Integrating Modulated Light Camera*. PhD thesis, The University of Nottingham, 2008.

[49] D. J. Denvir and E. Conroy, *Electron multiplying 'CCD' technology: the new 'ICCD'*. 2003.

[50] G. Cristobal, P. Schelkens, and H. Thienpont, *Optical and Digital Image Processing*. Wiley, 2011.

[51] G. P. Weckler, "Operation of p-n junction photodetectors in a photon flux integrating mode," *IEEE J. Solid-State Circuits*, vol. 2, pp. 65–73, 1967.

[52] S. G. Chamberlain, "Photosensitivity and scanning of silicon image detector arrays," *IEEE J. Solid-State Circuits*, vol. 4, pp. 333 – 342, 1969.

[53] G. Kopp, G. Lawrence, and G. Rottman, "The total irradiance monitor (tim): Science results," *The Solar Radiation and Climate Experiment (SORCE)*, p. 129139, 2005.

[54] AMS, *0.35 um CMOS C35 process parameters eng-182*. 2004.

[55] S. Achamfuo-Yeboah, *Design and Implementation of a CMOS Modulated Light Camera*. PhD thesis, The University of Nottingham, 2012.

[56] H.-A. Bachor and P. Fisk, "Quantum noise - a limit in photodetection," *Appl. Phys. B*, vol. 49, no. 4, pp. 291–300, 1989.

[57] W. Schottky, "Uber spontane stromschwankungen in verschiedenen elektrizitutsleitern," *Annalen der physik*, vol. 57, pp. 541–567, 1918.

[58] J. B. Johnson, "Thermal agitation of electricity in conductors," *Phys. Rev.*, vol. 32, pp. 97–100, 1928.

[59] S. A. Maas, *Noise in linear and nonlinear circuits*. Artech House, 2005.

[60] S. M. Sze and K. K. Ng, *Physics of semiconductor devices*. John Wiley and sons, 2007.

[61] R. Voss, "1/f (flicker) noise: a brief review," *Annu. Symp. Freq. Control*, vol. 33, pp. 40–46, 1979.

[62] B. Razavi, *Design of analog CMOS integrated circuits*. McGraw Hill, 2001.

[63] H. Osterberg, "An interferometer method of studying the vibrations of an oscillating quartz plate," *J. Opt. Soc. Am.*, vol. 22, pp. 19–34, Jan 1932.

[64] F. Ghebremichael and R. Knize, "Polymer relaxations determined by use of a temporally and thermally stable interferometer," *Opt. Lett.*, vol. 24, no. 21, pp. 1481 – 1483, 1999.

[65] K. Birch and M. Okaji, "Stable interferometer supporting system," *J. Phys. E: Sci. Instrum.*, vol. 19, no. 5, pp. 361 – 363, 1986.

[66] W. Lehmann, P. Gattinger, M. Keck, F. Kremer, P. Stein, T. Eckert, and H. Finkelmann, "Inverse electromechanical effect in mechanically oriented sc-elastomers examined by means of an ultra-stable michelson interferometer," *Ferroelectrics*, vol. 208, no. 209, pp. 373 – 383, 1998.

[67] R. Lange, P. Seitz, A. Biber, and R. Schwarte, "Time-of-flight range imaging with a custom solid state image sensor," *Laser Metrology and Inspection*, vol. 3823, no. 1, pp. 180–191, 1999.

[68] J. O. Stenflo and H. Povel, "Astronomical polarimeter with 2-d detector arrays," *Appl. Opt.*, vol. 24, pp. 3893–3898, Nov 1985.

[69] T. Spirig, P. Seitz, O. Vietze, and F. Heitger, "Lock-in ccd two-dimensional synchronous detection of light," *IEEE J. Quantum Electron.*, vol. 31, no. 9, pp. 1705 – 1708, 1995.

[70] P. Gulden, M. Vossiek, P. Heide, and R. Schwarte, "Novel opportunities for optical level gauging and 3d-imaging with the photoelectronic mixing device," *IEE Instr. Meas.*, vol. 51, no. 4, pp. 679–684, 2002.

[71] S. Ando and A. Kimachi, "Time-domain correlation image sensor: first cmos realization of demodulator pixels array," *Proc. IEEE CCD/AIS*, pp. 33 –36, 1999.

[72] S. Ando and A. Kimachi, "Correlation image sensor: two-dimensional matched detection of amplitude-modulated light," *IEEE Trans. Electron Devices*, vol. 50, no. 10, pp. 2059 – 2066, 2003.

[73] R. Schwarte, Z. Xu, H. G. Heinol, J. Olk, R. Klein, B. Buxbaum, H. Fischer, and J. Schulte, "New electro-optical mixing and correlating sensor: facilities and applications of the photonic mixer device (pmd)," *Proc. SPIE Int. Soc. Opt. Eng.*, vol. 3100, pp. 245 – 253, 1997.

[74] PMDtec, *PMD[vision] CamCube 3.0.* `http://www.pmdtec.com/products-services/pmdvisionr-cameras/pmdvisionr-camcube-30/`, 2012.

[75] D. Stoppa, N. Massari, L. Pancheri, M. Malfatti, M. Perenzoni, and L. Gonzo, "A range image sensor based on μm cmos imaging technology," *IEEE J. Solid-State Circuits*, vol. 46, no. 1, pp. 248–258, 2011.

[76] H. G. P. H. Benten, T. Ruotsalainen, A. J. Maekynen, T. E. Rahkonen, and H. K. Kopola, "Integrated synchronous receiver channel for optical instrumentation applications," *Sensors Sens. Syst. Sens. Data Process*, vol. 3100, no. 1, pp. 75–88, 1997.

[77] S. Bourquin, P. Seitz, and R. Salathe, "Two-dimensional smart detector array for interferometric applications," *Electron. Lett.*, vol. 37, no. 15, pp. 975 – 976, 2001.

[78] S. Bourquin, V. Monterosso, P. Seitz, and R. P. Salathé, "Video-rate optical low-coherence reflectometry based on a linear smart detector array," *Opt. Lett.*, vol. 25, pp. 102–104, Jan 2000.

[79] G. Lu, G. Guillaud, G. Sou, F. Devigny, M. Pitaval, and P. Morin, "Investigation of cmos bdj detector for fluorescence detection in microarray analysis," *Microtechnologies Med. Biol. 1st Annu. Int. Conf. 2000*, pp. 381–386, 2000.

[80] G. Lu, P. Pittet, G. Carrillo, and A. Mourabit, "On-chip synchronous detection for cmos photodetector," *Proc. IEEE Int. Conf. Electron. Circuits Syst.*, vol. 1, pp. 355 – 358, 2002.

[81] M. Pitter, J. Goh, M. Somekh, B. Hayes-Gill, M. Clark, and S. Morgan, "Phase-sensitive cmos photo-circuit array for modulated thermoreflectance measurements," *Electron. Lett*, vol. 39, no. 18, pp. 1339 – 1340, 2003.

[82] M. Pitter, R. Light, M. Somekh, M. Clark, and B. Hayes-Gill, "Dual-phase synchronous light detection with 64x64 cmos modulated light camera," *Electron. Lett*, vol. 40, no. 22, pp. 1404 – 1406, 2004.

[83] P. Dmochowski, B. Hayes-Gill, M. Clark, J. Crowe, M. Somekh, and S. Morgan, "Camera pixel for coherent detection of modulated light," *Electron. Lett.*, vol. 40, no. 22, pp. 1403 – 1404, 2004.

[84] P. Dmochowski, *CMOS Modulated Light Cameras*. PhD thesis, The University of Nottingham, 2006.

[85] N. A. Massie, R. D. Nelson, and S. Holly, "High-performance real-time heterodyne interferometry," *Appl. Opt.*, vol. 18, pp. 1797–1803, Jun 1979.

[86] G. E. Sommargren, "Optical heterodyne profilometry," *Appl. Opt.*, vol. 20, pp. 610–618, Feb 1981.

[87] N. A. Massie, "Real-time digital heterodyne interferometry: a system," *Appl. Opt.*, vol. 19, pp. 154–160, Jan 1980.

[88] M. Akiba, K. P. Chan, and N. Tanno, "Real-time, micrometer depth-resolved imaging by low-coherence reflectometry and a two-dimensional heterodyne detection technique," *Jpn. J. App. Phys.*, vol. 39, p. 1194, Nov. 2000.

[89] M. Akiba, K. P. Chan, and N. Tanno, "Full-field optical coherence tomography by two-dimensional heterodyne detection with a pair of ccd cameras," *Opt. Lett.*, vol. 28, pp. 816–818, May 2003.

[90] M. Pitter, C. See, and M. Somekh, "Full-field heterodyne interference microscope with spatially incoherent illumination," *Opt. Lett.*, vol. 29, pp. 1200–1202, JUN 1 2004.

[91] Y. U. Nam, M. S. Cheon, J. H. Ha, and Y. S. Hwang, "Improved common-path fast-scanning heterodyne interferometer system as potential dense-plasma diagnostics," *Rev. Sci. Instr.*, vol. 75, no. 10, pp. 3417–3419, 2004.

[92] S. Nakadate, "Shearing heterodyne interferometry using acoustooptic light modulators," *Appl. Opt.*, vol. 24, pp. 3079–3087, Sep 1985.

[93] S. Toyooka, T. Tanahashi, and M. Tominaga, "Simple heterodyne interferometry using a holographic common-path interferometer," *Appl. Opt.*, vol. 23, pp. 1460–1463, May 1984.

[94] M. J. Offside, M. G. Somekh, and C. W. See, "Common path scanning heterodyne optical profilometer for absolute phase measurement," *Appl. Phys. Lett.*, vol. 55, no. 20, pp. 2051–2053, 1989.

[95] C. Chou, J. chyang Shyu, Y. chuen Huang, and C. kee Yuan, "Common-path optical heterodyne profilometer: a configuration," *Appl. Opt.*, vol. 37, pp. 4137–4142, Jul 1998.

[96] M. V. Aguanno, F. Lakestani, M. J. Connelly, and M. P. Whelan, "Full-field heterodyne interferometry using a complementary metal-oxide semiconductor digital signal processor camera for high-resolution profilometry," *Opt. Eng.*, vol. 46, no. 9, pp. 095601–095601–5, 2007.

[97] Y. Park and K. Cho, "Heterodyne interferometer scheme using a double pass in an acousto-optic modulator," *Opt. Lett.*, vol. 36, no. 3, pp. 331 – 333, 2011.

[98] P. A. M. Dirac, *The Principles of Quantum Mechanics*. Oxford University Press, fourth edition ed., 1958.

[99] H. Paul, "Interference between independent photons," *Rev. Mod. Phys.*, vol. 58, pp. 209–231, Jan 1986.

[100] L. Basano and P. Ottonello, "Interference fringes from stabilized diode lasers," *Am. J. Phys*, vol. 68, no. 3, pp. 245–247, 2000.

[101] G. Magyar and L. Mandel, "Interference fringes produced by superposition of two independent maser light beams," *Nat. (London)*, vol. 198, no. 4877, pp. 255 – 256, 1963.

[102] F. Louradour, F. Reynaud, B. Colombeau, and C. Froehly, "Interference fringes between two separate lasers," *Am. J. Phys*, vol. 61, pp. 242–245, Mar 1993.

[103] T. Kawalec and D. Bartoszek-Bober, "Two-laser interference visible to the naked eye," *Eur. J. Phys.*, vol. 33, no. 1, pp. 85 – 90, 2012.

[104] C. Toumazou, F. J. Lidgey, and D. G. Haigh, *Analogue IC Design: The Current-Mode Approach*. 1993.

[105] B. Gilbert, "A new wide-band amplifier technique," *J. Solid State Circuits*, vol. 3, pp. 353 – 365, 1968.

[106] P. W. Milonni and J. H. Eberly, *Laser Physics (2nd Edition)*. Wiley, 2010.

[107] JDSU, *Uniphase 1100 series HeNe lasers*. `http://www.jdsu.com/en-us/Lasers/Products/A-Z-Product-List/Pages/laser-head-helium-neon-1100-series.aspx`, 2013.

[108] S. Goldwasser, *Laser Repair FAQs*. `http://www.repairfaq.org/`, 2011.

[109] S. Hooker and C. Webb, *Laser Physics*. Oxford master series in atomic, optical, and laser physics, 2010.

[110] C. L. Tang and H. Statz, "Nonlinear effects in the resonant absorption of several oscillating fields by a gas," *Phys. Rev.*, vol. 128, pp. 1013–1021, Nov 1962.

[111] H. Niewenhuijzen, "On the doppler frequency shift of light using rotating mirrors," *Bull. Astron. Inst. Neth.*, vol. 20, p. 2431, Jan 1969.

[112] R. N. Shagam and J. C. Wyant, "Optical frequency shifter for heterodyne interferometers using multiple rotating polarization retarders," *Appl. Opt.*, vol. 17, pp. 3034–3035, Oct 1978.

[113] H. Lck, J. Degallaix, H. Grote, M. Hewitson, S. Hild, B. Willke, and K. Danzmann, "Opto-mechanical frequency shifting of scattered light," *J. Opt. A: Pure Appl. Opt.*, vol. 10, no. 8, p. 085004, 2008.

[114] S. G. Johnson and J. D. Joannopoulos, "Designing synthetic optical media: photonic crystals," *Acta Mater.*, vol. 51, pp. 5823–5835, Nov. 2003.

[115] L. E. Drain and B. C. Moss, "The frequency shifting of laser light by electro-optic techniques," *Opt. Quantum Electron.*, vol. 4, pp. 429–439, 1972.

[116] D. Johnson, J. Hogan, S.-W. Chiow, and M. Kasevich, "Broadband optical serrodyne frequency shifting," *Opt. Lett.*, vol. 35, no. 5, pp. 745 – 747, 2010.

[117] B. Ware and W. Flygare, "Light scattering in mixtures of bsa, bsa dimers, and fibrinogen under the influence of electric fields," *J. Colloid Interface Sci.*, vol. 39, no. 3, pp. 670 – 675, 1972.

[118] C. V. Raman and N. S. N. Nath, "The diffraction of light by high frequency sound waves," *Proc. Indian Academy of Science*, vol. 2, pp. 406–412, 1935.

[119] W. H. Bragg and W. L. Bragg, "The reflection of x-rays by crystals," *Proc. R.l Soc. Lond. A*, vol. 88, no. 605, pp. 428–438, 1913.

[120] Gouch and Housego, *Gouch and Housego 40MHz AOFS datasheet (I-FS040)*. `http://www.goochandhousego.com/sites/default/files/documents/I-FS040-2S2E-3-0L3%20data%20sheet.pdf`, 2012.

[121] Gouch and Housego, *List of available Gouch and Housego AOFS*. http://www.goochandhousego.com/products/acousto-optics/frequency-shifters, 2012.

[122] A. Korpel, "Acousto-optics; a review of fundamentals," *Proceedings of the IEEE*, vol. 69, no. 1, pp. 48–53, 1981.

[123] NI, *NI PCI-6251 multi-channel DAQ board*. http://sine.ni.com/nips/cds/view/p/lang/en/nid/14124, 2013.

[124] D. Schleef, F. M. Hess, and I. Abbott, *Comedi - Control and Measurement Interface*. http://www.comedi.org, 2012.

[125] F. Gray, *US Patent No. 2632058 A - Pulse code communication*. 1953.

[126] D. Joseph and S. Collins, "Modeling, calibration, and correction of nonlinear illumination-dependent fixed pattern noise in logarithmic cmos image sensors," *IEEE Trans. Instrum. Meas.*, vol. 51, no. 5, pp. 996–1001, 2002.

[127] E. L. Ruden, J. F. Camacho, and A. G. Lynn, "Visibility oscillation in a multimode laser interferometer signal and its use in optimizing path lengths," *Rev. Sci. Instr.*, vol. 84, no. 10, pp. –, 2013.

[128] R. M. Goldstein, H. A. Zebken, and C. L. Werner, "Satellite radar interferometry: Two-dimensional phase unwrapping," *Radio Sci.*, vol. 23, pp. 713–720, 1988.

[129] PMDtec, *pmd PhotonICs 19k-S3*. http://www.pmdtec.com/html/pdf/pmdPhotonICs_19k_S3.pdf, 2013.

[130] M. J. Griffin, *Handbook of Human Vibration*. 988 p, Academic Press, 1996.

[131] A. Ismail, M. Nuawi, N. Kamaruddin, and R. Bakar, "Comparative assessment of the whole-body vibration exposure under different car speed based on malaysian road profile," *J. Appl. Sci.*, vol. 10 (14), pp. 1428–1434, 2010.

[132] A. Ismail, M. Nuawi, C. How, N. Kamaruddin, M. Nor, and N. Makhtar, "Whole body vibration exposure to train passenger," *Am. J. Appl. Sci.*, vol. Volume 7, Issue 3, pp. 352–359, 2010.

[133] C. G. Gordon, "Generic criteria for vibration-sensitive equipment," *Proc. SPIE Int. Soc. Opt. Eng.*, vol. 1619, pp. 71 – 85, 1992.

[134] W. Hays and G. S. (U.S.), *Facing geologic and hydrologic hazards: earth-science considerations*. No. v. 1240 in Earth-science special reports, U.S. Dept. of the Interior, Geological Survey, 1981.

[135] P. J. Stafford, F. O. Strasser, and J. J. Bommer, "An evaluation of the applicability of the nga models to ground-motion prediction in the euro-mediterranean region," *Bull. Earthquake Eng.*, vol. 6, no. 2, pp. 149 – 177, 2008.

[136] S. Rajasekaran, *Structural dynamics of earthquake engineering: theory and application using MATHEMATICA and MATLAB*. Woodhead Publishing, 2009.

[137] F. G. Cervantes, G. Heinzel, A. F. G. Marin, V. Wand, F. Steier, O. Jennrich, and K. Danzmann, "Real-time phase-front detector for heterodyne interferometers," *Appl. Opt.*, vol. 46, no. 21, pp. 4541 – 4548, 2007.

[138] J. M. Chartier, J. Labot, G. Sasagawa, T. M. Niebauer, and W. Hollander, "A portable iodine stabilized he-ne-laser and its use in an absolute gravimeter," *IEEE Trans. Instrum. Meas.*, vol. 42, pp. 420–422, April 1993.

[139] R. Balhorn, H. Kunzmann, and F. Lebowsky, "Frequency stabilization of internal-mirror helium-neonlasers," *Appl. Opt.*, vol. 11, pp. 742–744, Apr 1972.

[140] S. J. Bennett, R. E. Ward, and D. C. Wilson, "Comments on: frequency stabilization of internal mirror he-ne lasers," *Appl. Opt.*, vol. 12, pp. 1406–1406, Jul 1973.

[141] S. K. Gordon and S. F. Jacobs, "Modification of inexpensive multimode lasers to produce a stabilized single frequency beam," *Appl. Opt.*, vol. 13, pp. 231–231, Feb 1974.